AD_____

Grant Number DAMD17-94-J-4384

TITLE: New Methods for Quantitative, High-Resolution Ultrasonic
Imaging of the Breast

PRINCIPAL INVESTIGATOR: Robert C. Waag, Ph.D.

CONTRACTING ORGANIZATION: University of Rochester
                           Rochester, New York 14627

REPORT DATE: January 1998

TYPE OF REPORT: Final

PREPARED FOR: U.S. Army Medical Research and Materiel Command
               Fort Detrick, Maryland 21702-5012

DISTRIBUTION STATEMENT: Approved for public release;
                         distribution unlimited

The views, opinions and/or findings contained in this report are
those of the author(s) and should not be construed as an official
Department of the Army position, policy or decision unless so
designated by other documentation.

19980617 094

1

REPORT DOCUMENTATION PAGE

Public reporting burden for this collection of information is estimated to average 1 hour per response, including the time for reviewing instructions, searching existing data sources, gathering and maintaining the data needed, and completing and reviewing the collection of information. Send comments regarding this burden estimate or any other aspect of this collection of information, including suggestions for reducing this burden, to Washington Headquarters Services, Directorate for Information Operations and Reports, 1215 Jefferson Davis Highway, Suite 1204, Arlington, VA 22202-4302, and to the Office of Management and Budget, Paperwork Reduction Project (0704-0188), Washington, DC 20503.

1. AGENCY USE ONLY (Leave blank)	2. REPORT DATE January 1998	3. REPORT TYPE AND DATES COVERED Final (30 Sep 94 – 31 Dec 97)

4. TITLE AND SUBTITLE
New Methods for Quantitative, High-Resolution Ultrasonic Imaging of the Breast

5. FUNDING NUMBERS
DAMD17-94-J-4384

6. AUTHOR(S)
Robert C. Waag, Ph.D.

7. PERFORMING ORGANIZATION NAME(S) AND ADDRESS(ES)
University of Rochester
Rochester, New York 14627

8. PERFORMING ORGANIZATION REPORT NUMBER

9. SPONSORING/MONITORING AGENCY NAME(S) AND ADDRESS(ES)
U.S. Army Medical Research and Materiel Command
Fort Detrick, Maryland 21702-5012

10. SPONSORING/MONITORING AGENCY REPORT NUMBER

11. SUPPLEMENTARY NOTES

12a. DISTRIBUTION / AVAILABILITY STATEMENT
Approved for public release; distribution unlimited

12b. DISTRIBUTION CODE

13. ABSTRACT (Maximum 200

The objective of this research is to form quantitative, high-resolution ultrasonic images of the breast using advances in adaptive focussing, a breakthrough in inverse scattering, and unique experimental apparatus. Two new imaging methods were implemented and test images were formed to demonstrate the potential of the methods to improve resolution for better diagnosis of breast cancer. One method employs adaptive focussing to compensate for aberration in pulse-echo imaging. In this new technique, transmit signals are synthesized from scattered signals by using backpropagation followed by time-shift estimation and compensation. The other method uses eigenfunctions and eigenvalues of an operator associated with scattering measurements to focus adaptively on distributed scattering objects and to form quantitative images efficiently. Image evaluation employed comparison with observed morphology of scattering objects as well as with conventional b-scan images and reconstructed x-ray images.

14. SUBJECT TERMS
Breast Cancer
Ultrasound, imaging, diagnosis, quantitative, high-resolution.

15. NUMBER OF PAGES
97

16. PRICE CODE

17. SECURITY CLASSIFICATION OF REPORT	18. SECURITY CLASSIFICATION OF THIS PAGE	19. SECURITY CLASSIFICATION OF ABSTRACT	20. LIMITATION OF ABSTRACT
Unclassified	Unclassified	Unclassified	Unlimited

NSN 7540-01-280-5500

Standard Form 298 (Rev. 2-89)
Prescribed by ANSI Std. Z39-18
298-102

FOREWORD

Opinions, interpretations, conclusions and recommendations are those of the author and are not necessarily endorsed by the U.S. Army.

_____ Where copyrighted material is quoted, permission has been obtained to use such material.

_____ Where material from documents designated for limited distribution is quoted, permission has been obtained to use the material.

_____ Citations of commercial organizations and trade names in this report do not constitute an official Department of Army endorsement or approval of the products or services of these organizations.

_____ In conducting research using animals, the investigator(s) adhered to the "Guide for the Care and Use of Laboratory Animals," prepared by the Committee on Care and Use of Laboratory Animals of the Institute of Laboratory Resources, National Research Council (NIH Publication No. 86-23, Revised 1985).

_√_ For the protection of human subjects, the investigator(s) adhered to policies of applicable Federal Law 45 CFR 46.

_____ In conducting research utilizing recombinant DNA technology, the investigator(s) adhered to current guidelines promulgated by the National Institutes of Health.

_____ In the conduct of research utilizing recombinant DNA, the investigator(s) adhered to the NIH Guidelines for Research Involving Recombinant DNA Molecules.

_____ In the conduct of research involving hazardous organisms, the investigator(s) adhered to the CDC-NIH Guide for Biosafety in Microbiological and Biomedical Laboratories.

Robert C. Waag   28 Jan 98
‾‾‾‾‾‾‾‾‾‾‾‾‾‾‾‾‾‾‾‾‾‾‾‾‾‾‾‾‾‾‾‾‾‾
PI - Signature   Date

3

4. Table of Contents

5. Introduction

Widely recognized strengths of ultrasonic imaging techniques for diagnosis and monitoring for recurrence of breast cancer are the nonionizing nature of acoustic waves, the ability to provide good contrast between fluid and parenchymal tissue, portability, and good patient tolerance. Ultrasonic imaging is inexpensive compared to magnetic resonance imaging and is competitive in cost with x-ray mammography. However, these strengths are presently offset by significant weaknesses that include low resolution, inability to distinguish between solid masses, and the lack of quantitative information about breast tissue characteristics.

For some years, recognition has existed that high-resolution and quantitative ultrasonic imaging has the potential to provide diagnostic information not available through conventional ultrasonic techniques such as b-scanning. Aberration correction promises to increase significantly the resolution of ultrasonic mammography so that small lesions, tumors, and microcalcifications can be clearly imaged even through fatty or dense breast tissue. Quantitative, high-resolution ultrasonic imaging is particularly desirable for the diagnosis of breast disease since the approach has the potential to differentiate between types of cancerous tissue, to detect and characterize microcalcifications, to detect small tumors even in dense breast tissue, and to yield diagnostically useful images without operator-dependent adjustments of parameters.

The purpose of this research is to develop new ultrasonic imaging concepts based on significant advances in adaptive focusing and breakthroughs in inverse scattering as well as on newly available novel experimental apparatus. To focus adaptively, transmit signals are synthesized from scattered signals by using backpropagation followed by time-shift estimation and compensation. To reconstruct quantitatively, eigenfunctions and eigenvalues of an operator associated with scattering measurements are used to obtain efficiently images of distributed scattering objects.

6. Body

a. Method

The method employed to achieve the goal of quantitative and high-resolution ultrasonic imaging employs a combination of hardware innovations, careful measurements of ultrasonic aberrations and scattering, and implementation of new ideas for aberration correction as well as for image reconstruction via inverse scattering. The novel hardware consists of two different systems. One is a custom made pulse-echo apparatus in which the size of the transmit aperture can easily be altered and in which scattering objects can be easily changed without disturbing the aberrator. The other apparatus consists of a ring transducer array with 2048 elements and associated circuitry for multiplexing and signal control. Measurements performed with this ring produce experimental data from which the degrading effects of wavefront distortion imaging were studied. Measurements also provided experimental data from phantoms with known acoustic parameters for image reconstruction. Receive beamforming used backpropagation and other methods of space-time processing. Measured scattering data with three hundred and sixty degrees of spatial coverage was used for the reconstruction of quantitative ultrasonic images through the use of newly developed inverse scattering methods.

b. Results

Ultrasonic wavefront distortion produced by transmission through breast tissue specimens was measured in a two-dimensional aperture. Differences in arrival time and energy level between the measured waveforms and references that account for geometric delay and spreading were calculated as was the waveform similarity factor. Details of this investigation were reported in the Journal of the Acoustical Society of America. A copy of this paper is included as Appendix A. In this paper, maps of distortion are shown in Figure 2 focussing results are shown in Figure 3 and comparisons with corresponding abdominal wall data are given in Figures 7 and 8.

A new method of waveform design was developed and implemented to produce a spatially limited plane wave for illumination of the scattering object to be imaged. The method employed backpropagation of the desired spatially limited plane wavefront to obtain excitation signals for the ring transducer elements. A paper describing the methods in detail was published in the *IEEE Transactions on Ultrasonics, Ferroelectrics, and Frequency Control*. A copy of this paper is included as Appendix B. Figure 6 in this paper shows illustrative results.

Estimation and correction of ultrasonic wavefront distortion using pulse-echo data has also been implemented in an experimental setting. The processing used random scattering measured in a specially designed pulse-echo configuration in which the transmit beam is unperturbed by the aberrating medium. Major results in are:

1) A tightly focussed transmit beam, such as that achieved with f/1.5, is needed to produce a sufficiently coherent scattered wavefront so that time delay can be accurately estimated.

2) Accommodation of waveform shape distortion in time-delay estimation, such as in the modified least-mean-square-error method that incorporates a global smoothness requirement, is necessary for estimation of the time-delay surface of a wavefront that has propagated through distributed inhomogeneities.

3) The isoplanatic path size usually decreases with increasing severity of distortion and is influenced by compensation technique.

4) Incorporation of waveform shape compensation, such as by using backpropagation prior to time-shift compensation, improves the contrast ratio over that obtained by time-shift compensation alone.

A paper that details this work has been accepted for publication in the *IEEE Transactions on Ultrasonics, Ferroelectrics, and Frequency Control* and a preprint of this paper is included as Appendix C. Figures 9-14 of the preprint show results that are representative.

A novel inverse scattering method that uses eigenfunctions of the scattering operator was examined theoretically and using computations. A unified framework that encompasses eigenfunction methods of focussing and image reconstruction in arbitrary media was developed. A paper detailing this work has been published in the *Journal of the Acoustical Society of America* and is included as Appendix D to provide more detail. Figures 2 through 8 in this paper show representative images.

Representative high-resolution b-scan images produced by our ring transducer system are presented in Figure 1 along with a corresponding b-scan image produced by a conventional ultrasonic scanner and a corresponding x-ray image produced by computed tomography. The results show that our ring transducer system is capable of producing images that are superior to those of commercial b-scan ultrasonic imagers and comparable to those obtained from computed x-ray tomography.
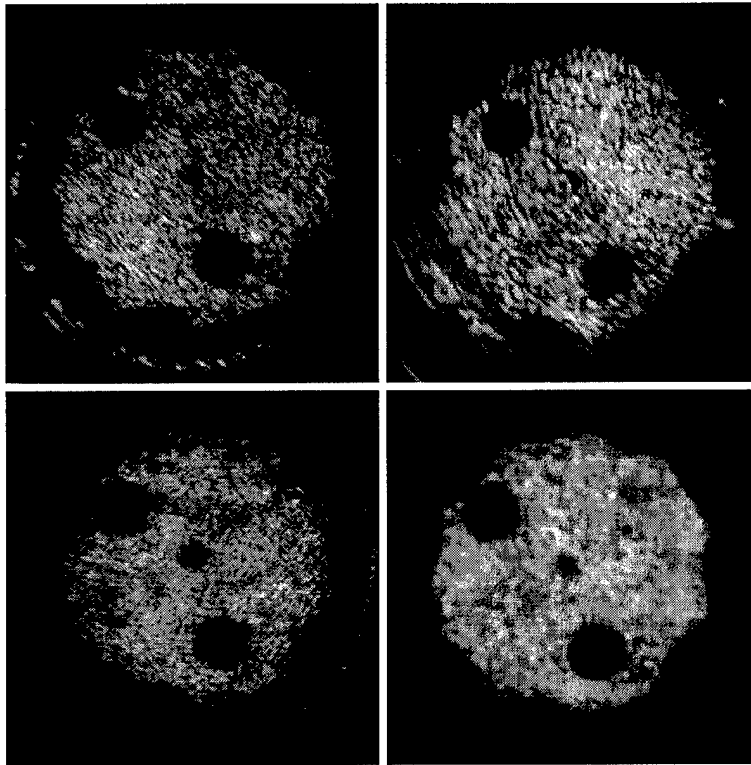
Fig. 1. Images of an Anthropomorphic Breast Phantom, The phantom was imaged in a plane containing two 9 mm diameter cysts on the periphery of the phantom and one 4 mm diameter cyst near the center. Top Left: single b-scan image obtained with the ring transducer system using f/1.0 aperture and scan plane diameter of 80 mm. Top right: b-scan image produced by a state-of-the-art clinical b-scanner operating at the same center frequency as the ring transducer system. Bottom Left: compounded b-scan image from six geometrically corrected views with the ring transducer system. Bottom Right: X-ray computed tomograph obtained with a state-of-the-art scanner using a 1 mm slice thickness. These images show that ring transducer b-scan resolution is superior to current clinical scanners at the same frequency and is comparable with x-ray computed tomography.

c. Discussion

The studies summarized above and detailed in appendices show that all of the tasks in the statement of work have been largely accomplished although studies employing breast tissue and comparative evaluations of imaging modalities were more limited than originally planned. These limitations resulted from lost time caused by unforeseen equipment failures and the need for more software development than made possible by the budget. Nevertheless, the results demonstrate the new ultrasonic imaging methods developed in this project have potential.

7. Conclusions

The forgoing results and discussion show that the research generally progressed along the lines described in the original proposal. Unanticipated problems limited the depth of some studies and the extent of progress but important theoretical, experimental, and computational results have been obtained. Additional studies that involve more use of tissue and further comparative evaluation of imaging modalities are needed to determine the ultimate capability of the imaging techniques investigated in this project to improve detection, diagnosis, and treatment monitoring of breast cancer.

8. References

The following publications provide additional background and further detail related to this research.

Breast Cancer: A Practical Guide to Diagnosis, Logan-Young, W. and Hoffman, N.Y., Vol 1 - Procedures, Mt. Hope Publishing Co., Rochester, NY (1994).

Critical Pathways in Using Breast US, Mendelson, E.B. and Tobin, C.E.,Radiographics 15:935-945 (1995).

Amplitude Characteristics of Ultrasound Waveform Distortion Produced by Abdominal Wall and Breast, Liu, D.-L., and Waag, R. C., J. Acoust. Soc. Am. 101(2):1172-1183 (1997).

Simulation of Ultrasonic Propagation Through Abdominal Wall, Mast, T.D., Hinkelman, L.M. and Waag, R.C., J. Acoust. Soc. Am. 102(2):1177-1191 (1997).

A Comparison of Wavefront Distortion in One-Dimensional and Two-Dimensional Apertures, Liu, D.-L. and Waag, R.C. IEEE Trans. UFFC 42(4):726-733 (1995).

Measurements of Ultrasonic Pulse Distortion Produced by the Chest Wall, Hinkelman, L.M., Waag, R.C., Szabo, T.L., 40th Annual Convention of the American Institute of Ultrasound in Medicine, 17-20 March 1996, New York, New York. Submitted.

Measurements of Ultrasonic Pulse Distortion Produced by the Chest Wall, Hinkelman, L.M., Waag, R.C., Szabo, T.L., J. Acoust. Soc. Am. 101(4):2365-2373 (1997).

9. Final Report Information

a. Bibliography of Publications and Meeting Abstracts

Publications in Journals

1. Measurements of ultrasonic pulse arrival time and energy level variations produced by propagation through abdominal wall: Hinkelman, L. M., Liu, D.-L., Metlay, L. A., and Waag, R. C. J. Acoust. Soc. Am. 95(1):530-541 (1994).

2. Time-shift compensation of ultrasonic pulse focus degradation using least mean square error estimates of time delay: Liu, D.-L. and Waag, R. C. J. Acoust. Soc. Am. 95(1):542-555 (1994).

3. Correction of ultrasonic wavefront distortion using backpropagation and a reference waveform method for time-shift compensation: Liu, D.-L. and Waag, R. C. J. Acoust. Soc. Am. 96(2):649-660 (1994).

4. Measurement and correction of ultrasonic pulse distortion produced by the human breast: Hinkelman, L. M., Liu, D.-L., Waag, R. C., Zhu, Q., and Steinberg, B. D., J. Acoust. Soc. Am. 97(3):1958-69 (1995).

5. A comparison of wavefront distortion in one-dimensional and two-dimensional apertures: Liu, D.-L. and Waag, R. C. IEEE Trans. on Ultras. Ferro. and Freq. Contr. 42(4):726-733 (1995).

6. Modified Gomori's trichrome stain for macroscopic tissue slices: Hinkelman, L. M., Metlay, L. A., Churukian, C. J., and Waag, R. C., J. Histotechnology 19(4):321-323 (1996).

7. Propagation and backpropagation for ultrasonic wavefront design: Liu, D.-L., and Waag, R. C. IEEE Trans. on Ultras. Ferro. and Freq. Contr. 44(1):1-13 (1997).

8. Harmonic amplitude distribution in a wideband ultrasonic wavefront after propagation through human abdominal wall and breast specimens: Liu, D.-L., and Waag, R. C. J. Acoust. Soc. Am. 101(2):1172-1183 (1997).

9. Measurements of ultrasonic pulse distortion produced by the human chest wall: Hinkelman, L. M., Szabo, T. L., and Waag, R. C. J. Acoust. Soc. Am. 101(4):2365-2373 (1997).

10. Simulation of ultrasonic pulse propagation through abdominal wall: Mast, T. D., Hinkelman, L. M., Sparrow, V. W., Orr, M. J., and Waag, R. C. J. Acoust. Soc. Am. 102(2):1177-1191 (1997).

11. Focussing and imaging using eigenfunctions of the scattering operator: Mast, T. D., Nachman, A. I., and Waag, R. C. J. Acoust. Soc. Am. 102(2):715-726 (1997).

12. Estimation and correction of ultrasonic wavefront distortion using pulse-echo data received in a two-dimensional aperture: Liu, D.-L., and Waag, R. C. IEEE Trans. on Ultras. Ferro. and Freq. Contr. In press.

Symposium/Conference Papers

1. Wavefront backpropagation and focus correction: Waag, R. C. and Liu, D.-L. 1993 Ultrasonics Symposium Proc., 31 Oct - 3 Nov '93, Baltimore, Maryland, IEEE cat. no. 93CH3301-9, pp 1127-1130.

2. Estimation and correction of ultrasonic wavefront distortion using pulse-echo data: Waag, R. C. and Liu, D.-L. 1996 Ultrasonics Symposium Proc., 3-6 November '96, San Antonio, Texas. IEEE cat. no. 96CH35993-2, pp1391-1394.

Abstracts/Summaries

1. Resolution obtained from one-dimensional and two-dimensional time-shift compensation using measurements of pulses transmitted through tissue: Liu, D.-L. and Waag, R. C. 38th Annual Meeting, American Institute of Ultrasound in Medicine, 20-23 March 1994, Baltimore, Maryland (J. Ultras. Med., v 13, no. 3, Supp., Mar '94 p S40).

2. Measurement, evaluation, and correction of ultrasonic wavefront distortion produced by breast specimens: Hinkelman, L. M., Liu, D.-L., Waag, R. C., Zhu, Q., and Steinberg, B. D. 21st International Symposium on Acoustical Imaging, 28-30 Mar 1994, Laguna Beach, California (Conference Record, p 3).

3. Visualizations for studies of ultrasonic scattering and propagation in medical applications (invited): Waag, R. C. 126th Meeting, Acoustical Society of America, 5-7 Jun 1994, Cambridge, Massachusetts (J. Acoust. Soc. Am., v 95, no. 5, Part 2, Jun '94, p 2902).

4. Preliminary 2-D measurements of coherent and incoherent scattering in the female breast as a function of propagation distance: Zhu, Q., Steinberg, B. D., Hinkelman, L. M. and Waag, R. C. Symposium on Ultrasonic Imaging and Tissue Characterization, 6-8 Jun 94, Arlington, Virginia (Acoustic Imaging, v 16, no. 1, p 31).

5. Measurement and correction of ultrasonic wavefront distortion produced by breast specimens: Hinkelman, L. M., Liu, D.-L., Waag, R. C. , Zhu, Q. and Steinberg, B. D. World Federation for Ultrasound Med. Biol. Seventh Congress, 17-22 Jul 1994, Sapporo, Hokkaido, Japan (J. Ultrasound Med. Biol., v 20, Supp. 1, p S77).

6. Experimental Study of Time-Shift Estimation for Compensation of Wavefront Distortion Using Scattered Signals: Kanda, R., Liu, D.-L., and Waag, R. C. World Federation for Ultrasound Med. Biol. Seventh Congress, 17-22 Jul 1994, Sapporo, Hokkaido, Japan (J. Ultrasound Med. Biol., v 20, Supp. 1, p S85).

7. Measurements of wavefront distortion and compensation of focus degradation (invited): Waag, R. C., Liu, D.-L, and Hinkelman, L. M. World Federation for Ultrasound Med. Biol. Seventh Congress, 17-22 Jul 1994, Sapporo, Hokkaido, Japan (J. Ultrasound Med. Biol., v 20, Supp. 1, p S25).

8. Eigenfuction and eigenvalue analysis of scattering operators: Mast, T. D. and Waag, R. C. 128th Meeting, Acoustical Society of America, 28 Nov - 2 Dec 1994, Austin, Texas (J. Acoust. Soc. Am., v 96, no. 5, Part 2, Nov '94, p 3336).

9. Amplitude characteristics of ultrasound waveform distortion produced by abdominal wall and breast: Liu, D.-L. and Waag, R. C. 39th Annual Convention, American Institute of Ultrasound in Medicine, 26-29 March 1995, San Francisco, California (J. Ultrasound Med., v 14, no 3, Supp., Mar '95, p S46).

10. Simulation of ultrasonic propagation through abdominal wall: Mast, T. D., Hinkelman, L. M., Waag, R. C., and Sparrow, V. W. 129th Meeting, Acoustical Society of America, 30 May-3 June 1995, Washington, D.C. (J. Acoust. Soc. Am., v 97, no. 5, Part 2, May '95, p 3325).

11. Measurements of ultrasonic pulse distortion produced by the chest wall: Hinkelman, L. M. Waag, R. C. and Szabo, T. L. 130th Meeting, Acoustical Society of America, 27 Nov-1 Dec 1995, St. Louis, Missouri (J. Acoust. Soc. Am., v 98, no. 5, Part 2, Nov '95, p 2922).

12. Measurement and correction of ultrasonic wavefront distortion (invited): Waag, R. C., Liu, D.-L., Hinkelman, L. M., and Mast, T. D. Third Joint Meeting Acoustical Society of America and Acoustical Society of Japan, 2-6 December 1996, Honolulu, Hawaii (J. Acoust. Soc. Am., v 100, no. 4, Pt 2, p 2646, Oct '96).

13. An ultrasonic ring transducer system for studies of scattering and imaging (invited): Waag, R. C., Liu, D.-L., Mast, T .D., Nachman, A. I., Jaeger, P., and Kojima, T. Third Joint Meeting Acoustical Society of America and Acoustical Society of Japan, 2-6 December 1996, Honolulu, Hawaii (J. Acoust. Soc. Am., v 100, no. 4, Pt 2, p 2795, Oct '96).

14. An ultrasonic ring transducer system for studies of scattering and imaging (invited): Waag, R. C., Liu, D.-L., Mast, T .D., Nachman, A. I., Jaeger, P., and Kojima, T. International Conference on Imaging and Image Processing Technology, 9-11 December 1996, Santa Barbara, California (Book of Abstracts. p 6).

15. Propagation and backpropagation for ultrasonic wavefront design: Liu, D.-L. and Waag, R. C. 41st Annual Convention, American Institute of Ultrasound in Medicine, 23-26 March 1997, San Diego, California (J. Ultrasound Med., v 16, no 3, Supp., Mar '97, p S12).

16. An ultrasonic ring transducer system for studies of scattering and imaging: Waag, R. C., Liu, D.-L., Mast, T. D., Nachman, A. I., Jaeger, P., and Kojima, T. 41st Annual Convention, American Institute of Ultrasound in Medicine, 23-26 March 1997, San Diego, California (J. Ultrasound Med., v 16, no 3, Supp., Mar '97, p S61).

17. Compensation for array nonidealities by electronic: Liu, D.-L., Waag, R. C., and Oakley, C. 133rd Meeting of the Acoustical Society of America, 15-20 June 1997, State College, Pennsylvania (J. Acoust. Soc. Am., v 101, no 5, pt 2, May '97, p 3115).

18. Ultrasonic wavefront distortion caused by human abdominal wall layers: Hinkelman, L. M., Mast, T. D., Orr, M. J., and Waag, R. C. 133rd Meeting of the Acoustical Society of America, 15-20 June 1997, State College, Pennsylvania (J. Acoust. Soc. Am., v 101, no 5, pt 2, May '97, p 3140).

b. List of Personnel (alphabetical)

1. Laura M. Hinkelman

2. Erling J. Hoie

3. Tomas T. Jansson

4. Dong-Lai Lin

5. Feng Lin

6. T. Douglas Mast

7. Adrian I. Nachman

8. Laurent P. Souriau

9. Robert C. Waag

10. List of Appendices

Appendix A. Measurement and Correction of Ultrasonic Pulse Distortion Produced by the Human Breast

Appendix B. Propagation and Backpropagation for Ultrasonic Wavefront Design

Appendix C. Estimation and Correction of Ultrasonic Wavefront Distortion Using Pulse-Echo Data.

Appendix D. Focussing and Imaging Using Eigenfunctions of the Scattering Operator

Measurement and correction of ultrasonic pulse distortion produced by the human breast

Laura M. Hinkelman and Dong-Lai Liu
Department of Electrical Engineering, University of Rochester, Rochester, New York 14627

Robert C. Waag
Departments of Electrical Engineering and Radiology, University of Rochester, Rochester, New York 14627

Qing Zhu and Bernard D. Steinberg
Valley Forge Research Center, The Moore School of Electrical Engineering, University of Pennsylvania, Philadelphia, Pennsylvania 19104

Ultrasonic wavefront distortion produced by transmission through breast tissue specimens was measured in a two-dimensional aperture. Differences in arrival time and energy level between the measured waveforms and references that account for geometric delay and spreading were calculated. Also calculated was a waveform similarity factor that is decreased from 1.0 by changes in waveform shape. For nine different breast specimens, the arrival time fluctuations had an average (±s.d.) rms value of 66.8 (±12.6) ns and an associated correlation length of 4.3 (±1.1) mm, while the energy level fluctuations had an average rms value of 5.0 (±0.5) dB and a correlation length of 3.4 (±0.8) mm. The corresponding waveform similarity factor was 0.910 (±0.023). The effect of the wavefront distortion on focusing and the ability of time-shift compensation to remove the distortion were evaluated by comparing parameters such as the −30-dB effective radius, the −10-dB peripheral energy ratio, and the level at which the effective radius departs from an ideal by 10% for the focus obtained without compensation, with time-shift estimation and compensation in the aperture, and with time-shift estimation and compensation performed after backpropagation. For the nine specimens, the average −10-dB peripheral energy ratio of the focused beams fell from 3.82 (±1.83) for the uncompensated data to 0.96 (±0.18) with time-shift compensation in the aperture and to 0.63 (±0.07) with time-shift compensation after backpropagation. The average −30-dB effective radius and average 10% deviation level were 4.5 (±0.8) mm and −19.2 (±3.5) dB, respectively, for compensation in the aperture and 3.2 (±0.7) mm and −22.8 (±2.8) dB, respectively, for compensation after backpropagation. The corresponding radius for the uncompensated data was not meaningful because the dynamic range of the focus was generally less than 30 dB in the elevation direction, while the average 10% deviation level for the uncompensated data was −4.9 (±4.1) dB. The results indicate that wavefront distortion produced by breast significantly degrades ultrasonic focus in the low MHz frequency range and that much of this degradation can be eliminated using wavefront backpropagation and time-shift compensation.

PACS numbers: 43.80.Cs, 43.80.Ev, 43.80.Vj

INTRODUCTION

Widely recognized strengths of ultrasonic imaging techniques for diagnosis and monitoring of breast disease are the nonionizing nature of acoustic waves and the ability to provide good contrast between fluids and parenchymal tissues. However, despite advances in transducer technology, breast ultrasonography has thus far been relegated to ancillary use, largely because resolution is inadequate.[1,2] This has led to consideration of the limitations imposed on ultrasonic imaging of the breast by wavefront distortion that arises from propagation through breast tissue.

Several researchers have studied ultrasonic distortion produced by the breast and considered how this distortion may be compensated. An early *in vivo* pulse-echo study by Moshfeghi and Waag[3] showed that increasing the aperture to *f*/1.0 from *f*/2.6 for breast produced only about $\frac{2}{3}$ the resolution improvement predicted in a homogeneous medium. Trahey *et al.*[4] made one-dimensional transmission measure- ments of ultrasonic phase distortion caused *in vivo* by propagation through breast and found an average rms arrival time aberration of 36.1 ns for 22 subjects. The same group later extended their transmission measurements to two dimensions and obtained an rms value of 55.3 ns for seven volunteers.[5] They concluded that phase distortion should be measured and corrected in two dimensions but did not mention amplitude distortion. In other *in vivo* one-dimensional transmission measurements, Zhu and Steinberg observed severe amplitude distortion, which they attributed to refraction in addition to scattering,[6,7] and obtained a relation between the average sidelobe floor and the normalized variance of the amplitude distortion produced by the breast.[8,9] They concluded that large two-dimensional arrays and new algorithms that correct both phase and amplitude distortion in two dimensions may be needed to reduce the effects of distortion produced by the breast.

Two basic algorithms for correction of ultrasonic distor-

tion have been investigated for general imaging applications. The first relies on cross correlation of signals in the aperture for estimation of pulse arrival time,[10,11] while the other adjusts beamformer delays to maximize signal brightness.[12,13] However, neither of these methods addresses the problems of amplitude and waveform distortion, since both use only time-shift compensation in the aperture. Another technique has been investigated for the removal of amplitude and waveform distortion as well as time-shift distortion in specialized applications when a point source is present as may be the case in lithotripsy. This technique employs time-reversed signals but is limited because a suitable point source is not generally available in every isoplanatic patch to be imaged.[14,15] A more recent method developed by Liu and Waag[16] can be used to remove time-shift, amplitude, and waveform distortion in general imaging applications. Their approach models the distorting medium as a phase screen placed some distance from the receiving aperture and removes amplitude and waveform distortion by backpropagation of the wavefront before applying time-shift compensation.

This paper reports a study of ultrasonic wavefront distortion produced by breast and the effectiveness of the backpropagation method in removing the distortion. In the study, wavefronts perturbed by transmission through breast tissue were measured in a two-dimensional aperture. Statistics describing arrival time variations, energy level fluctuations, and wave shape distortion were calculated and compared to values from analogous measurements using abdominal wall.[17] The received waveforms were then focused without compensation, with time-shift estimation and compensation in the measurement aperture, and with backpropagation followed by time-shift estimation and compensation to determine the effectiveness of time-shift compensation with and without wavefront backpropagation for the improvement of focusing.

I. METHOD

Breast tissue specimens were obtained fresh from reduction mammoplasty surgery and were stored frozen if not used immediately for measurements. The specimens came from regions of the breast away from the nipple and consisted of fat, glandular and connective tissue, and a surface covering of skin. Each specimen was essentially planar and had a surface area of at least 7×11 cm^2. The average thickness was 26.9 mm. The tissue donors were women ranging in age from 18 to 65 with a mean age of 34 years.

Measurements were carried out using the procedure detailed in Ref. 17 and summarized here for convenience. A breast tissue specimen was placed in the specimen holder with the skin facing the direction of the receiving transducer and pressurized to 500 psi for 30 min in order to dissolve any gas bubbles present in the tissue. The specimen holder was then mounted in the experimental chamber, which was maintained at 37 ± 1 °C throughout the measurement. Ultrasonic pulses emitted by a hemispheric transducer were received by a 128-element linear array immediately after propagation through the specimen. A two-dimensional area was scanned by translating the array in the elevation direction using an automated stage. At each elevation, the array elements were accessed sequentially by a multiplexer. The signal from each element was digitized into 12-bit samples for a period of 11.8 μs at a rate of 20 MHz. The signal was recorded 19 times at each element to permit noise reduction through signal averaging. The nominal center frequency was 3.75 MHz for each transducer and the -6-dB bandwidth of the received pulse was about 2.2 MHz. The element pitch in the receiving transducer was 0.72 mm and a reflecting mask reduced the receiving elevation to 1.44 mm. A period of about 35 min was required to record the signals from all 128 array elements at each of 32 elevations spaced 1.44 mm apart for a total of 4096 positions over a 92.16×46.08 mm^2 aperture. The total source–receiver separation was about 165 mm and the specimen–receiver gap was about 8 mm.

Three groups of measurements were made. The primary set consisted of independent measurements using nine different specimens. In addition, two specimens were employed for sequential measurements in which a 1-cm layer was removed from the bottom of the specimen before each subsequent measurement. For two other specimens, a pair of measurements was made with the source in each of two positions located 12 mm apart in the array direction.

Variations in pulse arrival time were calculated using the reference waveform method for arrival time estimation and differences in shape among the received waveforms were quantified using the waveform similarity factor as described in Ref. 16. Energy level fluctuations were calculated as described in Ref. 17. The calculations are outlined here to identify the main steps. A reference waveform was constructed for a set of data as an average of all the waveforms meeting a cross-correlation criterion for similarity. The reference pulse was then cross correlated with each of the original waveforms and an arrival time surface was calculated from the peaks of the correlation functions. Smoothing was done to remove questionable outlying points. A two-dimensional, fourth-order polynomial fit to the estimated arrival times was used to position a window on the original waveforms, and arrival time estimation was repeated using the windowed data. Geometric effects were removed by fitting a two-dimensional, fourth-order polynomial to the newly calculated arrival time surface and subtracting the result to obtain the arrival time fluctuations. Fluctuations in energy level across the received wavefront were calculated by summing the squared amplitudes of the windowed signals at each position, converting the results to decibel units, and subtracting a fitted two-dimensional, fourth-order polynomial from the result. This computation, however, did not employ the 20-dB restriction on the dynamic range as in Ref. 17, since no exceptionally low-energy values occurred. The waveform similarity factor, which ranges from an ideal value of 1 to a minimum of 0 and is insensitive to absolute amplitude and arrival time like a correlation coefficient, was computed for all the windowed waveforms throughout the aperture.

Two forms of compensation for wavefront distortion were applied to compare their effect on focusing. In one, time-shift estimation and compensation were performed directly in the receiving aperture. In the other, time-shift estimation and compensation were performed after the wavefront had been backpropagated to the point of maximum
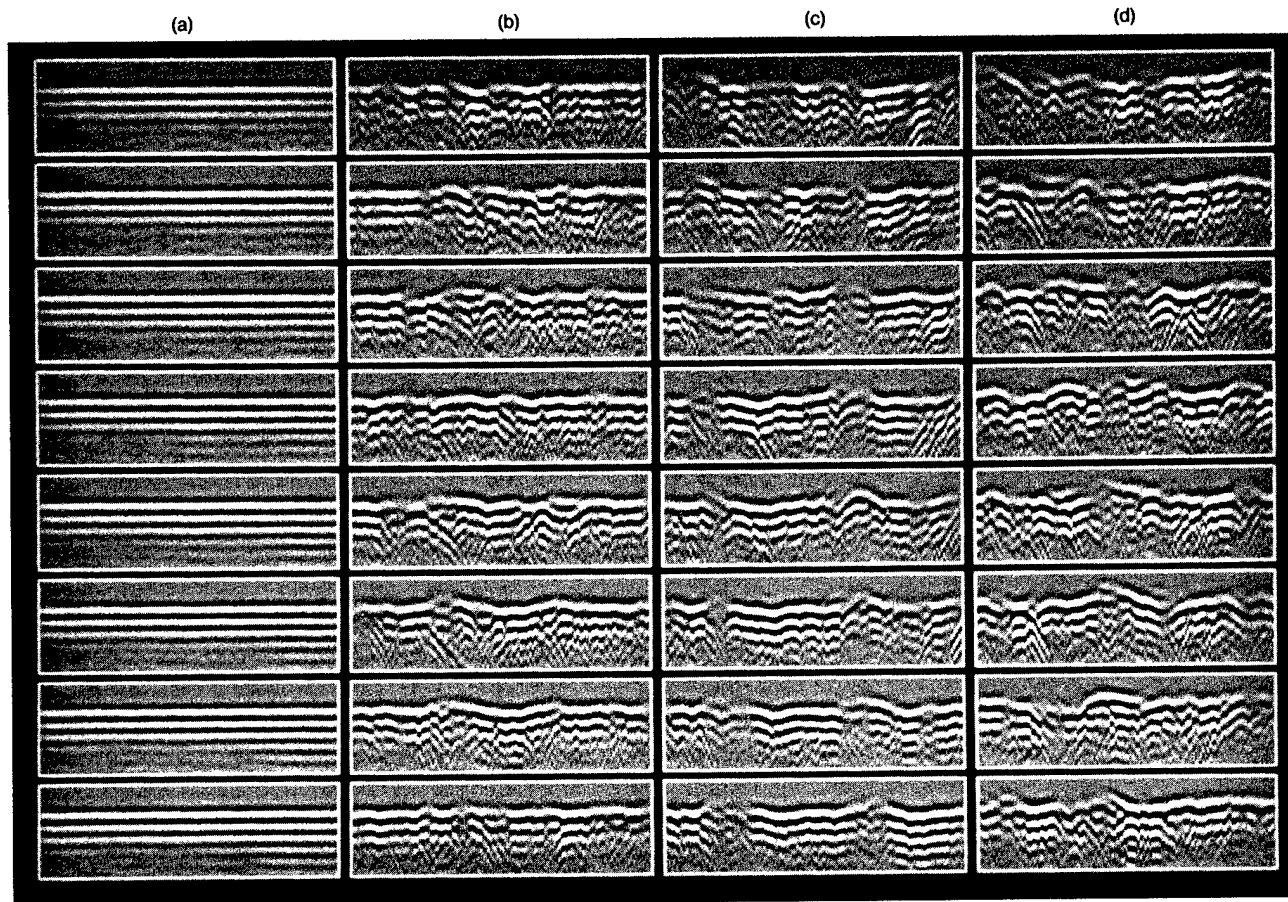
FIG. 1. Representative waveforms compensated for geometric travel time. (a) H_2O. (b) BRS 10. (c) BRS 8a. (d) BRS 8b. Each column of panels shows waveforms at sequential increments of 2.88 mm in elevation across the first half of the 46.08-mm aperture. At each elevation, the horizontal coordinate is the array direction and spans a distance of 92.16 mm in 0.72-mm increments while the vertical coordinate is time and spans an interval of 2.0 μs in 0.05-μs increments. Signal amplitude is shown linearly on a gray scale with the maximum signal in the two-dimensional aperture for each measurement represented by white and the corresponding negative value by black.

waveform similarity. The backpropagation used the angular spectrum method as described in Ref. 16. The reference waveform method was employed in both forms for time-shift estimation.

The efficacy of the two correction procedures, as well as the effect of the original distortion, were evaluated by focusing each set of data at 180 mm via a Fourier transform method as described in Ref. 18. Each focus was described by the -10, -20, and -30 dB effective radii, which are half the cube root of the product of the corresponding effective widths in the array, elevation, and time directions. The effective radius several dB down from the peak is a useful measure of point resolution while the effective radius many dB down from the peak is a measure of contrast resolution. The -10-dB peripheral energy ratio, which is the ratio of energy outside an ellipsoid bounded by the -10 dB effective widths to the energy inside that ellipsoid, was also used to describe each focus quantitatively. Since the energy outside a specified region around the main peak of the focus can be viewed as an integration of sidelobe intensity, the peripheral energy ratio is another measure of contrast resolution. Additionally, each focus was described by the 10% deviation level, which is the level at which the effective radius becomes 10% larger than that produced by ideal waveforms obtained for the data

set by replicating its average time-shift compensated waveform throughout the aperture. This level provides a measure of the degree to which the central region of actual focus is ideal.

II. RESULTS

Representative sets of waveforms recorded after transmission through breast tissue specimens and corrected for geometric arrival time are shown in Fig. 1 with corresponding representative water path waveforms to illustrate the range and combination of distortion levels encountered in this study. The water path waveforms in (a) show minimal arrival time and energy level fluctuation and nearly ideal waveform similarity. The tissue path waveforms in (b) exhibit low arrival time and energy level fluctuation and moderate waveform distortion. The waveforms in (c) have moderate arrival time variation, high energy level fluctuation, and low wave shape distortion. The waveforms in (d) show high arrival time and waveform distortion but moderate energy level fluctuation.

Arrival time fluctuations and energy level fluctuations produced by nine different breast tissue specimens are shown in Fig. 2 and statistics of these data as well as the waveform
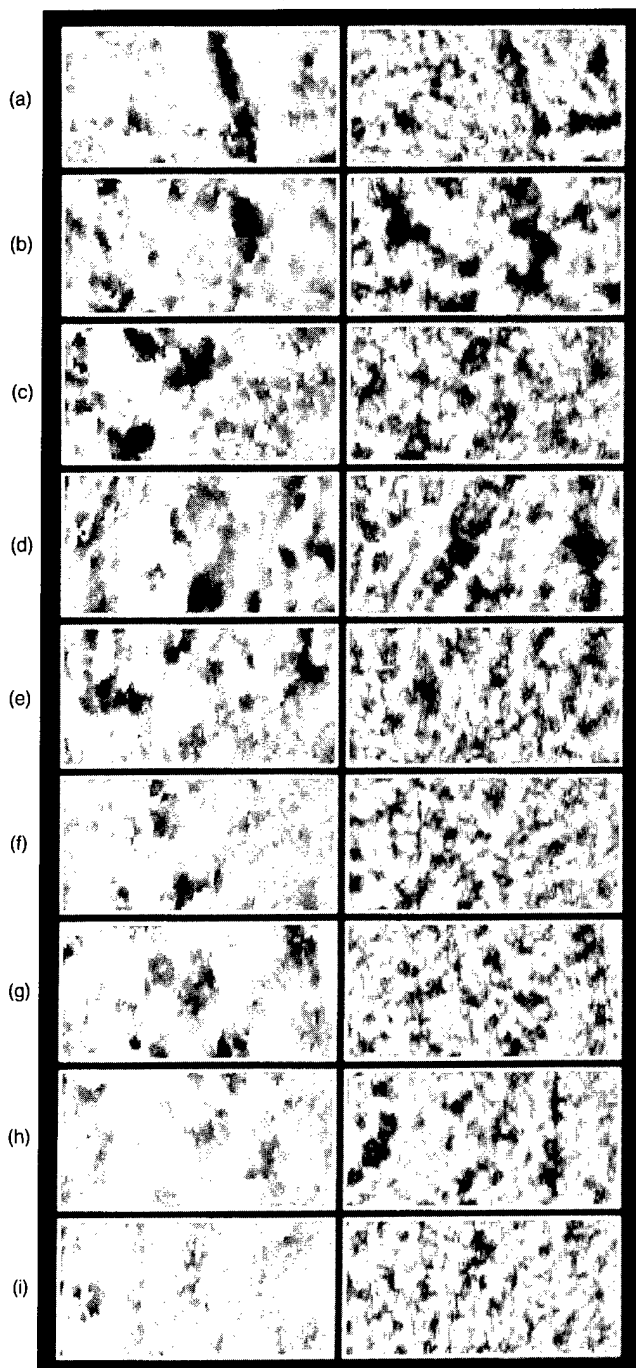
FIG. 2. Breast tissue path arrival time and energy level fluctuations for nine different specimens. (a) BRS 7. (b) BRS 8a. (c) BRS 8b. (d) BRS 9a. (e) BRS 9b. (f) BRS 10. (g) BRS 11. (h) BRS 13. (i) BRS 17. In the left panel of each pair, arrival time difference is shown on a linear scale with a maximum arrival time fluctuation of +150 ns represented by white and a minimum arrival time fluctuation of −150 ns represented by black. In the right panel of each pair, energy level fluctuations are shown on a log scale with a maximum positive excursion of +10 dB represented by white and a maximum negative excursion of −10 dB represented by black. In all panels, the horizontal coordinate is the array direction and spans a distance of 92.16 mm in 0.72-mm increments while the vertical coordinate corresponds to position of the array in elevation and spans a distance of 46.08 mm with points interpolated from measurements at 1.44-mm intervals to produce data at 0.72-mm increments.

similarity factor are given in Table I for each set of measured waveforms. The arrival time and energy level fluctuation patterns produced by a given specimen are roughly similar and the specimen-to-specimen variability is not great. Consistent with these observations, the effective arrival time and energy level fluctuation correlation lengths are similar for each specimen while the average waveform similarity factor has a small standard deviation.

Focal plane amplitude at representative instants of time are shown in Fig. 3 for typical measured waveforms that have been focused without compensation, with time-shift compensation in the aperture, and with time-shift compensation following backpropagation along with the focus obtained with ideal data. The spread of the focus obtained from uncompensated waveforms is large relative to the spread of the focus obtained from ideal data. The focus of the waveforms that have been time-shift compensated is more concentrated than that obtained from uncompensated waveforms and further concentration is obtained in the focus of waveforms that have been time-shift compensated following backpropagation, but the focus of each is not as concentrated as the focus obtained from ideal waveforms.

Effective radius curves of the focus obtained from the same typical measured waveforms for uncompensated, time-shift compensated, backpropagated and time-shift compensated, and ideal cases are shown in Fig. 4. The effective radius of the focus obtained without compensation departs from the ideal case by 10% at a level −5.2 dB below the peak. Time-shift compensation in the aperture reduces the 10% deviation level to −21.4 dB while time-shift compensation following backpropagation has a 10% deviation level of −25.8 dB and has an effective radius that is appreciably narrower at levels 30 to 40 dB below the peak.

The focus obtained with each of the nine different sets of data as well as the improvement in focus obtained using time-shift compensation in the aperture and using time-shift compensation after backpropagation are described by the parameters in Table II. The data show that time-shift compensation in the aperture and time-shift compensation following backpropagation result in an effective radius at the focus that is similar at the −10- and −20-dB levels but that time-shift compensation following backpropagation improves the −30-dB effective radius substantially over that obtained with time-shift compensation in the receiving aperture. This indicates that time-shift compensation with or without backpropagation yields about the same point resolution but that time-shift compensation after backpropagation improves the contrast resolution more than time-shift compensation in the receiving aperture does. The −10-dB peripheral energy ratio obtained with time-shift compensation in the aperture averages about 25% of that without compensation while the −10-dB peripheral energy ratio obtained with time-shift compensation following backpropagation is about 16% of that obtained without compensation. These peripheral energy ratios are another indication that the sidelobe level, and therefore the contrast ratio, is improved more by backpropagation followed by time-shift compensation than by time-shift compensation alone.

The arrival time and energy level fluctuations produced

TABLE I. Breast tissue path statistics of wavefront distortion produced by nine different specimens.

| Specimen number | Specimen thickness (mm) | Arrival time fluctuations | | | Energy level fluctuations | | | Waveform similarity factor |
		rms value (ns)	99.5% value (ns)	Effective corr. len. (mm)	rms value (dB)	99.5% value (dB)	Effective corr. len. (mm)	
7	15–25	63.1	196.2	5.82	4.86	14.21	3.20	0.940
8a	30–35	66.5	222.0	4.88	6.08	16.35	4.85	0.926
8b	30	85.6	252.0	5.16	5.02	12.99	3.41	0.869
9a	40	76.5	225.7	4.81	5.65	15.10	4.25	0.914
9b	35	79.5	276.6	4.20	4.98	13.09	3.04	0.883
10	20–25	59.5	212.8	3.38	4.67	12.75	2.87	0.908
11	20–25	70.7	252.2	4.73	4.77	12.44	2.75	0.903
13	15–20	49.3	160.8	3.36	4.72	13.44	3.39	0.930
17	20–25	50.5	162.3	2.40	4.53	12.46	2.46	0.918
mean	26.9	66.8	217.8	4.30	5.03	13.65	3.36	0.910
s.d.	7.7	12.6	39.9	1.07	0.51	1.33	0.76	0.023

by different thicknesses of tissue for two specimens are shown in Fig. 5 and described statistically in Table III. The arrival time fluctuations, energy level fluctuations, and waveform distortion increase with specimen thickness for all but one measurement. The arrival time and energy level fluctuation patterns for the different thicknesses of the same specimen are seen to vary considerably. The focus characteristics associated with these patterns are given in Table IV.

The arrival time and energy level fluctuations in the aperture and after backpropagation are shown in Fig. 6 for two specimens for each of two source positions 12 mm apart. The features in the fluctuation patterns obtained for each specimen are recognizable but shifted in the patterns obtained after the change in source position. The features are also changed but still identifiable after backpropagation. The similarity of the patterns is indicated quantitatively by the distortion statistics given in Table V and by the focus characteristics presented in Table VI for compensation using the time shifts calculated from the waveforms produced with the source at the focal position. The data in Table VI also show that compensation using the time shifts calculated from waveforms produced with the source 12 mm from the focal position is less effective than compensation using the time shifts from waveforms produced with the source at the position of focus.

III. DISCUSSION

The specimens studied here were sections of breast tissue rather than whole breasts. They came from unusually large breasts and ranged from 15–40 mm in thickness with nearly planar surfaces. Thus while the measurements illustrate elements of distortion produced by the breast, they may not describe conditions typically encountered in the clinic. Nevertheless, the information obtained in this study under precisely controlled experimental conditions adds to the available data about the ultrasonic wavefront distortion produced by the breast and should be useful in the development of imaging instruments with better resolution for improved ultrasonic diagnosis of breast disease.

Refraction at the specimen–water interfaces could contribute to the distortion measured in this transmission study. Prior investigations[16,17] have shown that this contribution is

negligible for abdominal wall, for which the surfaces are the skin and the peritoneum. The breast tissue specimens, however, had a cut surface on their lower side, so a special experiment was undertaken to investigate the contribution of refraction at this surface to the measured distortion. A thick specimen (BRS 9b) was selected and two measurements were made over approximately the same area, one with the skin side up and the other with the skin side down. Because of the 30-mm difference in propagation distance from the cut surface to the receiver in these measurements, differences in the distortion patterns from these measurements should be evident if refraction at the cut surface were an appreciable source of the distortion. In this experiment, however, the arrival time fluctuation rms values changed by less than 9% while the energy level fluctuation rms values and all correlation length values differed by less than 3%. These changes are within the range expected from reproducibility studies[17] given the uncertainty in the scan position and the differences in propagation path caused by inverting the specimen. The arrival time and energy level fluctuation maps from the two measurements were also remarkably similar. Therefore, the cut specimen surface, which is smoothed by the kapton membrane during measurements, is not considered to contribute significantly to the distortion measured for the breast specimens.

The data processing used to determine the wavefront distortion in this study employed the same calculated fourth-order polynomial references for the determination of arrival and energy fluctuation as were described in the report[17] of wavefront distortion by abdominal wall, but incorporated other improvements and extensions. The polynomial fits, as noted in Ref. 17, avoid the need for accurate knowledge about tissue dimensions and local acoustic characteristics and compensate for small misalignments and low spatial-frequency variations. The adaptive reference waveform method used to estimate arrival time differences in this paper is considered more accurate than the least-mean-square error method employed previously because, on average, fewer than 20% of the cross correlations computed for each abdominal wall data set using the adaptive reference waveform method had a peak value below 0.8, while about 30% of the
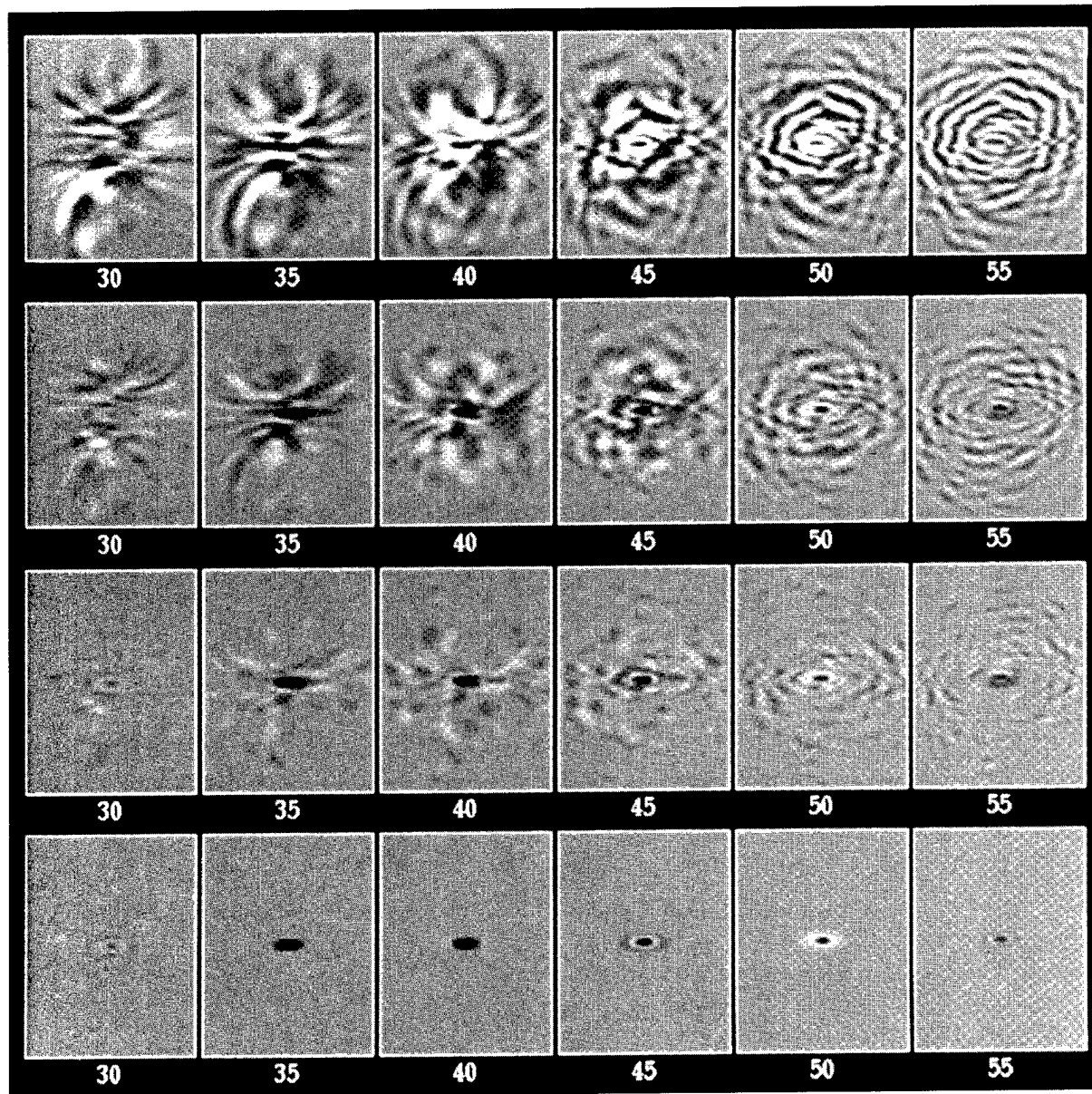
FIG. 3. Focal plane time histories of representative measured data (BRS 7). Each panel shows the bipolar distribution of signal amplitude as a shade of gray on a 50-dB log scale for each polarity in the focal plane at an instant of time. In all the panels, the horizontal coordinate is elevation and spans 37.504 mm while the vertical coordinate is in the array direction and spans 56.256 mm. The number beneath each panel identifies the (zero-origin) instant of time in the 128-point interval employed in the temporal Fourier transform. First row: Uncompensated data. Second row: After time-shift estimation and compensation in the aperture. Third row: After backpropagation of 40 mm followed by time-shift estimation and compensation. Fourth row: Ideal data.

peaks were below 0.8 for the least-mean-square error method. Also, the reference waveform method gives consistently lower estimates of distortion for water paths and yields superior focus characteristics when employed for time-shift compensation. Therefore, the reference waveform method was used in this study and the data in Ref. 16 were reprocessed using the reference waveform method to permit a comparison of the breast results discussed here with the abdominal wall data.

In the nine independent measurements reported here, an average ($\pm$s.d.) of 2807 ($\pm$228) waveforms or 68.5% of the 4096 received waveforms were similar enough to be incorporated into the final reference waveform. The average of the maximum value for correlations between each of the windowed waveforms and the final reference waveform was 0.868 ($\pm$0.018). This figure, calculated using all of the waveforms in the aperture before any smoothing, is similar to the average cross-correlation value of 0.86 calculated for neighboring waveforms in the 35 data sets selected for analysis by Freiburger et al.[5] in their two-dimensional study of the breast. An average of 758 ($\pm$183) or 18.5% of the calculated delays were deemed unacceptable because they deviated significantly from the overall delay surface. Of these, 495 (about two thirds) were replaced by delays from new peak searches while the remaining 263 (about one third) were corrected by smoothing.

The representative waveforms in Fig. 1 illustrate the variability of the wavefronts from which the characteristics
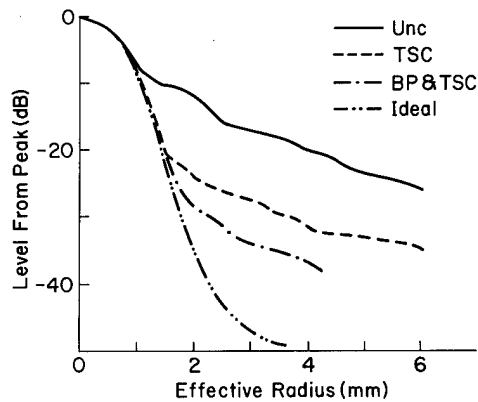
FIG. 4. Effective radius of the focus obtained with representative measured waveform data (BRS 7). Unc=uncompensated data. TSC=time-shift compensation in the receiving aperture. BP & TSC=backpropagation followed by time-shift compensation. Ideal=replication of a single average waveform throughout the receiving aperture.
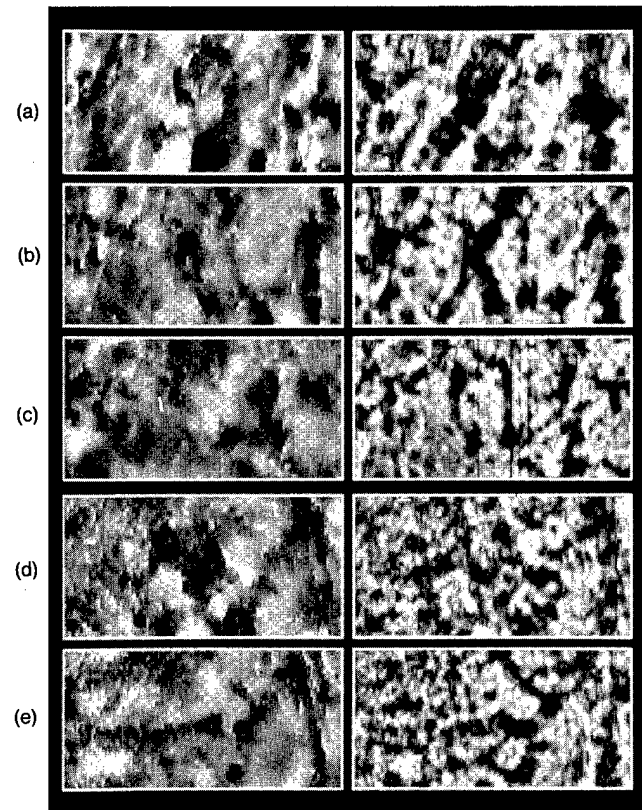

FIG. 5. Breast tissue path arrival time and energy level fluctuations for reductions of specimen thickness. (a)–(c) BRS 9a. (d) and (e) BRS 11. For each specimen, the results are presented from top to bottom in order of decreasing thickness. The format and scales in each pair of panels are the same as in Fig. 2.

of wavefront distortion have been found. The uniformity of the water path waveforms indicates that the error introduced by the apparatus is small compared to the fluctuations produced by the tissue path. The presence of tissue creates waveform shape changes which decorrelate the waveforms and introduce uncertainty in the estimation of arrival time. Improvement of arrival time estimation accuracy, and thus the correction of wavefront distortion, necessitates the removal of wave shape distortion and has motivated the introduction of a backpropagation step before time-shift compensation.

The arrival time and energy level fluctuation maps in Fig. 2 for the nine independent breast tissue measurements show the range of ultrasonic wavefront distortion patterns produced by human breast tissue in this study. These patterns have different characteristics from those reported[17] for the abdominal wall. For example, the breast arrival time fluctuation maps contain smaller features than those in the abdominal wall arrival time plots. The backgrounds of the breast arrival time and energy level fluctuation maps are also comprised of larger, more irregular patches than those in the abdominal wall plots. However, as is the case with the abdominal wall patterns, some breast arrival time fluctuation

map features appear to correlate with energy level fluctuations while others do not.

The bar charts in Fig. 7 compare the arrival time, energy level, and waveform distortion statistics for the nine breast specimen measurements to those in Ref. 17 for abdominal wall after recalculation using the reference waveform method. In general, breast tissue appears to cause more distortion than the abdominal wall. The rms arrival time fluctuations produced by the breast specimens in this study have

TABLE II. Breast tissue path focus characteristics for nine different specimens. r_e=effective radius. PER=peripheral energy ratio. Unc=uncompensated. TSC=time-shift compensation. BP=backpropagation followed by TSC. BP dist=distance of backpropagation for maximum waveform similarity.

| Specimen number | BP dist. (mm) | −10 dB r_e | | | −20 dB r_e | | | −30 dB r_e | | | −10 dB PER | | | 10% dev. lev. | | |
		Unc (mm)	TSC (mm)	BP (mm)	Unc (mm)	TSC (mm)	BP (mm)	Unc (mm)	TSC (mm)	BP (mm)	Unc	TSC	BP	Unc (dB)	TSC (dB)	BP (dB)
7	30	1.38	1.04	1.03	3.94	1.52	1.49	···	3.77	2.60	3.350	0.766	0.524	−5.2	−21.4	−25.8
8a	40	1.48	1.09	1.06	4.39	1.93	1.69	···	4.66	3.44	2.733	0.905	0.629	−1.0	−12.8	−17.0
8b	50	1.67	1.07	1.07	7.60	1.92	1.54	···	5.41	3.24	8.031	1.280	0.595	−0.9	−17.7	−22.0
9a	50	2.16	1.06	1.04	5.02	2.06	1.55	···	4.48	3.76	3.966	1.128	0.654	−4.9	−15.2	−20.9
9b	30	1.52	1.12	1.10	5.73	1.63	1.57	···	6.15	4.49	4.943	1.044	0.742	−1.0	−20.2	−23.7
10	40	1.17	1.04	1.03	3.39	1.59	1.50	···	3.64	2.54	3.957	0.968	0.592	−8.0	−19.4	−22.2
11	30	2.78	1.04	1.02	5.70	1.50	1.47	···	4.34	3.03	2.618	0.962	0.700	−3.4	−22.2	−24.4
13	30	1.16	1.05	1.03	2.71	1.54	1.48	5.92	3.74	2.89	1.766	0.712	0.554	−6.6	−20.1	−23.5
17	30	1.04	1.01	1.00	2.83	1.43	1.40	7.52	4.25	2.57	3.038	0.877	0.631	−13.3	−24.0	−26.1
mean		1.60	1.06	1.04	4.59	1.68	1.52	···	4.49	3.17	3.822	0.960	0.625	−4.9	−19.2	−22.8
s.d.		0.56	0.03	0.03	1.59	0.23	0.08	···	0.83	0.65	1.827	0.176	0.068	4.1	3.5	2.78

TABLE III. Breast tissue path statistics of wavefront distortion for reductions of specimen thickness.

Specimen number	Specimen thickness (mm)	Arrival time fluctuations			Energy level fluctuations			Waveform similarity factor
		rms value (ns)	99.5% value (ns)	Effective corr. len. (mm)	rms value (dB)	99.5% value (dB)	Effective corr. len. (mm)	
9a	40	76.5	225.7	4.81	5.65	15.10	4.25	0.914
	30	58.2	183.6	4.86	5.44	14.79	4.06	0.947
	18	54.6	157.6	5.12	5.01	15.31	2.92	0.965
11	20–25	70.7	252.2	4.73	4.77	12.44	2.75	0.903
	15	56.2	168.1	4.10	4.92	14.67	2.80	0.933

a mean of 66.8 ns, which is about 20% higher than the mean of 55.5 ns for the 14 abdominal wall samples. The rms energy level fluctuations produced by breast in this study have a mean value of 5.03 dB, which is about 39% higher than the mean of 3.62 dB for the abdominal wall. Wave shape distortion is also greater for the breast studies, which have a mean waveform similarity factor of 0.910 versus 0.938 for the abdominal wall.

The difference in the average thickness of breast and abdominal wall specimens may contribute to the difference in the average arrival time fluctuation rms values for the two types of specimens but appears to be a secondary source of the variation in energy level fluctuations. The mean thickness of the breast specimens is 25% larger than that of the abdominal walls and the average arrival time fluctuation of the breast specimens is about 20% larger than that of the abdominal walls. In addition, the arrival time fluctuation rms

values measured for specimens of both types having similar thicknesses were approximately the same. Thus the greater thickness of the breast specimens likely contributed importantly to the greater arrival time fluctuations observed in this study. However, a comparison of similarly thick breast and abdominal wall specimens revealed that the energy level fluctuation rms values of the breast specimens were larger in every case. This suggests that breast tissue produces more energy fluctuation per unit thickness than does abdominal wall tissue, so that the mean rms energy level fluctuation produced by the breast specimens would be greater than that of the abdominal walls even without the difference in their thicknesses.

The spatial distributions of arrival time and energy level fluctuations caused by breast and abdominal wall tissue differ as well. For the breast, the effective correlation length of arrival time fluctuation has a mean of 4.31 mm, which is
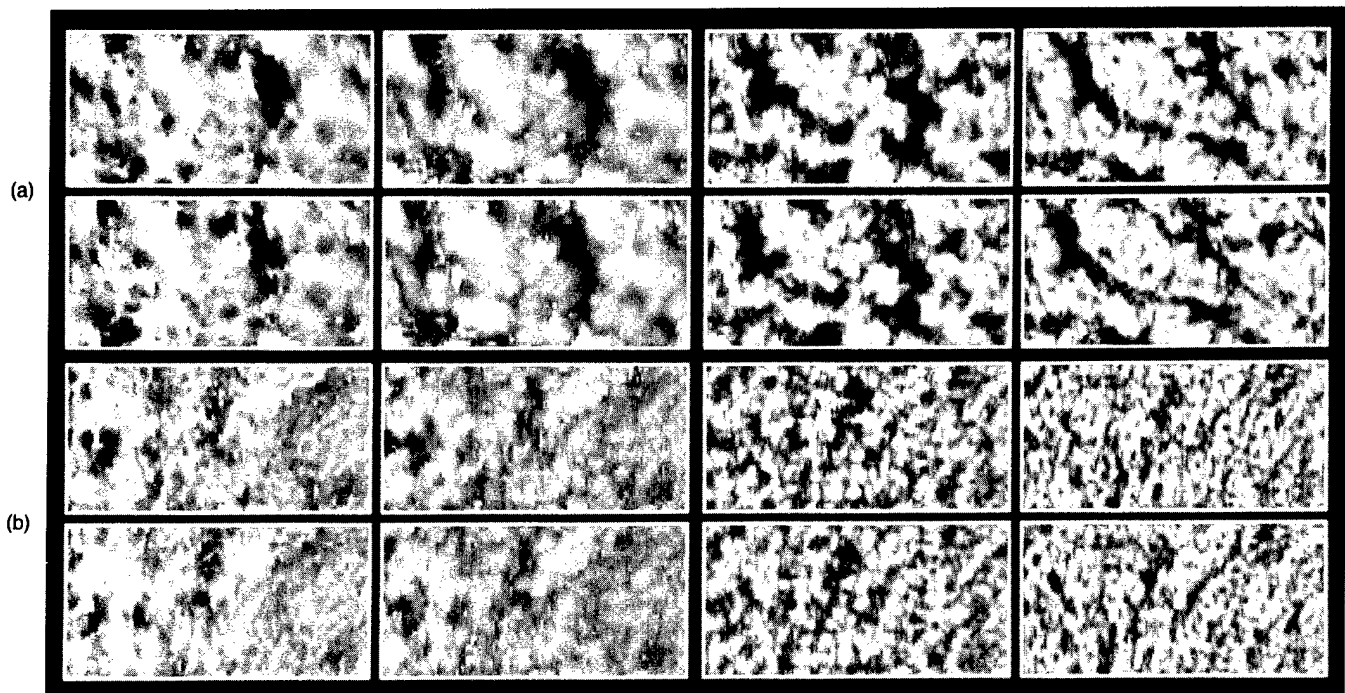

FIG. 6. Arrival time and energy level fluctuations before and after backpropagation for two source positions 12 mm apart. (a) BRS 8a. (b) BRS 17. For each specimen, the four-panel set on the left shows arrival time fluctuations and the four-panel set on the right shows the corresponding energy level fluctuations. In each four-panel set, the upper row shows the fluctuations with the source to the right and the lower row shows the fluctuations with the source to the left, while the left column shows the fluctuations in the measurement aperture and the right column shows the corresponding fluctuations after backpropagation to the distance of maximum waveform similarity. The scales in the panels are the same as in Fig. 2.

Hinkelman et al.: Ultrasonic pulse distortion by human breast

TABLE IV. Breast tissue path focus characteristics for reductions of specimen thickness. r_e=effective radius. PER=peripheral energy ratio. Unc =uncompensated. TSC=time-shift compensation. BP=backpropagation followed by TSC. BP Dist=distance of backpropagation for maximum waveform similarity.

Specimen number	BP dist. (mm)	−10 dB r_e			−20 dB r_e			−30 dB r_e			−10 dB PER			10% dev. lev.		
		Unc (mm)	TSC (mm)	BP (mm)	Unc (mm)	TSC (mm)	BP (mm)	Unc (mm)	TSC (mm)	BP (mm)	Unc	TSC	BP	Unc (dB)	TSC (dB)	BP (dB)
9a	50	2.16	1.06	1.04	5.02	1.06	1.55	···	4.48	3.76	3.966	1.128	0.654	−4.9	−15.2	−20.9
	40	1.14	1.04	1.03	3.66	1.73	1.56	7.20	3.82	2.89	2.372	0.830	0.540	−1.0	−17.0	−19.8
	20	1.56	1.03	1.03	4.10	1.49	1.46	8.06	4.21	2.94	2.954	0.673	0.508	−1.0	−22.1	−25.0
11	30	2.78	1.04	1.02	5.70	1.50	1.47	···	4.34	3.03	2.618	0.962	0.700	−3.4	−22.2	−24.4
	20	1.36	1.01	1.01	3.88	1.43	1.41	···	2.99	2.52	2.779	0.831	0.565	−5.6	−22.2	−24.2

26% smaller than the 5.78 mm mean calculated for the abdominal wall. The effective correlation length of energy level fluctuation for the breast has a mean of 3.36 mm, which is 45% larger than the abdominal wall correlation length of 2.31 mm. Consequently, the ratio of the average arrival time fluctuation effective correlation length to the average energy level fluctuation correlation length is 2.5 for the abdominal wall but only 1.3 for the breast specimens. This shows that the arrival time and energy level fluctuation correlation lengths for the breast are more similar to each other than are those for the abdominal wall.

The focus obtained with uncompensated breast tissue waveforms was predictably worse than that obtained with abdominal wall waveforms as is illustrated by the bar charts in Fig. 8 for uncompensated data. For example, the mean −10-dB peripheral energy ratio of the focused breast data was 3.8, nearly twice the average value of 2.1 computed for the abdominal data. Also, although not shown in Fig. 8, the mean −20-dB effective radius for the focused breast data was 4.6 mm while the corresponding value was 3.6 mm for the abdominal wall data. However, both the average breast and abdominal wall data sets first deviate 10% from their ideal effective radius curves at about −5 dB.

Time-shift compensation after backpropagation improves the focus of breast data more than time-shift compensation in the aperture does. However, in neither case is the average focus better than that of abdominal wall data after similar processing. The bar charts in Fig. 8 illustrate these trends. For example, the average 10% deviation level for breast data is reduced to −18.4 dB by time-shift compensation in the aperture and to −22.3 dB by time-shift compensation after backpropagation, but the corresponding values for the abdominal wall data are −23.5 and −26.3 dB, respectively. Similarly, time-shift compensation in the aperture reduces the average −10-dB peripheral energy ratio to 1.0

for the breast measurements and time-shift compensation after backpropagation further reduces it to 0.60, while the corresponding values for the abdominal wall measurements are 0.63 and 0.47. Although both compensation techniques improve the focus of ultrasonic waveforms that have propagated through breast tissue, time-shift compensation is more effective when performed after backpropagation.

The distance of backpropagation for maximum waveform similarity, i.e., the position of the equivalent phase screen in the propagation model employed here, is indicated by the data in Tables I and II (as well as in Tables III–VI) to be usually greater than the specimen thickness. However, as already noted, a distance of about 8 mm is present between the top surface of the specimen and the receiving aperture in the measurements. Adding 8 mm to the mean (±s.d.) specimen thickness given in Table II yields 34.9 (±7.7) mm while the mean backpropagation distance is 36.7 (±8.7) mm. Thus the data indicate that the optimum backpropagation distance is approximately the sum of the specimen thickness and the specimen-receiver separation, as in the case of the abdominal wall measurements.[16] The physical origin of this circumstance is currently unknown, although observations and experiments noted earlier indicate that the origin is not refraction at the specimen boundary. Additional studies are needed to provide information about the relation between tissue morphology and ultrasonic aberration.

The plots of arrival time and energy level fluctuations in Fig. 5 and the statistics of Table III show that reducing the tissue path length decreases the severity of the distortion produced in transmitted ultrasonic pulses. For both specimens 9a and 11, the magnitude of the measured arrival time and energy level fluctuations decreases as the tissue thickness is reduced while waveform similarity generally increases. The lack of similarity in the patterns of fluctuations as each specimen decreases in thickness is attributed to configurational

TABLE V. Breast tissue path statistics of wavefront distortion for two source positions 12 mm apart.

Specimen number	Source position	Arrival time fluctuations			Energy level fluctuations			Effective corr. len. (mm)	Waveform similarity factor
		Specimen thickness (mm)	rms value (ns)	99.5% value (ns)	Effective corr. len. (mm)	rms value (dB)	99.5% value (dB)		
8a	Left	30–35	66.5	222.0	4.88	6.08	16.35	4.85	0.926
	Right	30–35	65.2	216.0	4.17	6.01	15.11	4.79	0.916
17	Left	20–25	50.5	162.3	2.40	4.53	12.46	2.46	0.918
	Right	20–25	47.0	150.4	2.27	4.36	11.93	2.44	0.909

TABLE VI. Breast tissue path focus characteristics for two source positions. The numbers in parentheses are values obtained at one source position with waveforms compensated using time-shifts calculated with waveforms from the other source position. r_e=effective radius. PER=peripheral energy ratio. Unc=uncompensated. TSC=time-shift compensation. BP=backpropagation followed by TSC. BP Dist=distance of backpropagation for maximum waveform similarity.

Specimen number	Source position	BP dist. (mm)	−10 dB r_e Unc (mm)	−10 dB r_e TSC (mm)	−10 dB r_e BP (mm)	−20 dB r_e Unc (mm)	−20 dB r_e TSC (mm)	−20 dB r_e BP (mm)	−30 dB r_e Unc (mm)	−30 dB r_e TSC (mm)	−30 dB r_e BP (mm)	−10 dB PER Unc	−10 dB PER TSC	−10 dB PER BP	10% dev. lev. Unc (dB)	10% dev. lev. TSC (dB)	10% dev. lev. BP (dB)
8a	Left	40	1.48	1.09	1.06	4.39	1.93	1.69	···	4.66	3.44	2.73	0.91	0.63	−1.0	−12.8	−17.0
				(1.13)	(1.12)		(2.41)	(2.17)		(6.76)	(6.24)		(1.75)	(1.35)		(−7.7)	(−8.8)
	Right	40	1.43	1.05	1.05	4.61	1.82	1.55	···	4.86	3.74	3.17	1.05	0.67	−1.0	−16.4	−20.6
				(1.09)	(1.09)		(2.47)	(1.87)		(7.20)	(6.23)		(1.91)	(1.34)		(−11.5)	(−12.0)
17	Left	30	1.04	1.01	1.00	2.83	1.43	1.40	7.52	4.25	2.57	3.04	0.88	0.63	−13.3	−24.0	−26.1
				(0.99)	(1.00)		(1.76)	(1.67)		(6.98)	(5.46)		(2.29)	(1.75)		(−17.7)	(−19.1)
	Right	30	1.06	1.02	1.01	2.86	1.53	1.46	7.07	4.67	2.31	2.79	0.88	0.63	−12.3	−22.2	−28.1
				(1.01)	(1.02)		(1.75)	(1.64)		(···)	(5.92)		(2.32)	(1.78)		(−16.9)	(−18.4)

changes that result from removal of tissue slabs, differences in position of the specimen, and deformation from pressure applied when the specimen was sliced.

The nine separate breast measurements show a similar dependence of distortion on specimen thickness. Linear regression establishes significant relationships between breast tissue thickness and both rms arrival time and energy level fluctuation values, with correlation coefficients of 0.729 and 0.724, respectively. The energy level fluctuation correlation lengths are somewhat correlated to thickness as well. For the abdominal wall specimens, the arrival time fluctuation rms and correlation length values are moderately correlated to thickness and the waveform similarity factor is closely correlated, but energy fluctuation rms values and correlation lengths are not correlated to thickness. Since breast tissue consists of a heterogeneous arrangement of fat, glandular, and connective tissue while the abdominal wall is comprised of distinct fat and muscle layers, morphological differences are thought to be the reason for the observed differences in fluctuations produced by breast and abdominal wall.

The arrival time fluctuation maps in Fig. 6 and focus parameters in Table VI for measured wavefronts with different source positions demonstrate that the time shifts that best compensate the focus at one position may be less effective when the desired focus is moved 12 mm laterally and indicate that the use of backpropagation reduces this problem. Compensation in the aperture using the time-shifts calculated for the adjacent source position, i.e., cross compensation, improves the focus in every case, but is far less effective than compensation using the time-shifts calculated for the data set being corrected. Backpropagation increases the peak cross-correlation coefficient of the arrival time fluctuation map pairs to 0.728 from 0.564 for specimen 8a and to 0.568 from 0.426 for specimen 17. Cross compensation is more effective after backpropagation, but still does not achieve the level of focus improvement obtained using regular time-shift compensation in the aperture. This implies a limitation on the size of the region over which a single pattern of compensation is useful. For a related theoretical treatment that yields an expression for the size of the isoplanatic patch, see Ref. 19.

The statistics of the arrival time distortion measured in this study can be compared to the in vivo results of Freiburger et al. for a two-dimensional array.[5] Their mean rms phase distortion value of 55.3±14.0 ns obtained for 35 scans on the left breasts of seven volunteers is somewhat lower than the 66.8±12.6 ns determined here for nine breast specimens. However, their tissue paths had a mean length of 78.8±21.4 mm,[20] which is much longer than those measured here. As discussed above, a longer path is expected to produce larger fluctuations in arrival time. Also, their receiver elements were 0.51×3.50 mm^2, which corresponds to a surface area 1.7 times larger than that of the elements used in this study. A larger measurement spot is associated with a decrease in measured arrival time fluctuations because the fluctuations are averaged over the measurement spot, as detailed in a study[21] that emulated the outputs of elements of various sizes in one-dimensional apertures from the measured outputs of smaller elements in a two-dimensional aperture. Nevertheless, the 4.31±1.08-mm phase correlation length measured here is similar to the 4.21±1.14-mm value obtained by Freiburger et al.[5] in the azimuthal direction. The effects of the distortion measured in the two cases on the resulting focus are not comparable because of substantial differences in focusing parameters.

The wavefront distortion and focus degradation found in this study may also be compared with the already cited in vivo results of Zhu and Steinberg.[6-9] Their observation of severe amplitude distortion accompanying phase distortion in narrow-band measurements is analogous to energy level fluctuations accompanying arrival time fluctuations in the present wideband measurements. The emphasis that Zhu and Steinberg give to the influence of amplitude distortion in their analysis is strongly supported by the new data given here. Zhu and Steinberg also showed representative reconstructions of source profiles that are analogous in the present study to effective width curves of the uncompensated focus in the array direction. The high degradation of the source profiles illustrated in their reports is qualitatively similar to the poor focus characteristics given here for uncompensated data. However, a quantitative comparison of source profile and focus width characteristics is not readily made with the
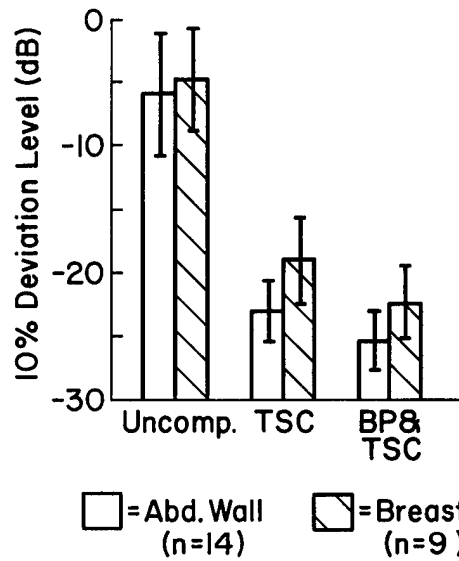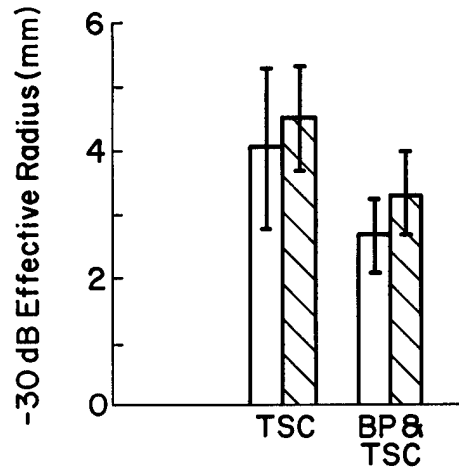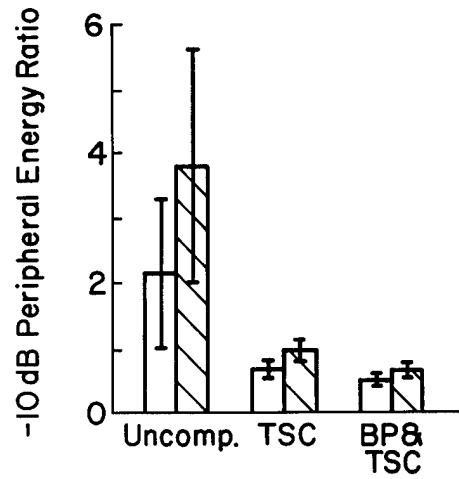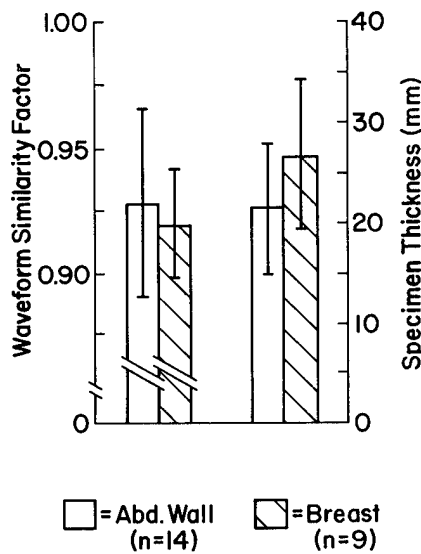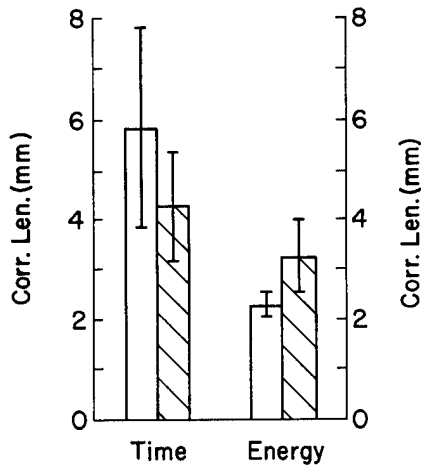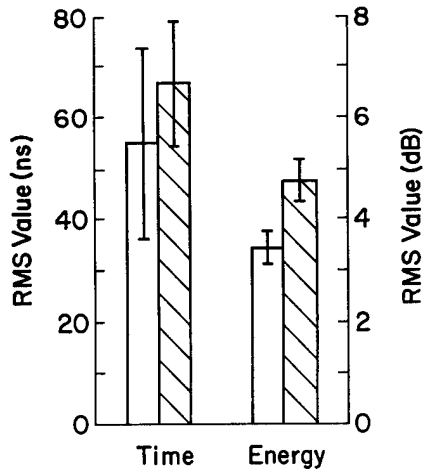
FIG. 7. Comparison of breast and abdominal wall wavefront distortion statistics. In each chart, the average and standard deviation of the measurements within each group are shown.

FIG. 8. Comparison of breast and abdominal wall focus statistics. In each chart, the average and standard deviation of the measurements within each group are shown. Uncomp=uncompensated waveforms. TSC=time-shift compensation. BP&TSC=backpropagation before time-shift compensation.

published Zhu and Steinberg data because they employed different focus descriptors, as well as relatively narrow-band pulses, a larger measurement spot size, and significantly longer tissue paths.

IV. CONCLUSION

Ultrasonic wavefront distortion produced by transmission through breast specimens has been investigated by recording and processing pulsed waveforms to obtain maps and statistics of arrival time and energy level fluctuations. The average rms value of the arrival time fluctuations was similar to that for abdominal wall specimens of like thickness while the average rms value of energy level fluctuations was greater than that for similarly thick abdominal wall specimens. The average effective correlation length of the arrival time fluctuations for breast specimens was shorter than that for the abdominal wall while the average effective correlation length of the energy level fluctuations was larger than that for the abdominal wall. The breast tissue waveforms showed more variation than the abdominal wall waveforms. Time-shift compensation in the aperture improved the focus of pulses distorted by breast tissue specimens and time-shift compensation after backpropagation brought the focus closer to the ideal, but the improvement was generally less than that obtained for distortion produced by abdominal wall. Repeated study of specimens with reduction of thickness showed that pulse arrival times, energy levels, and wave shape are increasingly altered as tissue path length increases. Measurements using different source positions indicated that time-shift compensation in the aperture with arrival times estimated when the source was 12 mm away from the focal position produced little improvement in the focus, but that backpropagation made such cross compensation more effective, although still less effective than self-compensation in the receiving aperture. These results demonstrate that ultrasonic propagation through breast tissue produces appreciable arrival time and energy level fluctuations and provide important new information about the variety and range of these fluctuations. They also show that time-shift compensation improves the focus of waveforms distorted by breast tissue, especially when the compensation is applied after wavefront backpropagation.

[1] P. M. Jokich, D. L. Monticciolo, and Y. T. Adler, "Breast Ultrasonography," Radiol. Clin. North Am. **30**(5), 993–1009 (1992).

[2] W. J. Donegan, "Evaluation of a Palpable Breast Mass," N. Engl. J. Med. **327**(13), 937–942 (1992).

[3] M. Moshfeghi and R. C. Waag, "In-Vivo and In-Vitro Ultrasound Beam Distortion Measurements of a Large Aperture and a Conventional Aperture Focussed Transducer," Ultrasound Med. Biol. **14**(5), 417–430 (1988).

[4] G. E. Trahey, P. D. Freiburger, L. F. Nock, and D. C. Sullivan, "In Vivo Measurements of Ultrasonic Beam Distortion in the Breast," Ultrason. Imag. **13**(1), 71–90 (1991).

[5] P. D. Freiburger, D. C. Sullivan, B. H. LeBlanc, S. W. Smith, and G. E. Trahey, "Two Dimensional Ultrasonic Beam Distortion in the Breast: In Vivo Measurements and Effects," Ultrason. Imag. **14**(4), 398–414 (1992).

[6] Q. Zhu and B. D. Steinberg, "Large-Transducer Measurements of Wavefront Distortion in the Female Breast," Ultrason. Imag. **14**(3), 276–299 (1992).

[7] Q. Zhu and B. D. Steinberg, "Wavefront Amplitude Distribution in the Female Breast," J. Acoust. Soc. Am. **96**, 1–9 (1994).

[8] Q. Zhu and B. D. Steinberg, "Wavefront Amplitude Distortion and Image Sidelobe Levels—Part I: Theory and Computer Simulations," IEEE Trans. Ultrason. Ferroelect. Freq. Control **40**(6), 747–753 (1993).

[9] Q. Zhu, B. D. Steinberg, and Ronald Arenson, "Wavefront Amplitude Distortion and Image Sidelobe Levels—Part II: In Vivo Experiments," IEEE Trans. Ultrason. Ferroelect. Freq. Control **40**(6), 754–762 (1993).

[10] S. W. Flax and M. O'Donnell, "Phase-Aberration Correction Using Signals from Point Reflectors and Diffuse Scatterers: Basic Principles," IEEE Trans. Ultrason. Ferroelect. Freq. Control **35**(6), 758–767 (1988).

[11] M. O'Donnell and S. W. Flax, "Phase-Aberration Correction Using Signals from Point Reflectors and Diffuse Scatterers: Measurements," IEEE Trans. Ultrason. Ferroelect. Freq. Control **35**(6), 768–774 (1988).

[12] L. Nock, G. E. Trahey, and S. W. Smith, "Phase Aberration Correction in Medical Ultrasound Using Speckle Brightness as a Quality Factor," J. Acoust. Soc. Am. **85**, 1819–1833 (1989).

[13] D. Zhao and G. E. Trahey, "A Statistical Analysis of Phase Aberration Correction Using Image Quality Factors in Coherent Imaging Systems," IEEE Trans. Med. Imag. **11**(3), 446–452 (1992).

[14] M. Fink, "Time Reversal of Ultrasonic Fields—Part I: Basic Principles," IEEE Trans. Ultrason. Ferroelect. Freq. Control **39**(5), 555–566 (1992).

[15] F. W. Wu, J.-L. Thomas, and M. Fink, "Time Reversal of Ultrasonic Fields—Part II: Experimental Results," IEEE Trans. Ultrason. Ferroelect. Freq. Control **39**(5), 567–578 (1992).

[16] D.-L. Liu and R. C. Waag, "Correction of Ultrasonic Wavefront Distortion Using Backpropagation and a Reference Waveform Method for Time-Shift Compensation," J. Acoust. Soc. Am. **96**, 649–660 (1994).

[17] L. M. Hinkelman, D.-L. Liu, L. A. Metlay, and R. C. Waag, "Measurements of Ultrasonic Pulse Arrival Time and Energy Level Variations Produced by Propagation through Abdominal Wall," J. Acoust. Soc. Am. **95**, 530–541 (1994).

[18] D.-L. Liu and R. C. Waag, "Time-Shift Compensation of Ultrasonic Pulse Focus Degradation Using Least-Mean-Square Error Estimates of Arrival Time," J. Acoust. Soc. Am. **95**, 542–555 (1994).

[19] B. D. Steinberg and A. K. Luthra, "Simple Theory of the Effects of Medium Turbulence upon Scanning with an Adaptive Phased Array," J. Acoust. Soc. Am. **71**, 630–634 (1982).

[20] P. D. Freiburger (personal communication, 20 April 1994).

[21] D.-L. Liu and R. C. Waag, "A Comparison of Wavefront Distortion and Compensation in One-Dimensional and Two-Dimensional Apertures," IEEE Trans. Ultrason. Ferroelect. Freq. Control (in press).

ESTIMATION AND CORRECTION OF ULTRASONIC

WAVEFRONT DISTORTION USING PULSE-ECHO DATA

RECEIVED IN A TWO-DIMENSIONAL APERTURE

D.-L. Donald Liu*

Robert C. Waag

Department of Electrical Engineering

University of Rochester

Rochester, New York 14627

---

* Currently with Siemens Medical Systems Ultrasound Group, Issaquah, WA 98029

ABSTRACT

Pulse-echo measurements from random scattering and from a point target have been used to quantify transmitter beam size effects and isoplanatic patch size as well as to evaluate the performance of different aberration compensation techniques. Measurements were made using a single-element transmitter with a diameter of 1/2″, 1″, or 2″, each focused at 3″. A tissue-mimicking scattering phantom or a point target was used to produce echoes that were received in a two-dimensional aperture synthesized by scanning a linear array. A specimen of abdominal wall was placed in the reception path to produce aberration. B-scan images were formed with no compensation, with time-shift compensation in the receiving aperture, and with backpropagation followed by time-shift compensation. The isoplanatic patch size was estimated by compensating the focus of a test point target with the parameters estimated for an original point target position, and observing the deterioration of compensation effects with increasing distance between the test and the original point targets. The results of the measurements using different transmitter diameters quantify the improvement of time-delay estimation with the increase in wavefront coherence that accompanies decreased transmitter beam size. For 7 specimens, the average isoplanatic patch size determined from a 10% increase in the −10 dB effective diameter was 16.7 mm in the azimuthal direction and 39.0 mm in the range direction. These sizes increased after backpropagation to 19.0 mm and 41.4 mm, respectively. For the 1/2″, 1″, and 2″ diameter transmitters, the average contrast ratio improvement was 2.0 dB, 2.1 dB, and 2.8 dB, respectively, with time-shift compensation, and 2.3 dB, 2.7 dB, and 3.5 dB, respectively, with backpropagation of 20 mm followed by time-delay estimation and compensation. The investigation indicates that a tightly focused transmitter beam is necessary to create a scattered wavefront satisfactory for time-shift estimation, the isoplanatic patch is about twice as long in the range direction as in the azimuthal direction, and backpropagation followed by time-shift compensation provides better compensation of distortion than time-shift compensation alone.

INTRODUCTION

The estimation and correction of ultrasonic wavefront distortion caused by propagation through an inhomogeneous medium (as most tissues are) has been studied by academic and industrial researchers using various approaches. Some started from data measured with one-dimensional, clinical arrays having a large elevation. Some developed algorithms and systems with emphasis on real-time implementation. Some measured the distortion effects using a relatively controlled yet clinically relevant configuration. This latter approach has yielded transmission measurements using a spherical wave source and two-dimensional receiving aperture with a small (about 1 mm^2) measurement spot size and has provided basic data that describe the characteristics of wavefront aberration caused by tissue. The next logical step is to apply this information to correct for tissue aberration in a pulse-echo setting using random scattering, similar to conditions commonly encountered in diagnostic imaging. A study that does so and aims to provide considerable insight into aberration correction in the pulse-echo mode is reported here.

Although the existence of wavefront distortion has been known since almost the beginning of b-scan imaging [1,2], the need for compensation of this distortion has only recently become great with the advent of large, high-frequency arrays. Extensive investigation of aberration measurement and correction conducted in view of this need started about 10 years ago. Flax and O'Donnell [3] measured the time distortion based on the cross-correlation of waveforms received by neighboring elements of a linear array. Waag, et al. [4,5] reported measurements and analysis of wavefront distortion caused by propagation through abdominal wall and calf liver. Nock, et al. [6] proposed a maximum brightness method that was implemented in real-time. Focus compensation in these early studies concentrated on the correction of arrival time fluctuations. However, later studies [7–11] have shown that correction of arrival time fluctuation alone is not sufficient to compensate fully for ultrasonic distortion caused by propagation through an extended thickness of tissue. Measurements [7,8] indicate that the propagated wavefront contains not only time-shift aberration but also substantial energy level fluctuation and significant waveform changes. Focusing studies [9,10] show that time-shift compensation improves mainly the point resolution but that the sidelobes remain considerably higher than that of an ideal focus. Based on these results and observations, an improved wavefront distortion model that

3

consists of a time-shifting screen placed some unknown distance away from the measurement aperture was proposed and employed with measured data [12]. The results obtained using this model with abdominal-wall data [12] and breast data [9] suggest that a better way to compensate for wavefront distortion is first to backpropagate the wavefront by an appropriate distance, and then to time-shift compensate the wavefront at that distance.

Accurate estimation of the distortion is required to model and compensate the distortion effectively. This estimation, which includes calculation of arrival time fluctuation from wavefront data, is a difficult task, since severe waveform distortion can invalidate the usual definition and estimation of arrival time. Additionally, for randomly distributed scatterers illuminated by a focused beam, the scattered signals are known to decorrelate with increasing spatial distance between the measurement spots. The degree of decorrelation is related to the illumination beam size, and is governed by the van Cittert-Zernike theorem [13,14] under the assumptions of incoherent scattering and a homogeneous propagation path. Another factor that influences the perceived distortion effect is the size of receiver elements. Simulations of a one-dimensional aperture using measurements in a two-dimensional aperture have shown [15] that accurate measurement of distortion requires small size elements to avoid significant spatial averaging over the element surface. All the foregoing points must be addressed for the appropriate measurement, estimation, and correction of wavefront distortion.

The application of wavefront aberration correction in *in vivo* clinical diagnostic imaging requires the estimation of a distortion profile using randomly scattered waveforms produced by a beam of illumination. The distortion effect of the inhomogeneous medium may vary for different regions of the scattering medium because wavefronts originating from different positions propagate through different paths in the inhomogeneous medium and are distorted differently. Critical questions for the practical implementation of wavefront aberration correction are the following. How accurately can the distortion profile be estimated? For how large a spatial region is a single estimation suitable? How much improvement can be expected by distortion compensation? The answer to these questions naturally depends on the severity of the distortion and the compensation technique being used. In this paper, pulse-echo experiments and calculations designed to address the above questions are described to provide quantitative results about the following.

4

1. The effect of the transmitter beam size on the coherence of scattered wavefront and on the accuracy of time-delay estimation.

2. The isoplanatic patch size, *i.e.*, the size of a region for which the distortion effect can be corrected using the same set of parameters.

3. The use of backpropagation in the pulse-echo mode using randomly scattered waveforms, and the effectiveness of time-shift compensation with and without backpropagation.

The organization of this paper is the following. First, data acquisition is described along with the considerations of experimental design. Next, issues in data processing, particularly in time-delay estimation, are discussed, and the formation of b-scan images with dynamic receive focusing is described for the particular geometry used in the measurements. Also, methods used for the evaluation of wavefront coherence, image contrast ratio, and point focus are described. Then, results from seven specimens of abdominal wall are presented for waveform similarity factor, rms arrival time fluctuation, isoplanatic patch size, and contrast ratio. The results are next discussed and finally conclusions are drawn.

I. DATA ACQUISITION

A. Measurement Configuration

The measurement apparatus consisted of a transmitter, a scattering phantom, a specimen, and a receiving linear array, configured as shown in Fig. 1. The apparatus is immersed in distilled water with temperature maintained at 30°C using a heater and circulation. In this configuration, the transmit beam is unperturbed and only the receive beam is distorted by the aberration medium, for which specimens of human abdominal wall were used. The arrangement permits control of the transmit beam and compensation of the receive beam by different techniques using data measured in a two-dimensional aperture. Two scan movements used in the measurement are illustrated in Fig. 2. The first movement scans the linear array to form a two-dimensional receiving aperture. The second movement, analogous to conventional b-scan imaging, scans the transmitter and the receiving aperture together to form different scan lines.

The transmit beam was produced using a single element transducer and the beam size was controlled by using transducers of different diameters, *i.e.*, 1/2″, 1″, and 2″, each focused at 3″. The fixture was designed so that the focal point of each transducer was at the same spatial point. Due to the different electrical impedances of the transducers, a custom-made pulser with individual impedance matching networks for each transducer was used to maximize the energy radiated into the medium.

A tissue-mimicking phantom with a 10 mm-diameter scatterer-free cylinder to simulate a blood vessel or a cyst was used as the scattering medium. To increase scattering signal strength and reduce attenuation in the phantom, the phantom was made of agar (40 grams per liter of water) and glass spheres of diameters around 75~90 μm (4 grams per liter of agar solution). This resulted in about 10 dB greater signal strength compared to previously used graphite-gel phantoms. The final signal-to-noise ratio achieved with the measurement system averaged 21.9 dB, 22.9 dB, and 19.0 dB for seven specimens of abdominal wall using the 1/2″, 1″, and 2″ transducer, respectively.

In place of the phantom, a point target was positioned at the focal point of the transmitting transducer to produce a spherical scattered wavefront with the highest possible spatial coherence so that time delays estimated from such a wavefront could be used as a

6

standard against which time delays estimated using random scattering from the phantom could be compared.

A diagram of the data acquisition system is shown in Fig. 3. A free-running oscillator, synchronized with the 20 MHz clock signal of the analog-to-digital (A/D) converter, triggered a custom-made pulser that excited the single-element transducers through impedance matching networks individually tuned for each transducer. The scattered signal was received by a 128-element linear array and the elements were individually accessed using a multiplexer. The pitch of the array is 0.72 mm and the element size in the elevation direction was limited to 1.00 mm to avoid excessive spatial averaging across the element surface. The output from the accessed element then passed through a TGC amplifier and a fixed gain amplifier. The signal was next A/D converted with a precision of 12 bits at a rate of 20 MHz. The measurement at each element was repeated 6 times (determined by hardware) so that data averaging could be used to reduce electronic noise and the results were stored in a waveform memory. After data were acquired for all elements at each elevation and scan position, the data were transferred to a PC via GPIB, averaged, and stored on a disk temporarily before being sent (via Internet) for subsequent processing on an IBM SP2 computer. Parameters of the measurement configuration are tabulated in Table I. As indicated in Table I and shown in Fig. 2, the linear array was moved over 12 elevation positions to form the two-dimensional receiving aperture, and the transmitter and linear array assembly was moved over 20 positions to obtain 20 scan lines. Because the scan movement was mechanical, the scan step size could be chosen independent of the element pitch of the linear array. The size of each dataset was (2 bytes/sample) × (776 samples/element) × (66 elements/elevation) × (12 elevations/scan) × (20 scans), or about 25 MBytes.

A water-path point target echo waveform and its amplitude spectrum are presented in Fig. 4 to show the center frequency and bandwidth of the measurement system. Typical pulse-echo wavefronts obtained using a point target and using the random scattering phantom are shown in Fig. 5 for a representative tissue path.

B. Measurements for Evaluating Isoplanatic Patch Size

The point target positioned at the center of the transmit focus provided a means for measuring the isoplanatic patch size, *i.e.*, the size of the scattering region for which the distortion effect of the inhomogeneous medium is about the same.

7

Data for the evaluation of isoplanatic patch size in the range direction were obtained by moving the transmitter/point-target assembly in the vertical direction manually and measuring the scattered wavefront in a two-dimensional aperture for each point target position. See Fig. 6. The topmost point target position was about 81 mm below the aperture, and 5 sequential positions were measured in an increment of 7 mm, yielding 5 sets of wavefront data.

The sets of wavefront data were independently corrected for geometric path length differences, after which all the wavefronts were essentially flat having only small fluctuations from wavefront distortion. The geometric correction was performed by estimating an arrival time surface, fitting a spherical surface to the arrival time surface, and shifting the waveforms with the fitted delays. Next, a time delay map was estimated for the wavefront corresponding to the topmost point target, and this was used to time shift each of the 5 wavefronts. In this way, the wavefront corresponding to the topmost point target was time-shift compensated with delays estimated from itself, which is called here *self* compensation, and the other wavefronts were time-shift compensated with delays estimated for a different point target position, which is called here *cross* compensation. In cross compensation, a *test* point target wavefront is said for brevity to be compensated with distortion parameters estimated for the *original* point target. The compensated wavefronts were then each focused to produce an image of the point target.

The data for the evaluation of isoplanatic patch size in the azimuthal direction was similarly obtained by scanning the transmitter and point-target assembly in the horizontal or array direction. During the scan, the specimen was stationary while the receiving array translated with the transmitter. This resulted in a relative shift between the specimen and the two-dimensional receiving aperture. In order to maintain interrogation of the same tissue path, a different portion of the array was used for forming the receiving aperture. Therefore, the azimuthal scan step size was made to be the same as the element pitch in the linear array, *i.e.*, 0.72 mm, and with each scan, the portion of array used to form the receiving aperture was shifted by one element in the direction opposite to the scan movement. The number of such scans was 20. The vertical distance from the point target to the aperture in these measurements was about 95 mm. In processing, the 20 measured wavefronts were each corrected for geometric path length difference, and a time-shift map

8

was estimated for the first wavefront. This map was used to time-shift compensate each of the 20 wavefronts. The time-shift compensated wavefronts were then each focused to produce an image of the point target.

II. DATA PROCESSING

A. Time-Delay Estimation

Time-delay estimation is the central issue in data processing. If time delays are not estimated correctly, the full potential improvement that results from time-shift compensation (with or without backpropagation) cannot be achieved, and the effectiveness of techniques that employ time-shift compensation cannot be properly assessed. Similarly, for the measurement of isoplanatic patch size, if the point target focus is not optimal after compensation with time delays estimated for that position, then, as the point target moves away, the deterioration of the compensation effect will be less noticeable, leading to an overestimation of the isoplanatic patch size.

The problem of time-delay estimation for a two-dimensional array of $M \times N$ waveforms $s_i(t)$ for $i = 1 \sim MN$ can be posed as an optimization problem in which the maximization of

$$J(\tau_1, \tau_2, \cdots, \tau_{MN}) = \int_{-\infty}^{+\infty} \left[\sum_{i=1}^{MN} s_i(t - \tau_i) \right]^2 dt$$

is sought subject to a smoothness requirement on the map of τ_i's. The quantity J can be interpreted as the energy of the coherent sum of the aligned waveforms, and is proportional to the waveform similarity factor defined in Ref. [12] and the focusing criterion defined in Ref. [16]. The smoothness requirement on the τ_i map comes from the observation that, since the time delay aberration is induced by a specimen of soft tissue with smooth structures, a two-dimensional map of arrival time is not likely to contain any abrupt jumps or local points that are very different from their neighboring points. This smoothness requirement is experimentally supported by the smoothness of point target wavefronts measured through tissue specimens. Although direct optimization of J is computationally intensive and difficult because numerous local minima exist, this general point of view was used to guide the development of specific time delay estimation algorithms for the study reported here.

In the current study, time delays were estimated from two types of wavefront: point target wavefronts and random scattering wavefronts. These two types of wavefront have different spatial coherence properties in addition to different temporal waveform shapes.

10

The point target wavefront consists of a single pulse and is coherent throughout the aperture (that is, in the absence of propagation aberration, all the pulses are the same), whereas the scattering wavefront consists of random waveforms that lasts a long time and has a spatial coherence that decreases with increasing separation between points in the aperture. Previously, the authors have proposed two different algorithms for time-delay estimation in a two-dimensional aperture. These are the least-mean-square-error method [10] and the reference waveform method [12]. Both methods employed cross-correlation followed by spline interpolation to detect the peak as the basic means to find the relative time delay between two given waveforms. However, the reference waveform method assumes all the waveforms in the aperture to be the same, and so is only suitable for point target wavefronts. Another method known in the literature for time-delay estimation in a two-dimensional aperture is the row-sum method [17], but this method in its presented form also assumes the waveforms to be similar throughout each row and is considered to be suitable only for point target wavefronts.

The least-mean-square-error method uses relative time delays for neighboring waveforms and requires the waveforms be only locally coherent. This method is suited for estimating the arrival time surface for a wavefront that arises from random scattering. The difficulty with this method is the need to determine an arrival time when neighboring waveforms are poorly correlated. In the current study, the least-mean-square-error method was improved by using reference points to guide the search for peak positions in the cross-correlation function and using weights in the solution of the least-squares problem. The improved version was used as the method for time-delay estimation.

The least-mean-square-error method for time delay estimation in a two-dimensional aperture has been described elsewhere [10], so only an outline is provided here. In this method, for a rectangular array of waveforms, relative time delays are found for neighboring waveforms in the horizontal, vertical, and the two diagonal directions. These relative time delays are then used to write a set of linear equations of the form $\tau_i - \tau_j = d_{ij}$, where τ_i represents the unknown time delay for waveform i and d_{ij} represents the given relative time delay between waveforms i and j. For an array of $M \times N$ waveforms, the number of such equations is $4MN - 3(M + N) + 2$, and the number of unknowns is $MN - 1$. (One waveform is used as a time reference.) Therefore, the number of equations is approximately

11

four times the number of unknowns. These equations are solved in the least-squares sense
by minimizing

$$\sum_i \sum_j \left[w_{ij} (\tau_i - \tau_j - d_{ij})^2 \right],$$

where the summations for i and j are over all the relative time delays d_{ij}'s that have been
given, and w_{ij} is the weight for d_{ij}. The solution of this least-squares problem can exploit
the simple structure of the equations and is computationally inexpensive compared to the
calculation of all the cross-correlation functions that are needed to find the relative time
delays.

The estimation of relative time delay between two waveforms was based on the position
of a peak in the cross-correlation function of the two waveforms. However, instead of
seeking the peak position blindly, a reference point was used to guide the search for the
peak position and to provide a weight for the obtained result. To reduce computation,
the cross-correlation function of neighboring waveforms was calculated over only ± 10 lags.
The search in the cross-correlation function returned a peak position that was closest to
the reference point and that position was used for the relative time delay.

The weight of the relative time delay so obtained was calculated using the distances
of the reference point to the two closest peaks on either side of the reference point. When
the two distances were about equal, meaning which peak to choose was not clear, a low
confidence was placed on the result. When one peak was much closer than the other to
the reference point, a high confidence was placed on the result. The particular weight
function used is $\log[(d_a + \epsilon)/(d_b + \epsilon)]$, where d_a is the larger and d_b is the smaller of the
two distances from the reference point to the two nearest peaks, and ϵ is a small positive
number added to avoid singularity in the calculation.

The reference value initially used to guide the peak search was zero for every pair,
meaning that in the absence of any *a priori* knowledge, the time difference of neighboring
waveforms was assumed to be zero. This is a reasonable initial guess so long as the
wavefront has already been compensated for geometric path length differences. After the
least-squares problem was solved, a new set of references was obtained using the current
solution, *i.e.*, $\tau_i - \tau_j$ was used as the reference value for finding a new set of d_{ij}. With
the newly obtained d_{ij}, the least-squares problem was solved again to yield new values for

τ_i's. This was repeated until no d_{ij} was altered, and the final τ_i's were used as the result of time-delay estimation.

B. Dynamic Receive Focusing

Dynamic focusing in reception was performed along the axis of the transmit beam. The basic idea, like that of dynamic focusing in present clinical systems, is to have the receive focus track the transmit wavefront. The complication in this study is that the transmit and receive apertures did not overlap and an angle of about 35° existed between the transmit axis and the normal of the receiving aperture. For tracking the transmit wavefront in receive focusing, the position of the transmit wavefront at each instant was estimated by fitting a spherical surface to the estimated arrival time surface, assuming that the sound speed in the scattering medium is known. A coordinate system was established on the surface of the two-dimensional receive aperture in which x-axis was along the array direction, y-axis was along the elevation direction, and z-axis was normal to the aperture surface, as diagramed in Fig. 7. The fitting algorithm used to find the center of a given spherical arrival time surface $\tau(x, y)$ is described in an appendix. For random scattering, the arrival time was estimated using the portion of echoes that arose from the focal region of the transmission and had the highest spatial coherence. The fitted parameters (X_0, Y_0, Z_0) then represented the spatial origin for that portion of echoes and corresponded to the position of the transmit focal point. To calculate the spatial origin for other portions of echoes, the angle α of the transmit axis with respect to the normal of the receiving aperture was used. As illustrated in Fig. 7, a distance $l(\Delta t)$ along the transmission axis was determined from the focal point such that the propagation time along the new path is Δt longer than that for the path that goes through the focal point. The spatial origin of the wavefront that arrives Δt later than the focal point wavefront is then given by

$$(x_0(t), y_0(t), z_0(t)) = (X_0, Y_0 + l(\Delta t) \sin \alpha, Z_0 + l(\Delta t) \cos \alpha).$$

To bring a wavefront originating from $(x_0(t), y_0(t), z_0(t))$ into focus, the waveform $s_i(t)$ received at $(x_i, y_i, 0)$ was shifted in time by the amount

$$\eta_i(t) = \frac{1}{c} \left[\sqrt{(x_0(t) - x_i)^2 + (y_0(t) - y_i)^2 + z_0^2(t)} - \sqrt{x_0^2(t) + y_0^2(t) + z_0^2(t)} \right].$$

13

This transformed the waveform $s_i(t)$ into $s_i'(t)$ given by

$$s_i'(t) = s_i[t + \eta_i(t)].$$

Since the time-shift $\eta_i(t)$ is not a constant but a function of time, the waveforms were not only time-shifted but also stretched or compressed after dynamic focusing. To avoid undesirable time quantization effects, spline interpolation was used to resample the waveform so that $\eta_i(t)$ need not be quantized to be an integral number of sampling intervals.

C. Single Transmit Image Formation

Two kinds of images were formed with the data. The first kind is similar to the so-called explososcan imaging [18] in which a single transmit beam illuminates the medium and the received data are processed to yield an image of the medium with the given illumination. The second kind mimics regular b-scan imaging in which both the transmit and receive beams are scanned simultaneously and a line in the b-scan is obtained for each scan position.

The first step common to both kinds of image formation was the estimation of a time-delay surface using the portion of wavefront that arises from the transmit focal point and has the highest spatial coherence. The signal length used for time-delay estimation is an important parameter. Since the signals arise from random scattering, the signals are themselves random. Use of a longer signal length helps overcome the effects of randomness on the estimated time delays. However, a longer signal extends the region in the scattering medium from which the wavefronts originate and the effective distortion profile of the specimen may consequently change. Also, the spatial coherence property of the wavefronts scattered from different positions may change because the transmit beam has a finite depth of field. Therefore, a compromise was used to determine the signal length for time-delay estimation. A signal length of 128 samples, corresponding to a segment length of about 5 mm, was chosen and found to be appropriate.

The time-delay surface was estimated by first removing an approximate geometric arrival time surface from the data and then applying the least-mean-square-error method to the shifted wavefront. The approximate shifts were then added to the least-mean-square-error solution to give the total time-delay surface. The reason for this two-stage process is

14

that the current implementation of the least-mean-square-error method expects a wavefront that does not contain significant curvature. Next, a spherical fit to the time-delay surface was used to find the spatial position of the focal point relative to the receiving aperture. The fitted spherical centers appeared to coincide with the expected transmit focal point positions. Then, dynamic receive focusing shifts were applied to the received wavefront using information about the spatial origin of the echoes obtained as described previously. The resulting wavefront no longer contained any spherical curvature, and was essentially flat in the absence of aberration. This intermediate wavefront, called here the dynamically shifted wavefront, plays an important role in subsequent processing.

A single transmit image, *i.e.*, an image formed from a single transmit beam, is similar to a snap-shot picture of the medium. In the processing, the dynamically shifted wavefront was windowed spatially using a Hamming window, passed through an imaging lens of fixed focal length, and subsequently propagated to the focal plane. The focal plane time history then yielded an image of the medium under the given illumination. This image can also be interpreted as the convolution of the transmit beam with the receive beam because the image is obtained by fixing the transmit beam and steering the receive beam. The propagation from the aperture plane to the focal plane was performed by the shift-and-add method using spline interpolation to implement arbitrary time-shifts of the waveforms. For the focal length of the imaging lens, the distance of the transmit focal point to the origin in the receiving aperture was used. Although the focal plane time history corresponds to a 3-D volume, which implies that a volume image of the medium can be obtained, attention in the current study was limited to the time-history along the central elevation so the result is an image of a single cross section.

D. B-Scan Image Formation

B-scan images were formed without compensation (UNC), with time-shift compensation (TSC), and with backpropagation followed by time-shift compensation (BP+TSC).

To form an uncompensated b-scan image, the waveforms in the dynamically shifted wavefront were simply added together. This represents a focusing operation by an imaging lens and the result corresponds to the time history at the focal point of the imaging lens. The Hilbert transform [19] was used to find the analytic envelope of the waveform resulting

15

from the summation. The analytic envelopes from sequential scan lines were arranged side-by-side to form a b-scan image.

To form a time-shift compensated b-scan image, a time-delay map was estimated for each dynamically shifted wavefront, and the result was used to time-shift the wavefront at each scan position individually. After such time-shifting, the waveforms in the wavefront are better aligned in time, and summation results in a signal of larger amplitude. For wavefronts obtained with the 1/2″ transmitter, time-shift compensation was also performed using the time-delays estimated from the corresponding 2″ data. The subsequent processing was the same as that for the uncompensated case.

To form an image using backpropagation followed by time-shift compensation, the dynamically shifted wavefront was first backpropagated by a fixed distance of 20 mm. The distance was fixed because of the large amount of computation needed to carry out the backpropagation and also because of the previous finding [12] that the result is relatively insensitive to the exact distance of backpropagation. In addition, trial computations confirmed that the compensation effect did not change much with the present data when the backpropagation distance was varied by a few millimeters. Since the specimen thickness ranged from 10 to 35 mm and a distance of 5 to 8 mm existed between the receiving aperture and the top surface of the specimen, backpropagation by 20 mm brought the wavefront about half-way into the specimen. The backpropagation was implemented using the angular spectrum method [20]. In the calculation, an FFT was used to calculate the temporal as well as the spatial Fourier transform. Waveforms of 776 samples were zero-padded to 1024 samples, and aperture size of 12 × 66 elements was zero-padded to 16 × 128. Since the same backpropagation function of the form $\exp\left(j2\pi z\sqrt{1/\lambda^2 - f_x^2 - f_y^2}\right)$ was needed to backpropagate the wavefront for each scan line, the backpropagation function was computed for only one scan line and then stored for use with other scan lines. Evanescent wave components corresponding to the region $f_x^2 + f_y^2 > 1/\lambda^2$ were discarded in backpropagation because the propagation distance was much larger than the wavelength λ. A time-delay map was then estimated for the backpropagated wavefront and used to time-shift the waveforms. The subsequent processing was the same as that for the uncompensated case.

The flow-chart in Fig. 8 summarizes the various paths and steps taken to obtain images from the raw data.

III. METHODS OF EVALUATION

A. Evaluation of Wavefront Coherence

Wavefront coherence was measured by the waveform similarity factor, defined for N waveforms $s_i(t)$, $i = 1 \sim N$, by

$$\text{WSF} = \sqrt{\int_{-\infty}^{+\infty} \left[\sum_{i=1}^{N} s_i(t - \tau_i)\right]^2 dt} \bigg/ \sqrt{\sum_{i=1}^{N} \int_{-\infty}^{+\infty} s_i^2(t) dt}$$

in which the τ_i's are adjusted to align all the waveforms in time and to maximize the WSF. The value of this factor is easily shown to be always between 0 and 1, with 1 corresponding to the case where all waveforms are exactly alike except for a time delay and an amplitude scaling. The value of the WSF depends on the time delays τ_i and will generally be smaller if the estimated τ_i's are incorrect. In the current study, the τ_i's were obtained using the least-mean-square-error method, as summarized in Section II-A.

B. Evaluation of Point Target Image

Point target images were obtained using the single transmit image formation described in Section II.C. The point target was illuminated with a focused transmit beam and the corresponding echoes received in the two-dimensional aperture were processed under different conditions of compensation to produce different images. These images were two-dimensional, with one of the dimensions being the array (azimuthal) direction and the other being the time (range) direction. The evaluation of such images follows the procedure we used in a previous study [15]. The amplitudes of the analytic envelope were first projected using the maximum amplitude for each array or time position, to yield one-dimensional amplitude profiles along the time or array direction. Effective widths were then found from these profiles at -10, -20, and -30 dB, from the peak. The square root of the product of the effective widths in each direction was defined as the effective diameter. The effective diameter was a function of the level from the peak, and provided a measure of the focal spot size at different levels. Another measure was the -10 dB peripheral energy ratio. This dimensionless parameter was calculated by specifying an ellipse whose center was at the position of maximum amplitude and whose axes were half of the -10 dB effective widths in each direction. The ellipse separated the image into the central

17

and the peripheral regions, and the ratio of the total energy outside the ellipse to the total energy inside the ellipse was the peripheral energy ratio.

C. Evaluation of Isoplanatic Patch Size

Using data measured as described in Section I.B, images of the test point target were obtained at each position after cross compensation using time-shifts derived from the wavefront measured with the original point target. The −10 dB effective diameter of the image was calculated. For self compensation, the compensation effect is the best, and the −10 dB effective diameter is the smallest. With increasing distance between the test and the original point target, the compensation effect deteriorates, and the effective diameter increases. When the amount of increase reached 10%, the corresponding distance between the original and the test point targets was taken to be half of the isoplanatic patch size. The reason for the factor of 2 is that the isoplanatic patch extends over both sides of the original point target.

Isoplanatic patch size was evaluated for wavefronts in the aperture as well as after backpropagation by 20 mm. In the latter case, all the wavefronts were backpropagated individually first, and a set of time shifts was estimated for the backpropagated wavefront corresponding to the original point target. These time shifts were then applied to the other backpropagated wavefronts, which were then focused and evaluated as before.

D. Evaluation of Contrast Resolution

The evaluation of contrast resolution used b-scan images of the cyst phantom obtained with no compensation, with time-shift compensation in the aperture, and with backpropagation followed by time-shift compensation. The cyst phantom had a scatterer-free cylinder that was 10 mm in diameter and was positioned perpendicular to the transmit beam. To calculate the contrast ratio, a circular area of diameter 6 mm was manually selected in central part of the cyst region. Another circular area of the same diameter and 12 mm above the first circle was correspondingly placed in the region of uniform scattering. The contrast ratio was calculated as the ratio of the average energy levels in these two circles. The area inside the cyst region was manually selected because the alignment between the phantom and the scanning stages was not controlled exactly. The diameter of the circular area was made smaller than the known diameter of the cyst-like region in order to exclude relatively large amplitudes near the edge.

IV. RESULTS

A total of 10 specimens were studied using the agar/glass-sphere phantom. However, three measurements were unusable due to misalignment of the transmit focus with the cyst phantom or too low SNR's caused by specimen attenuation. Results obtained with the remaining seven different specimens are presented here.

A. Waveform Similarity Factor and Time-Delay Estimation

Representative maps of estimated arrival time fluctuation are shown in Fig. 9. These maps show essentially the same trend of arrival time fluctuation caused by the tissue, but spatial features as well as the numerical values of arrival time fluctuations estimated using the 2″ transducer data are closer to those obtained with the point target data than those in the maps estimated using the 1/2″ and 1″ transducer data.

The waveform similarity for the point target and water path propagation was 0.997, very close to the ideal value of 1.0. The nonideality stems from the variation of the response characteristics of the elements in the linear array. The waveform similarity factor results for the seven specimens are tabulated in Table II. These results show that, at the aperture, the average waveform similarity factor of random scattering wavefronts was 0.261 for 1/2″ transmitter, 0.490 for 1″ transmitter, and 0.577 for 2″ transmitter. The point target data has a much higher average waveform similarity factor at 0.935. After backpropagating the wavefronts by 20 mm, the average waveform similarity factor increased to 0.275, 0.513, and 0.597, respectively, for random scattering with the 1/2″, 1″, and 2″ transmitter, and to 0.951 for the point target data. These results show that a point target produces a scattered wavefront with the highest spatial coherence, but a body of random scatterers illuminated with a highly focused transmit beam (such as obtained with the 2″ transmitter) can be used to produce a wavefront of sufficient spatial coherence in the absence of isolated point targets. These results also show that wavefront backpropagation removes some waveform distortion caused by propagation through the inhomogeneous medium.

The time-delay estimation results are summarized in Table III in which the rms value of the residual of fitting a spherical surface to the estimated arrival time surface is used to describe the fluctuation. Using the results obtained with the point target data as the standard, the rms arrival time fluctuation estimated using random scattering was

underestimated by 8.6, 5.7, and 2.9 ns for the 1/2″, 1″, and 2″ diameter transducers, respectively. The corresponding average underestimation was reduced to 6.6, 3.1, and 0.4 ns, respectively, after backpropagation by 20 mm. These results, combined with the above waveform similarity results, show that a tight transmit focus is needed to create a highly coherent scattered wavefront for the accurate measurement of time shifts, and that backpropagation increases the wavefront coherence and improves the accuracy of arrival time estimation.

B. Point Target Images

Point target images are shown in Fig. 10 to illustrate the compensation effects through a tissue path. The uncompensated image has a large spread of energy around the focal point. The focus is significantly improved with time-shift compensation and the sidelobe energy is greatly reduced. With backpropagation followed by time-shift compensation, the sidelobe energy is further reduced but the mainlobe remains relatively unchanged. For comparison, the corresponding point target image obtained through a water path is also shown. The image obtained with backpropagation followed by time-shift compensation approachs the image obtained through a water path.

Statistics are presented in Table IV for the effective diameters of the focus at different levels from the peak as well as for the −10 dB peripheral energy ratio. The results show that time-shift compensation significantly improves the −10 and −20 dB effective diameter, but the −30 dB effective diameter after time-shift compensation (16.22 mm) is still much greater than the corresponding water-path value (7.79 mm). With backpropagation followed by time-shift compensation, the effective diameter at −30 dB is reduced to 8.20 mm, which is very close to the water-path value.

C. Isoplanatic Patch Size

A set of representative point target images used to determine the isoplanatic patch size is shown in Fig. 11. These images were obtained for different point target positions after time-shift compensation using the same time delay map estimated for the first point target position. The deterioration of the compensation effects as the distance between the test point target and the original (first) point target increases is clearly visible. For comparison, the point target image obtained without any compensation is also shown in the figure.

The isoplanatic patch size results are summarized in Table V. For time-shift compensation in the aperture, the average isoplanatic patch size was 16.7 mm in the azimuthal direction and 39.0 mm in the range direction. For time-shift compensation after backpropagation by 20 mm, the average isoplanatic patch size increased to 19.0 mm in the azimuthal direction and 41.4 mm in the range direction. This indicates that backpropagation has effectively extended the isoplanatic patch size. In only one case (npe21) did the isoplanatic patch size in the range direction decrease (from 16.1 mm to 7.4 mm) with backpropagation. Further examination of that case reveals that the self compensated point target image has a −10 dB focal diameter of 2.49 mm after backpropagation, much smaller than the corresponding value (3.29 mm) obtained with time-shift compensation alone. Therefore, the threshold for determining the isoplanatic patch size, which is taken as 1.1 times the −10 dB focal diameter with self-compensation, was correspondingly lowered. If the same threshold value were used to determine the isoplanatic patch size with or without backpropagation, the isoplanatic patch size would be 24.2 mm instead of 7.4 mm in the range direction after backpropagation.

D. Images and Contrast Ratio

A set of single transmit images are shown in Fig. 12. These images were obtained with the phantom illuminated by the 1/2″, 1″, and 2″ diameter transmitters, respectively, and the reception is through a water path. The data used to form these images were from the first scan position, so the center of illumination is about 10 mm away from the cyst-like area. The reduction of beam size with increasing transmitter diameter is clearly demonstrated. In the case of the 1/2″ transmitter, the illuminated region was so large that part of the cyst-like area appears in the lower right corner of the image.

Another set of single transmit images are shown in Fig. 13. These images are obtained with the 2″ transmitter through a tissue reception path (npe21) under different conditions of beamforming (UNC, TSC, and BP+TSC), and through a water reception path. These images show that the receiver beam was severely distorted by the specimen, was significantly improved with time-shift compensation, and was further improved with backpropagation followed by time-shift compensation. However, the results after compensation still show more energy spread compared to water path results.

Representative b-scan images that correspond to the single transmit images shown in Fig. 13 are shown in Fig. 14. The contrast ratio in this example improved from 24.0 dB to 26.2 dB using time-shift compensation, and to 27.5 dB using backpropagation followed by time-shift compensation. The water path contrast ratio was much higher at 38.0 dB. Statistics of the contrast ratio results for the seven tissue specimens are summarized in Table VI. The average improvement in contrast ratio is the smallest (2.0 dB) with time-shift compensation on the 1/2″ transducer data, and the largest (3.5 dB) with backpropagation followed by time-shift compensation on the 2″ transducer data.

VI. DISCUSSION

The reason for using a configuration in which the transmit beam is unperturbed is the need to control the transmit beam size for the purpose of this investigation. In *in vivo* b-scan imaging, however, the transmit beam as well as the receive beam will be distorted by the inhomogeneous medium, so any compensation of the transmit beam must be applied iteratively based on current estimation of distortion. To be more specific, initially, a transmit focus could be formed using geometric delays, and distortion information estimated using the scattered wavefront. Next, the distortion information can be used to improve the transmit focus. This would produce a tighter transmit focus for more accurate estimation of distortion. Such a process could then be repeated until no improvement is obtained or the estimated values of distortion do not change substantially. To carry out this kind of iteration, however, requires a two-dimensional array with electronics that permits modification of time delay. If the distortion is modeled as a time-shifting screen placed some distance away from the aperture, then the transmit waveforms should ideally be individually adjustable to produce a predistorted wavefront such that subsequent propagation in the inhomogeneous medium will undo the distortion and a diffraction-limited focus will result. The predistorted wavefront would be obtained by backpropagating a time-shifted (but otherwise ideally focused) wavefront from the position of the hypothetical phase screen to the array. When both transmit and receive beams are compensated for distortion, the contrast ratio improvement will be about twice as much as obtained with only receive beam compensation, because the effective beam pattern in b-scan imaging is the product of the transmit and receive beams. This implies that the contrast ratio improvements presented in Table VI can potentially be doubled in practice.

The underestimation of arrival time fluctuation when the transmit beam is broad (as shown in Table III for the 1/2″ transducer) is noteworthy. This phenomenon has been qualitatively observed before [3]. With a broad beam, echoes return from a large volume of random scatterers. Since the distortion effect for different scatterer positions is different (with the difference larger for scatterers farther apart), the overall distortion effect for the rf-signal received by a particular element is in a sense an average of the different distortion effects. This averaging results in the significant underestimation of arrival time fluctuation for a broad transmit beam.

23

A gradual variation of the perceived arrival time fluctuation with the point target position was observed in processing the measured wavefronts to derive the isoplanatic patch size. The variation consisted of changes in spatial feature details and magnitudes of the fluctuation. Because the relative position of the receiving array and the specimen remained fixed in our measurements for the isoplanatic patch size, the overall spatial features of the arrival time fluctuation remained unchanged.

The size of the isoplanatic patch found in this study implies that a single distortion profile can be used over a reasonable region of about 20×40 mm^2. However, these numerical values depend on many factors including the severity of distortion, the distance from the scattering region to the aperture, and the threshold condition used to define the isoplanatic patch size. Examination of Tables V reveals that the isoplanatic patch sizes for datasets npe21, npe24, and npe27 are relatively small. Correspondingly, the waveform similarity factors for these 3 sets of data are low (Table II) and the waveform arrival time fluctuations are high (Table III). In practice, due to the relatively slow speed of sound propagation in tissue, only a limited number of transmissions can be used for real-time image formation. Therefore, not many transmissions can be devoted to the estimation of the distortion profile. To circumvent this difficulty, a point of interest may be selected, and the distortion profile around that point may be estimated and used to compensate for distortion in the associated isoplanatic patch. This way the frame rate is little influenced and the computational requirements are also reduced.

The expansion of the isoplanatic patch size after backpropagation merits further comment. If the aberration effect is indeed caused by a time-shifting screen placed at some distance away from the measurement aperture, then, after backpropagation by the right distance, the time delays required to align the waveforms will be the same no matter where the point target is positioned. In this case, the same set of parameters (backpropagation distance and arrival time fluctuations) can be used to correct for any imaging positions, and the isoplanatic patch size will be very large. Therefore, the increase in the isoplanatic patch size after backpropagation indicates that a time-shifting screen placed a certain distance away is a better model for the aberration medium. This observation also indicates that the isoplanatic patch size is not merely a function of the aberration medium but is also a function of the compensation algorithm.

24

A comparison of the images in Fig. 12 shows that the beam pattern of the 2″ transducer is only modestly narrower than that of the 1″ transducer. A possible explanation is that the 2″-diameter transducer has a focusing lens that is over 1 cm thicker at the edge than at the center. The attenuation through the lens material presumably added a spatial apodization to the transducer and effectively broadened the transmit beam. The small beamwidth difference between the 1″ and 2″ transducers is also reflected in the very small difference in contrast ratios (Table VI) achieved with these transducers.

The results presented in Table VI show that greater improvement is achieved with a larger transmitting aperture. An intuitive explanation for this is that the scattered wavefront produced by the larger aperture is more coherent and can be aligned with greater accuracy. Similarly, wave backpropagation removed some of the amplitude fluctuation and waveform distortion developed during propagation through the specimen, and this helped to improve the contrast ratio further.

The compensated images still, however, have a significantly lower contrast ratio than that of images obtained through a water path. For example, the average contrast ratio obtained with the 2″ transmitter after backpropagation and time-shift compensation was 31.3 dB, whereas the water path image in Fig. 14, also obtained using the 2″ transmitter, had a contrast ratio of 38 dB. One reason for the incomplete compensation is that the backpropagation model is still an approximation of the inhomogeneous medium and does not completely represent all the distortion effects. Another reason is the reduced signal-to-noise ratio (SNR) of the received signals as a result of attenuation in the specimen. The average tissue-path SNR obtained with the 2″ transducer was 19 dB as measured by digitizing the random signals from the phantom with the pulser turned on, and by digitizing the background noise with the pulser turned off. In a water path, however, the SNR obtained with the 2″ transducer (npe284) was 26.6 dB. Since random noise is incoherent and cannot be focused, its presence increases the baseline signal energy throughout the image, thereby reducing the image contrast.

VII. CONCLUSION

Wavefront aberration estimation and correction have been investigated using random scattering measured in a specially designed pulse-echo configuration in which the transmit beam was unperturbed by the aberration medium.

From the investigation, the following conclusions can be made about the accuracy of aberration estimation, the isoplanatic patch size, and the effectiveness of correction.

1) A tightly focused transmit beam, such as that produced by the 2″ f/1.5 transducer in this study, is needed to produce a sufficiently coherent scattering wavefront so that time delays can be accurately estimated.

2) Accommodation of waveform shape distortion in time-delay estimation, such as in the modified least-mean-square-error method that incorporates a global smoothness requirement as described in this paper, is needed to estimate the time-delay surface from a random scattering wavefront that has propagated through distributed inhomogeneities.

3) The isoplanatic patch size usually decreases with increasing severity of distortion, as shown in this study for abdominal wall specimens. The isoplanatic patch size is also influenced by compensation technique, as seen in the increased isoplanatic patch size for backpropagation followed by time-shift compensation.

4) Incorporation of waveform shape compensation, such as by using backpropagation prior to time-shift compensation as in this study, improves the contrast ratio over that obtained by time-shift compensation alone.

In the absence of *a priori* knowledge about the propagation path, a tight transmit focus can only be achieved by modifying iteratively the excitation signals based on previous estimation of the aberration. Ideally, a two-dimensional array with programmable transmit waveform capability is needed for producing such a tight focus.

26

ACKNOWLEDGEMENTS

REFERENCES

[1] G. Kossoff, D. E. Robinson, and W. J. Garrett, "Ultrasonic Two-Dimensional Visualization Techniques", *IEEE Trans. Sonics Ultras.*, Vol. 12, No. 2, 31–37, 1965.

[2] F. S. Foster and J. W. Hunt, "The Focusing of Ultrasound Beams through Human Tissue", in *Acoustical Imaging*, Vol. 8, 709–718, ed. A. F. Metherell, New York: Plenum, 1980.

[3] S. W. Flax and M. O'Donnell "Phase-Aberration Correction Using Signals from Point Reflectors and Diffuse Scatterers: Basic Principles", *IEEE Trans. Ultras., Ferroelec., and Freq. Contr.*, Vol. 35, No. 6, 758–767, 1988.

[4] M. Moshfeghi and R. C. Waag, "*In-Vivo* and *In-Vitro* Ultrasound Beam Distortion Measurements of a Large Aperture and a Conventional Aperture Focused Transducer", *Ultras. in Med. and Bio.*, Vol. 14, No. 5, 415–428, 1988.

[5] R. C. Waag, D. Dalecki, and W. A. Smith, "Estimates of Wave Front Distortion from Measurements of Scattering by Model Random Media and Calf Liver", *J. Acoust. Soc. Am.*, Vol. 85, No. 1, 406–415, 1989.

[6] L. Nock, G. E. Trahey, and S. W. Smith, "Phase Aberration Correction in Medical Ultrasound Using Speckle Brightness as a Quality Factor", *J. Acoust. Soc. Am.*, Vol. 85, No. 5, 1819–1833, 1989.

[7] Y. Sumino and R. C. Waag, "Measurements of Ultrasonic Pulse Arrival Time Differences Produced by Abdominal Wall Specimens", *J. Acoust. Soc. Am.*, Vol. 90, No. 6, 2924–2930, 1991.

[8] L. M. Hinkelman, D.-L. Liu, L. A. Metlay, and R. C. Waag, "Measurements of Ultrasonic Pulse Arrival Time and Energy Level Variations Produced by Propagation through Abdominal Wall," *J. Acoust. Soc. Am.*, Vol. 95, No. 1, 530–541, 1994.

[9] L. M. Hinkelman, D.-L. Liu, R. C. Waag, Q. Zhu, and B. D. Steinberg, "Measurements and Correction of Ultrasonic Pulse Distortion Produced by Human Breast", *J. Acoust. Soc. Am.*, Vol. 97, No. 3, 1958–1969, 1995.

[10] D.-L. Liu and R. C. Waag, "Time-Shift Compensation of Ultrasonic Pulse Focus Degradation using Least Mean Square Error Estimates of Time Delay", *J. Acoust. Soc. Am.*, Vol. 95, No. 1, 542–555, 1994.

[11] M. Fink, "Time Reversal of Ultrasonic Fields — Part I: Basic Principles", *IEEE Trans. Ultras., Ferroelec., and Freq. Contr.*, Vol. 39, No. 5, 555–566, 1992.

[12] D.-L. Liu and R. C. Waag, "Correction of Ultrasonic Wavefront Distortion using Backpropagation and a Reference Waveform Method for Time-Shift Compensation", *J. Acoust. Soc. Am.*, Vol. 96, No. 2, 649–659, 1994.

[13] R. Mallart and M. Fink, "The van Cittert-Zernike Theorem in Pulse Echo Measurements", *J. Acoust. Soc. Am.*, Vol. 90, No. 5, 2718–2727, 1990.

[14] D.-L. Liu and R. C. Waag, "About the Application of the van Cittert-Zernike Theorem in Ultrasonic Imaging", *IEEE Trans. Ultras., Ferroelec., and Freq. Contr.*, Vol. 42, No. 4, 590–601, 1995.

[15] D.-L. Liu and R. C. Waag, "A Comparison of Ultrasonic Wavefront Distortion and Compensation in One-Dimensional and Two-Dimensional Apertures", *IEEE Trans. Ultras., Ferroelec., and Freq. Contr.*, Vol. 42, No. 4, 726–733, 1995.

[16] R. Mallart and M. Fink, "Adaptive Focusing in Scattering Media through Sound-Speed Inhomogeneities: the van Cittert-Zernike Approach and Focusing Criterion", *J. Acoust. Soc. Am.*, Vol. 96, No. 6, 3721–3732, 1994.

[17] P.-C. Li and M. O'Donnell, "Phase Aberration Correction on Two-dimensional Conformal Arrays", *IEEE Trans. Ultras., Ferroelec., and Freq. Contr.*, Vol. 42, No. 1, 73–82, 1995.

[18] O. T. von Ramm, S. W. Smith, and H. G. Pavy, Jr., "High-Speed Ultrasound Volumetric Imaging System — Part II: Parallel Processing and Image Display", *IEEE Trans. Ultras., Ferroelec., and Freq. Contr.*, Vol. 38, No. 2, 109–115, 1991.

[19] A. V. Oppenheim and R. W. Shafer, *Discrete-Time Signal Processing*, Prentice Hall, Englewood Cliffs, NJ (1989), ch. 10.

[20] J. W. Goodman, *Introduction to Fourier Optics*, McGraw-Hill Publishing Co., NY (1968), ch. 3.

APPENDIX

The problem is to find a spherical surface that best fits a given arrival time surface $\tau(x_i, y_i)$ with an unknown offset τ_0,

$$\tau(x_i, y_i) \approx \tau_0 + \frac{1}{c}\sqrt{(x_i - x_0)^2 + (y_i - y_0)^2 + z_0^2},$$

where the sound speed c is assumed known, and (x_0, y_0, z_0) is the unknown center of the sphere. Although direct minimization of the sum of squared errors in the above approximation leads to a nonlinear least-squares problem, the problem can be linearized by rewriting the above equation as

$$c^2[\tau(x_i, y_i) - \tau_0]^2 \approx (x_i - x_0)^2 + (y_i - y_0)^2 + z_0^2.$$

Rearranging this equation yields

$$\theta_0 + x_i\theta_1 + y_i\theta_2 + \tau_i\theta_3 \approx b_i,$$

where

$$\tau_i = \tau(x_i, y_i),$$
$$\theta_0 = x_0^2 + y_0^2 + z_0^2 - (c\tau_0)^2,$$
$$\theta_1 = -2x_0,$$
$$\theta_2 = -2y_0,$$
$$\theta_3 = 2c^2\tau_0,$$

and

$$b_i = (c\tau_i)^2 - x_i^2 - y_i^2.$$

Therefore, the problem can be solved by minimizing

$$\sum_i [\theta_0 + x_i\theta_1 + y_i\theta_2 + \tau_i\theta_3 - b_i]^2$$

with respect to $\theta_0, \theta_1, \theta_2, \theta_3$. This is a linear problem, and x_0, y_0, z_0, and τ_0 can readily be found from the θ_i's.

Table I. Data Acquisition Parameters

Parameter	Value
Transmit Transducer diameters	0.5″, 1″, and 2″
Transmit Transducer focal length	3″
2-D aperture in array direction	66×0.72 mm^2
2-D aperture in elevation direction	12×1.0 mm^2
Number of scan lines	20
Scan line increment	1.0 mm
Signal center frequency	3.63 MHz
Signal bandwidth (-6 dB)	1.42 MHz
Sampling rate	20 MHz
Sampling precision	12 bits

Table II. Waveform Similarity Factor Statistics. The column under Pt are data from a point target, while the columns under 1/2″, 1″, and 2″ are data from random scattering produced with transducers of the corresponding diameters.

Dataset	In Aperture				After Backpropagation			
	Pt	1/2″	1″	2″	Pt	1/2″	1″	2″
npe14	0.977	0.293	0.575	0.715	0.964	0.298	0.579	0.720
npe15	0.956	0.270	0.550	0.674	0.957	0.277	0.560	0.685
npe17	0.979	0.288	0.571	0.733	0.978	0.294	0.575	0.735
npe21	0.863	0.224	0.372	0.389	0.930	0.251	0.442	0.439
npe22	0.935	0.263	0.497	0.544	0.957	0.279	0.535	0.575
npe24	0.893	0.248	0.437	0.474	0.912	0.263	0.449	0.490
npe27	0.941	0.245	0.429	0.511	0.958	0.263	0.449	0.535
avg	0.935	0.261	0.490	0.577	0.951	0.275	0.513	0.597
sd	0.040	0.023	0.073	0.122	0.021	0.016	0.059	0.109

Table III. Arrival Time Fluctuation Statistics. The abbreviations are the same as in Table II while the units are nanoseconds.

Dataset	In Aperture				After Backpropagation			
	Pt	1/2″	1″	2″	Pt	1/2″	1″	2″
npe14	29.9	28.6	28.7	28.9	30.6	27.5	28.8	29.3
npe15	44.3	34.9	40.3	41.1	42.4	35.0	41.5	42.0
npe17	34.8	30.4	31.7	33.1	35.0	29.4	30.8	32.6
npe21	60.9	48.4	52.7	58.0	61.8	55.4	60.6	65.0
npe22	41.6	30.0	31.9	36.0	41.6	33.4	35.6	39.0
npe24	62.9	52.3	55.5	59.4	61.6	51.7	56.5	60.2
npe27	40.2	30.6	33.2	39.5	42.3	36.5	40.0	44.1
avg	45.2	36.6	39.5	42.3	45.0	38.4	42.0	44.6
sd	11.5	8.9	9.9	11.0	11.3	10.0	11.3	12.4

Table IV. Point-Target Image Statistics. Listed are the average (avg) and standard deviation (sd) of the -10, -20, and -30 dB effective diameter in mm, and the -10 dB peripheral energy ratio (PER) for 7 abdominal specimens under three conditions: UNC=uncompensated, TSC=time-shift compensated, BP+TSC=backpropagation by 20 mm followed by time-shift compensation. The corresponding values for a water path are also listed.

		UNC	TSC	BP+TSC	Water
-10 dB Dia.	avg	4.38	2.40	2.25	2.25
	sd	3.13	0.08	0.12	
-20 dB Dia.	avg	10.59	4.87	3.70	3.38
	sd	4.43	2.62	0.71	
-30 dB Dia.	avg	18.46	16.22	8.20	7.79
	sd	1.06	2.42	2.68	
-10 dB PER	avg	0.727	0.297	0.203	0.188
	sd	0.537	0.123	0.040	

Table V. Isoplanatic Patch Size Statistics. The units are mm.

Dataset	In Aperture		After Backpropagation	
	Azimuth	Range	Azimuth	Range
npe14	27.4	56.0	27.4	56.0
npe15	20.9	51.5	23.4	56.0
npe17	27.4	56.0	27.4	56.0
npe21	1.6	16.1	4.4	7.4
npe22	13.0	54.1	15.2	56.0
npe24	16.4	15.3	22.2	19.6
npe27	9.9	24.2	12.9	39.1
avg	16.7	39.0	19.0	41.4
sd	8.7	18.0	7.9	18.9

Table VI. Contrast Ratio Statistics. The units are dB. Abbreviations: UNC = Uncompensated data, TSC = time-shift compensated data, BP+TSC = backpropagation followed by time-shift compensation, TSC/2″ delay = time-shift compensation with delays estimated using the corresponding 2″ transducer data.

Dataset	1/2″				1″			2″		
	UNC	TSC	BP+TSC	TSC/2″ delay	UNC	TSC	BP+TSC	UNC	TSC	BP+TSC
npe14	24.0	25.0	26.1	24.4	29.8	30.6	30.9	30.7	32.9	33.0
npe15	21.9	22.2	22.7	23.7	28.1	29.7	29.6	29.1	30.9	30.5
npe17	21.9	23.8	24.1	24.9	31.0	31.7	32.1	30.5	33.6	34.0
npe21	13.7	18.2	18.0	18.7	24.2	27.6	28.5	24.0	26.2	27.5
npe22	17.9	19.7	20.5	20.6	28.1	30.8	32.4	28.0	30.6	31.9
npe24	16.5	19.7	19.5	20.5	26.8	30.3	31.2	25.0	29.4	31.1
npe27	20.9	21.6	21.5	20.9	23.6	26.1	26.1	27.5	30.3	31.0
avg	19.5	21.5	21.8	22.0	27.4	29.5	30.1	27.8	30.6	31.3
sd	3.4	2.2	2.6	2.2	2.5	1.8	2.1	2.4	2.2	1.9
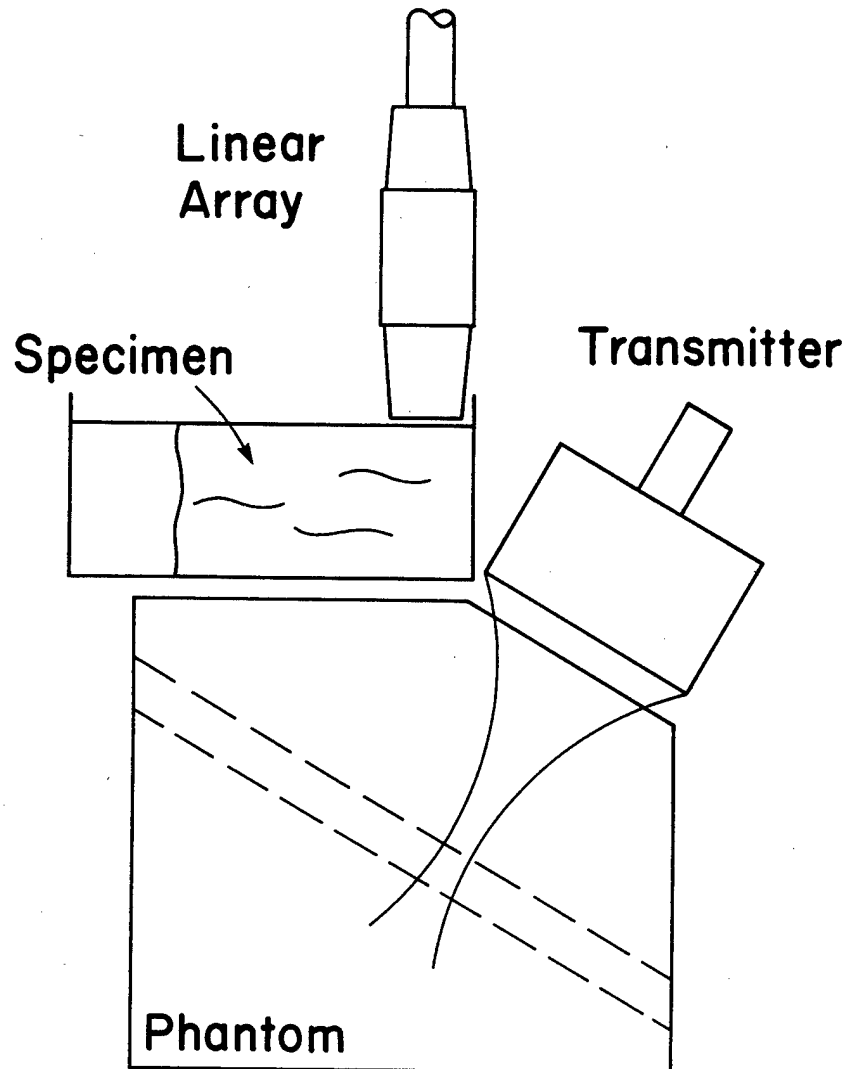
Fig. 1. Measurement Configuration. A single-element transducer produces an unperturbed beam that illuminates the scattering phantom. The phantom contains a scatterer-free cylinder that emulates a blood vessel or a cyst-like region. Echoes are received by a modified linear array after propagation through a specimen of human abdominal wall. The transmit focal point is maintained in the same spatial position by a special transmitter mount (not shown) when the transmitter is changed.
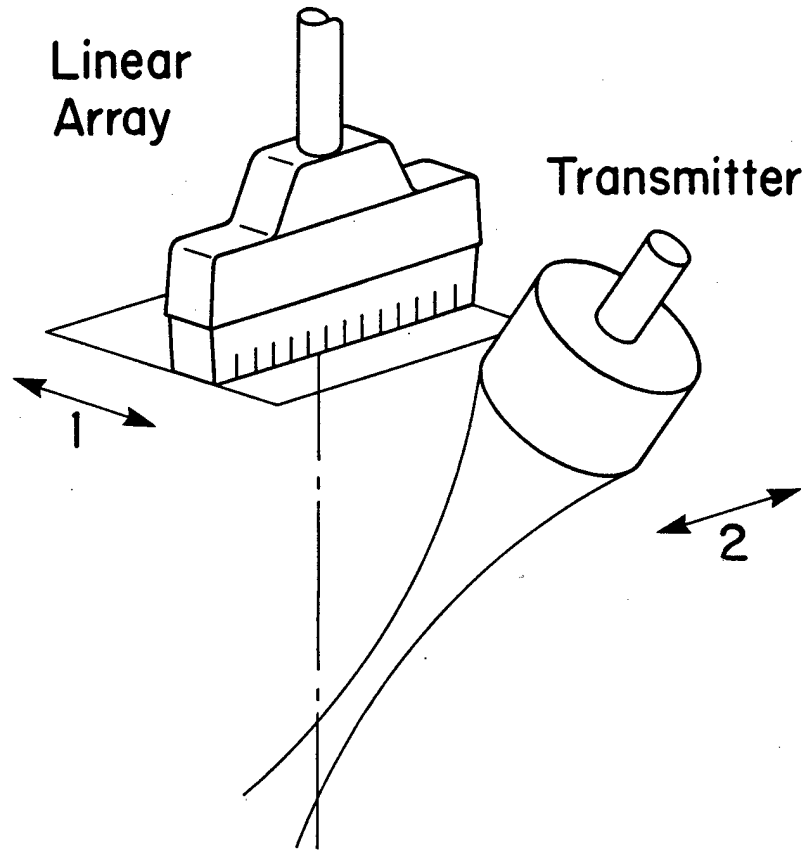
Fig. 2. Scan Movements. The linear array is scanned in the elevation direction by scan movement 1 to synthesize a 2-D receiving aperture. The transmitter and the linear array (and, thus, the synthesized 2-D aperture) are scanned together by scan movement 2 to form b-scan lines.
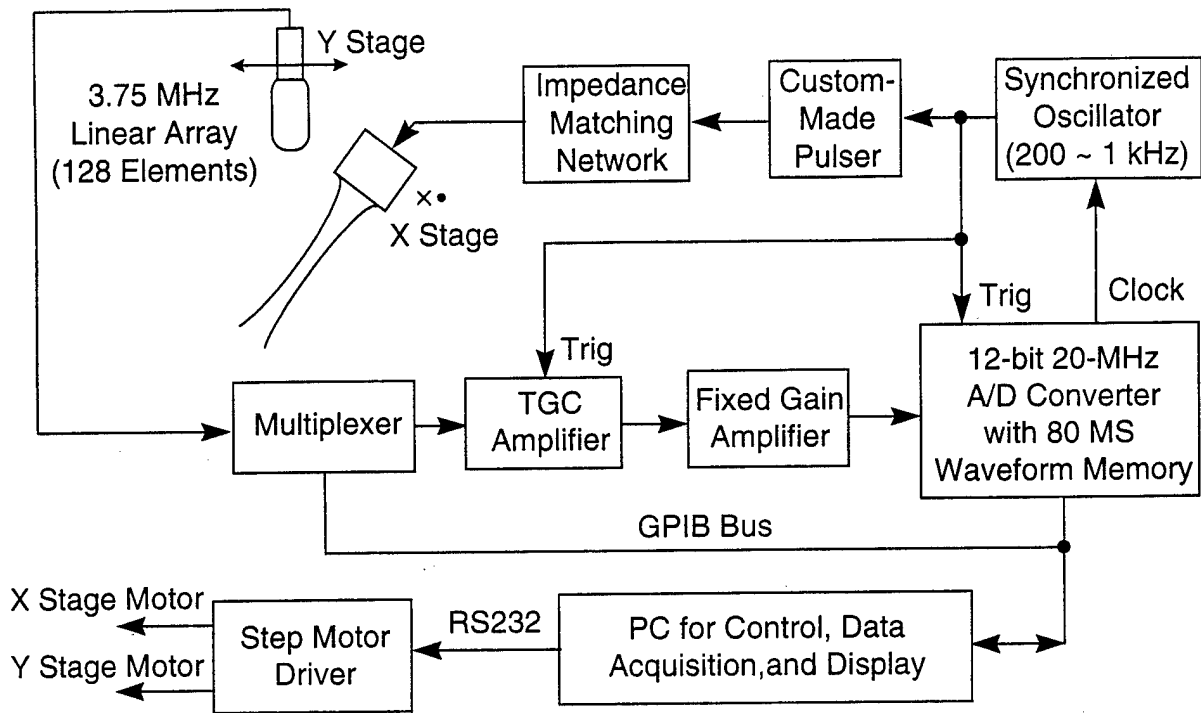
Fig. 3. Diagram of Data Acquisition System.
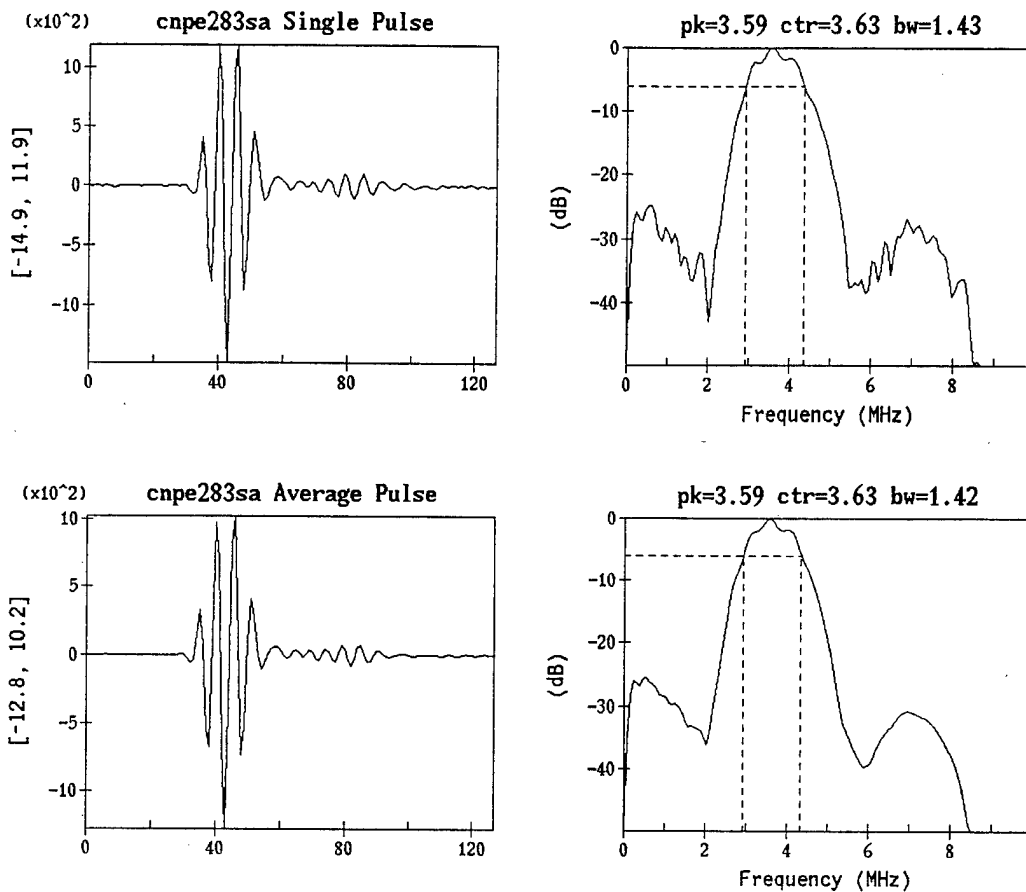
Fig. 4. Pulse-Echo Waveforms and Corresponding Spectra obtained through a Water Path from a Point Target. The top row shows a waveform (left) and the corresponding spectrum (right) from the central array element at the central elevation. The bottom row shows the average pulse and its spectrum. The average pulse was obtained by adding all the pulses in the receiving aperture after the pulses have been aligned in time. In the waveform plots, the horizontal axis is sample number and the vertical axis is amplitude on a linear scale. The transmitter was a 2″ transducer, and the point target was the rounded tip of a 1/8″-diameter stainless steel rod positioned so that the tip echo had maximum amplitude. Abbreviations: pk = peak frequency, ctr = center frequency of −6 dB passband, bw = −6 dB bandwidth.

Tissue-Path Wavefronts (Raw Data)

0.5 inch [40.0 (dB)]

1 inch [40.0 (dB)]

2 inch [40.0 (dB)]

Point Target [40.0 (dB)]
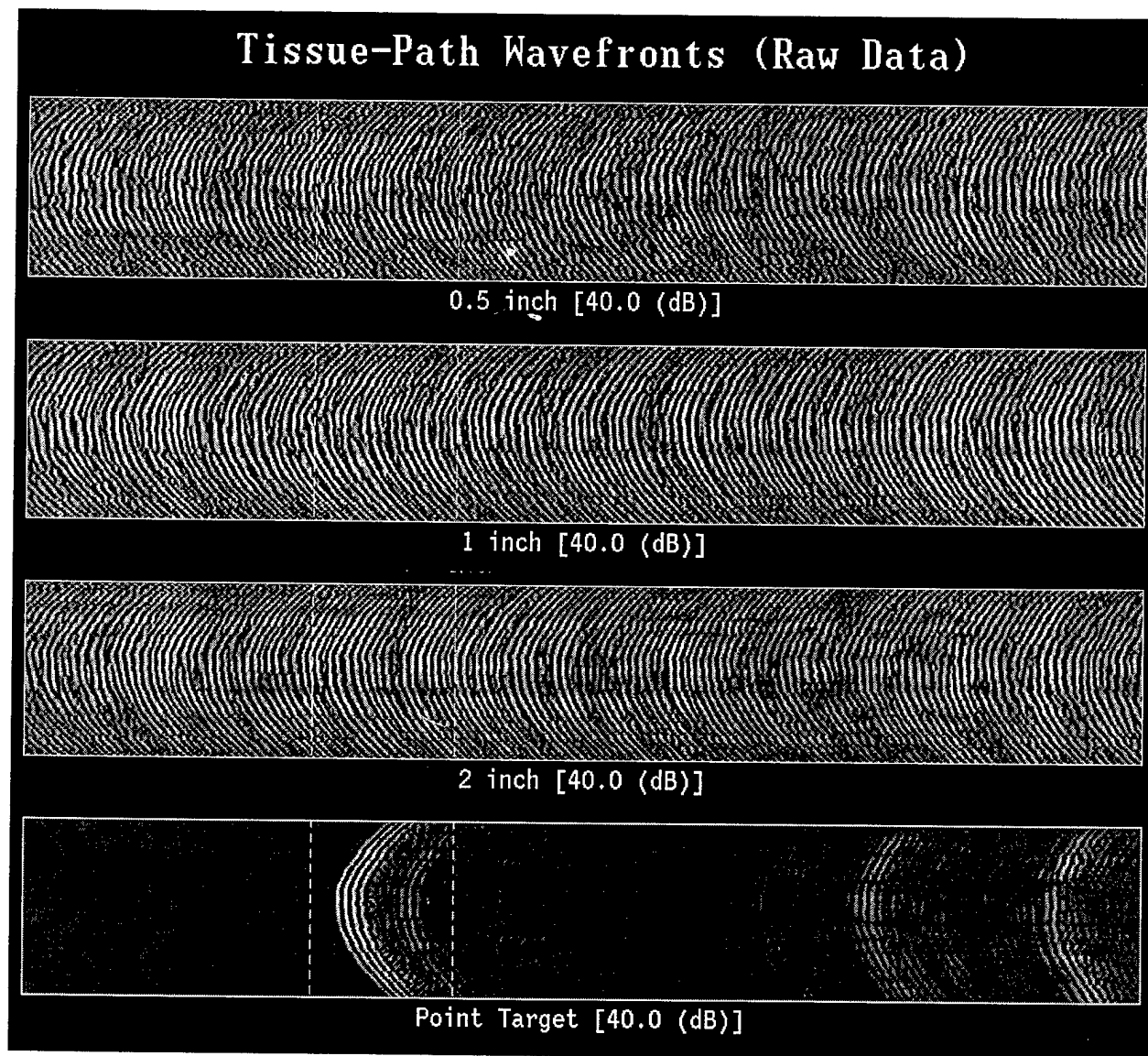
Fig. 5. Wavefronts Measured through a Tissue Path. The first three rows show wavefronts of scattering from the scattering phantom illuminated with the 1/2″, 1″, and 2″ transducer, respectively, while the last row shows the wavefront from the point target illuminated by the 2″ transducer. The horizontal axis is time and contains 776 samples obtained at a 20 MHz sampling rate. The vertical axis is the array direction and spans 66 elements with a pitch of 0.72 mm. The rf signal amplitudes are displayed using a bipolar logarithmic gray scale with 40 dB dynamic range for each polarity. The dashed lines indicate the segment of signals used for time-delay estimation after geometric correction.
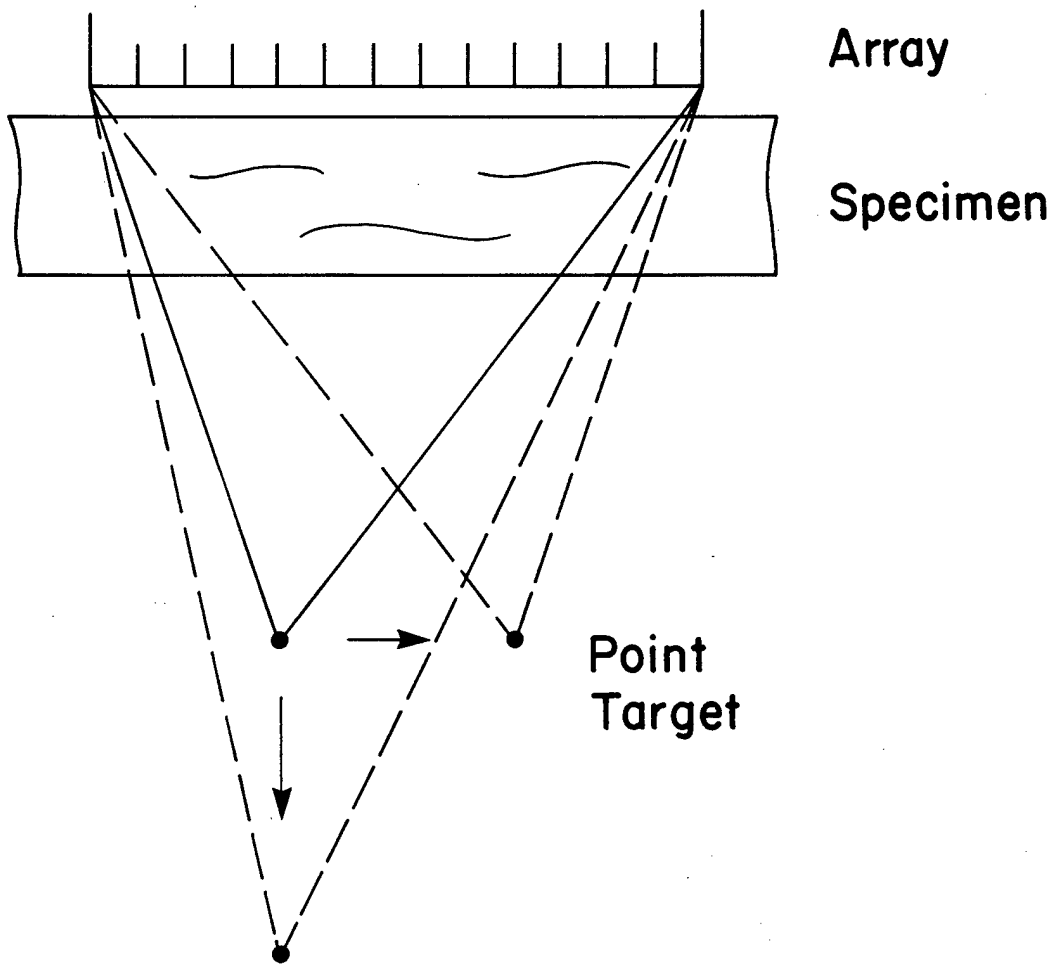
Fig. 6. Measurements for the Evaluation of Isoplanatic Patch Size. The scattered wavefront from a point target was measured for an initial (original) position (indicated by solid lines). The point target was then moved in the range or azimuthal directions to other (test) positions (indicated by dashed lines) and the scattered wavefronts were measured again.
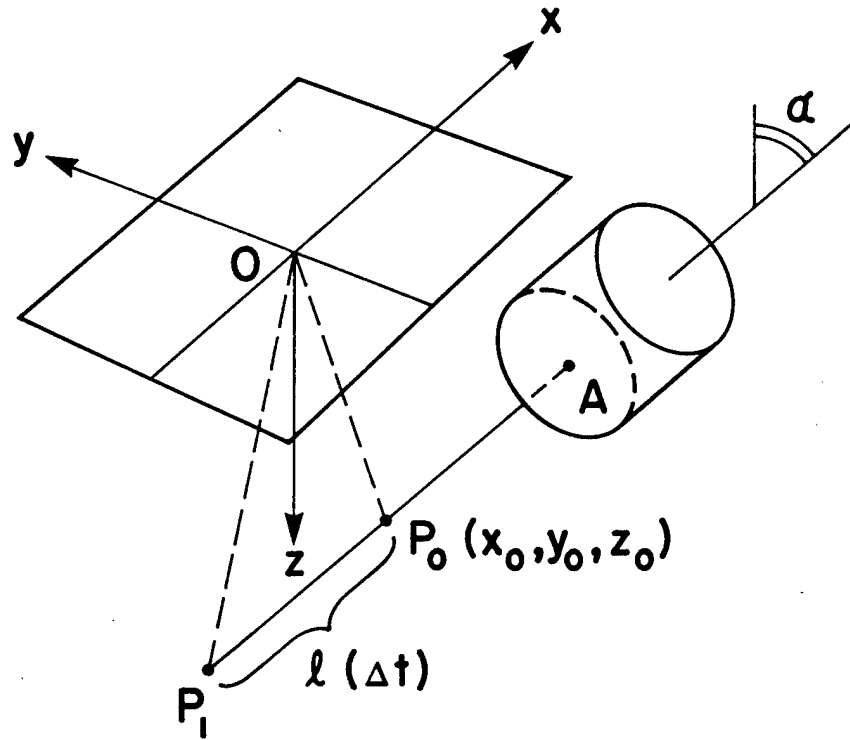
$$T(AP_1O) - T(AP_0O) = \Delta t$$
$$P_0 = \text{Transmit Focal Point}$$

Fig. 7. Estimation of the Transmit Wavefront Position along the Transmit Axis at Each Instant. The position of the transmit focal point $P_0(x_0, y_0, z_0)$ was found by fitting a spherical surface to the arrival time surface. For echoes arriving Δt later than the echoes from the focal point, the spatial origin is $\ell(\Delta t)$ away from the focal point, where $\ell(\Delta t)$ satisfies the requirement that the propagation time along the path AP_1O is Δt longer than along the path AP_0O. The angle α between the transmit axis and the z-axis was assumed known ($35°$ for the measurements reported here).

```
                    ┌───────────┐
                    │ Raw Data  │
                    └───────────┘
                          │
                          ▼
        ┌─────────────────────────────────────┐
        │   Approximate Geometric Correction  │
        └─────────────────────────────────────┘
                          │
                          ▼
              ┌───────────────────────┐
              │  Time-Delay Estimation │
              └───────────────────────┘
                          │
                          ▼
            ┌───────────────────────────┐
            │  Exact Geometric Correction │
            └───────────────────────────┘
                          │
                          ▼
          ┌─────────────────────────────┐
          │  Dynamic Receive Focussing  │
          └─────────────────────────────┘
```
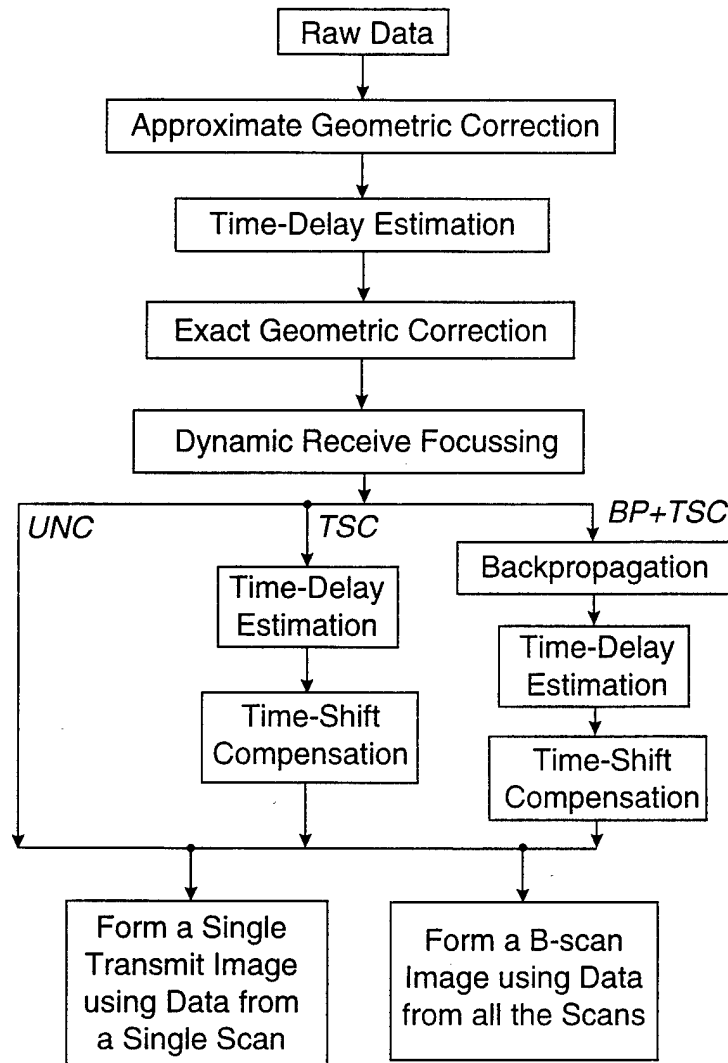
Fig. 8. Flow of Data Processing and Image Formation. Raw data were first corrected approximately for geometric path length difference using *a priori* knowledge about the position of transmit focal point. An arrival time surface was then estimated using the least-mean-square-error method with echoes arising from the focal region, and a spherical surface was fit to the arrival time surface to determine the focal point position. Next, exact geometric correction and dynamic focusing were performed. A single transmit image and a b-scan image were then formed under three different conditions: without compensation (UNC), with time-shift compensation in the aperture (TSC), and with backpropagation followed by time-shift compensation (BP+TSC). The single transmit image used aperture data from a single transmit or scan line position, while the b-scan image used data from different transmit or scan positions.
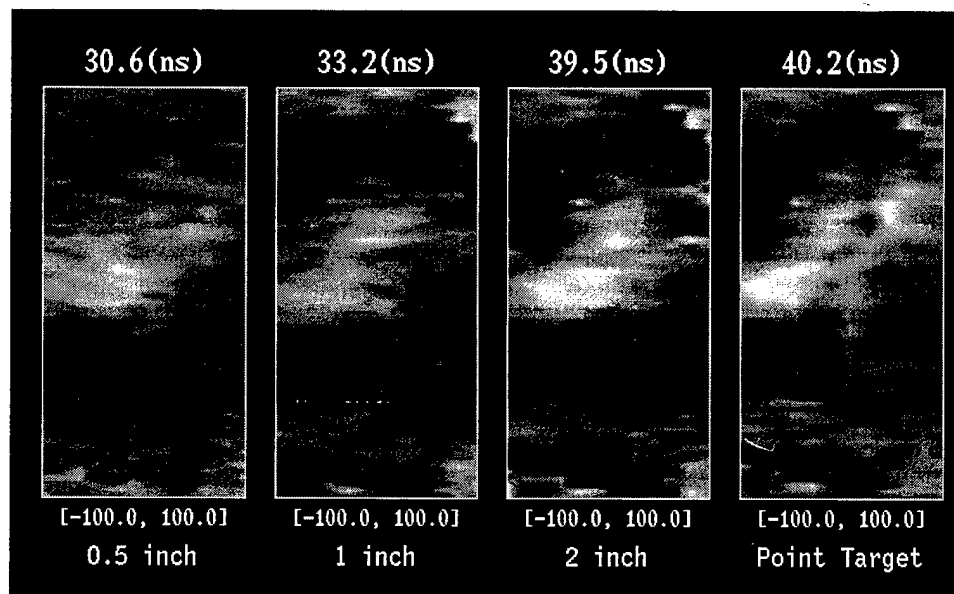
Fig. 9. Tissue-Path Arrival Time Maps Estimated Using a Point Target and Using Random Scattering Produced by 1/2″, 1″, and 2″ Transducers. The vertical coordinate is the array direction and spans 66×0.72 mm. The horizontal axis is the elevation direction and spans 12×1.00 mm. The gray scale is linear with white corresponding to +100 ns and black corresponding to −100 ns. The standard deviation (indicated at the top of each panel) and the spatial features of the arrival time map estimated from random scattering approach those estimated using a point target as the transmit focal spot size gets smaller. The dataset was npe27.
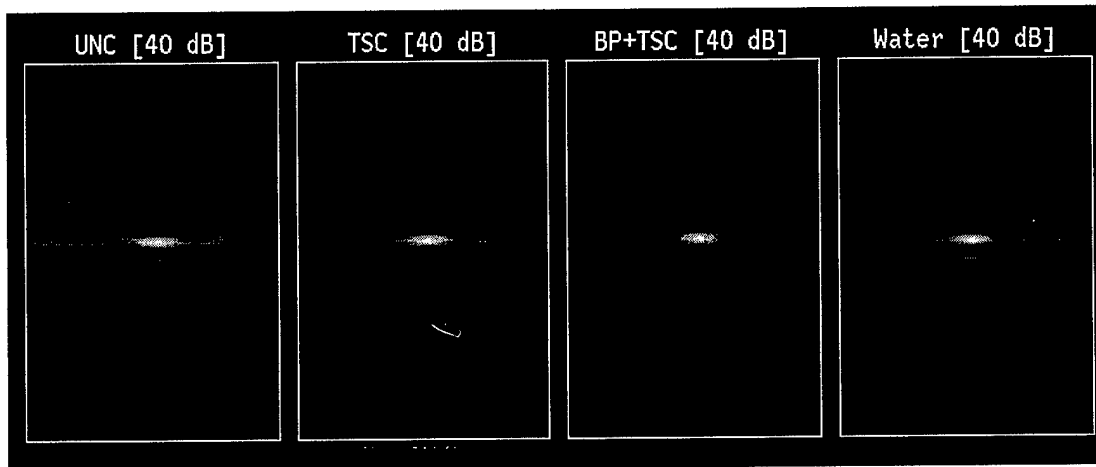
Fig. 10. Point Target Images Obtained through a Tissue Path (Left Three Panels) and through a Water Path (Rightmost Panel). The tissue path images were formed without compensation (UNC), with time-shift compensation (TSC), and with backpropagation followed by time-shift compensation (BP+TSC). In each panel, the analytic envelope is displayed on a 40 dB logarithmic scale, and the horizontal (array) direction spans 20 mm while the vertical (range or time) direction consists of 776 time samples that span 29.57 mm. The dataset was npe22.
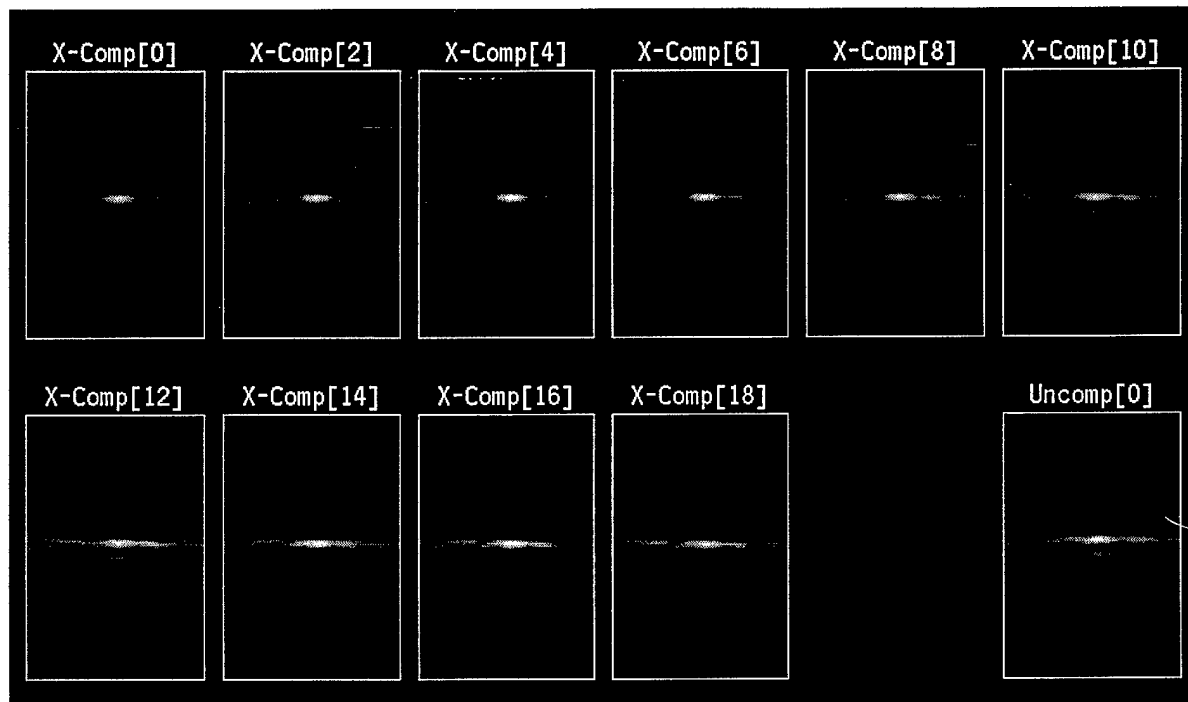
Fig. 11. Point Target Images from a Single Transmit Position for the Evaluation of Isoplanatic Patch Size. The panel X-Comp[0] is the image that results when the wavefront measured at the initial point-target position is compensated with time shifts derived from the same wavefront. The panels X-Comp[2], [4], [6], $\cdots$, [18] show images that result when wavefronts measured with the point target shifted in the azimuthal direction by 1.44 mm, 2.88 mm, 4.32 mm, $\cdots$, 12.96 mm are time-shift compensated using the time shifts derived from X-Comp[0]. The panel Uncomp[0] shows the image that results from using the uncompensated wavefront measured at the initial point-target position. The scales are the same as in Fig. 10. The dataset was npe27.
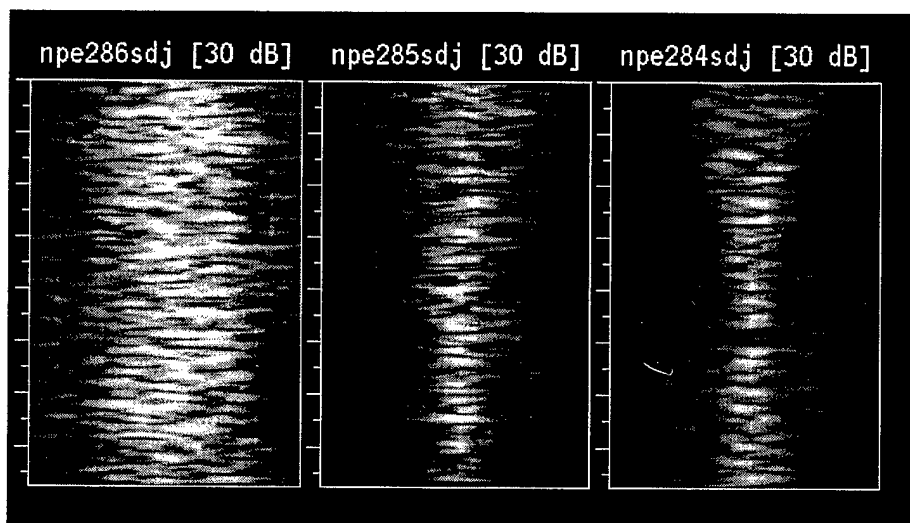
Fig. 12. Images for a Water Path from a Single Transmit Position using Three Different Diameter Transducers. For the images from left to right, the corresponding transmitter diameter was $1/2''$, $1''$, and $2''$. In each panel, the analytic envelope is displayed on a 30 dB logarithmic scale, while the horizontal and vertical scales are the same as in Fig. 10.
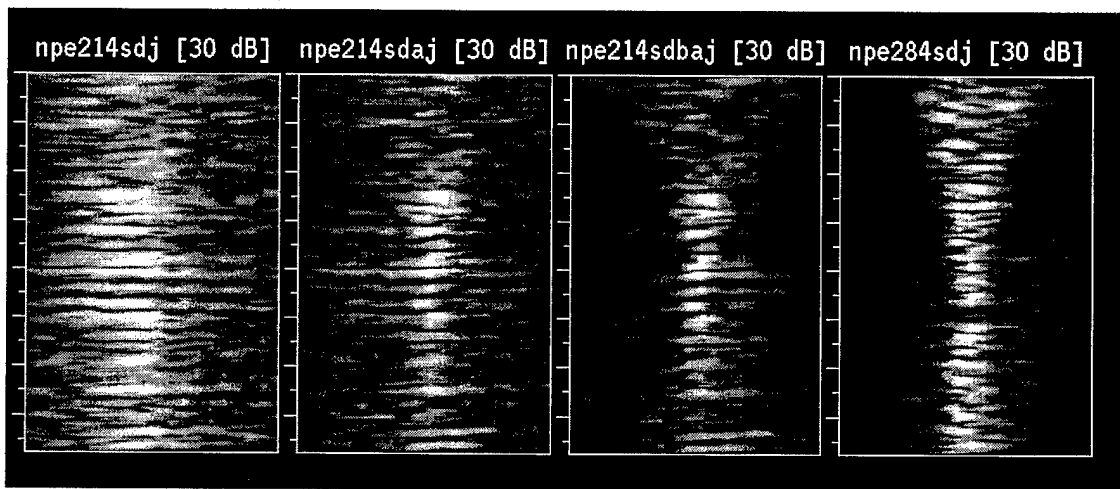
Fig. 13. Images for a Water Path and for a Tissue-Path from a Single Transmit Position under Different Conditions. The 2″ transducer was used as the transmitter for each image. The left three images were formed using tissue-path data without compensation, with time-shift compensation in the aperture, and with backpropagation by 20 mm followed by time-shift compensation, respectively. The rightmost image was formed using water-path data. The scales are the same as in Fig. 12. The dataset was npe21.

Uncomp [40 dB]	TSC [40 dB]	BP+TSC [40 dB]	Water [40 dB]
e1=79.1 e2=55.1	e1=78.1 e2=52.0	e1=76.8 e2=49.3	e1=75.6 e2=37.6
CR = 24.0 dB	CR = 26.2 dB	CR = 27.5 dB	CR = 38.0 dB
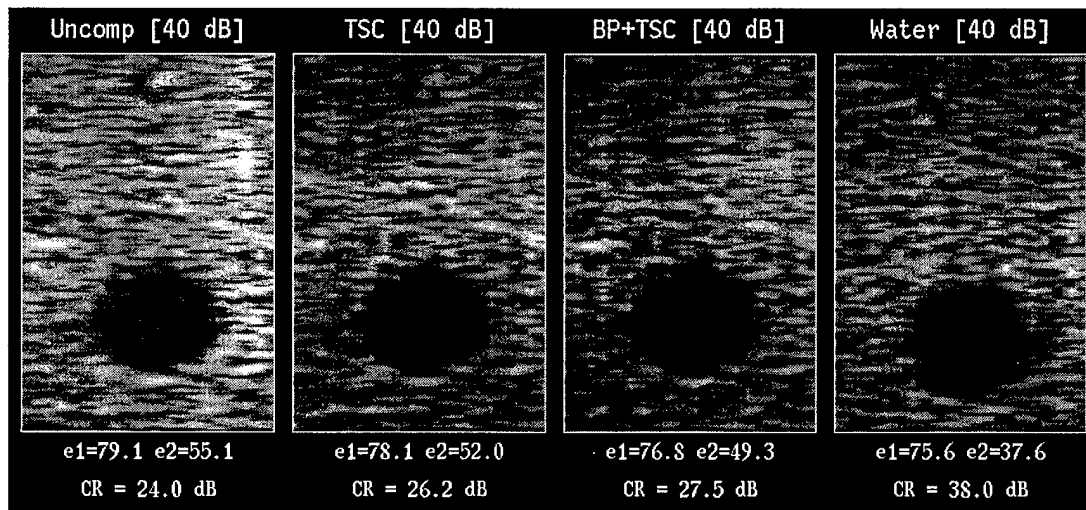
Fig. 14. B-Scan Images Corresponding to the Single Transmit Images in Fig. 13. The contrast ratio (CR) is the difference between the average energy levels for the scattering region (e1) and for the scattering-free region (e2). The scales are the same as in Fig. 10. The dataset was npe21.

Final Report   Appendix C   DAMD17-94-J-4384

Propagation and Backpropagation for Ultrasonic Wavefront Design

Dong-Lai Liu, *Member, IEEE,* and Robert C. Waag, *Fellow, IEEE*

Abstract—Wave backpropagation is a concept that can be used to calculate the excitation signals for an array with programmable transmit waveforms to produce a specified field that has no significant evanescent wave components. This concept can also be used to find the field at a distance away from an aperture based on measurements made in the aperture. For a uniform medium, three methods exist for the calculation of wave propagation and backpropagation: the diffraction integral method, the angular spectrum method, and the shift-and-add method. The boundary conditions that are usually implicitly assumed by these methods are analyzed, and the relationship between these methods are explored. The application of the angular spectrum method to other kinds of boundary conditions is discussed, as is the relationship between wave backpropagation, phase conjugation, and the time-reversal mirror. Wave backpropagation is used, as an example, to calculate the excitation signals for a ring transducer to produce a specified pulsatile plane wave with a limited spatial extent.

I. INTRODUCTION

THREE METHODS EXIST for calculating the acoustic field in a uniform medium given the vibration on a planar surface. They are the diffraction integral method [1], the angular spectrum method [2],[3], and the more empirical shift-and-add method [4]. All these methods have been widely used, yet the underlying conditions for the application of each method and the relationship between the methods have not been clearly addressed. For example, the need for the use of boundary conditions appropriate to the physical setting is obvious in the diffraction integral method, yet the boundary conditions are not obvious in the angular spectrum method and in the shift-and-add method. This implies that some choice of the boundary conditions has already been made when the latter two methods are applied.

An application in which the above issues arise is the determination of the element excitation for an array with programmable transmit waveforms to produce a specified acoustic wavefront at some position away from the array. This can be accomplished by the backpropagation of the specified wavefront to the position of each element and the assignment of the resulting signal as the excitation. The

The authors are with the Department of Electrical Engineering, University of Rochester, Rochester, New York 14627 (e-mail: liudl@ee.rochester.edu).

procedure outlined here provides a new approach to design a specified wavefront.

With a planar array, backpropagation can be performed straightforwardly using the angular spectrum method. With a curved array (like a convex or concave array), however, the angular spectrum method is not efficient, and the way to backpropagate with the other two methods is not obvious.

The purpose of this paper is to show the relationship between these methods as well as to answer the following four questions.

1. What are the implicit boundary conditions in the angular spectrum method and in the shift-and-add method?
2. How can backpropagation be accomplished using the diffraction integral method and the shift-and-add method?
3. Should the signals in the shift-and-add method be differentiated with respect to time, and should a spherical spreading factor and an obliquity factor be included?
4. How may calculations of propagation and backpropagation be implemented with curved apertures?

The computation of the ultrasonic field produced by a transducer often uses the normal component of particle velocity [5],[6]. This approach assumes, explicitly or implicitly, a rigid baffle boundary condition, by using a zero value for the normal velocity outside of the transducer surface in the transducer plane. Another common approach is the impulse response method [7] that makes the shift-and-add evaluation computationally more efficient by analytically evaluating the diffraction integral in the time domain for transducers of simple geometry. This approach also assumes the rigid baffle boundary condition. A recent paper [8] confirmed the equivalence between the impulse response method and the angular spectrum method. However, the use of a rigid baffle boundary condition may not be supported by experimental evidence in all cases.

Measurements have been performed [9],[10] to investigate the influence of boundary conditions on the acoustic field produced by an ultrasonic transducer. The usual configuration encountered in medical ultrasonic imaging, during which the transducer array is placed on the subject's skin, can be approximated by assuming the transducer to be placed at the surface of water. For the latter situation, a comparison of the water tank measurements with theoretically computed results indicates that a zero pressure boundary condition or a pressure release surface ($p = 0$ outside the transducer surface) is more appropriate than

a zero velocity boundary condition or a rigid baffle surface ($v = 0$ outside the transducer surface) [9].

A rigid baffle boundary condition, however, is more frequently used in calculating acoustic wave propagation, in spite of the above noted experimental observations. The reasons for this may include the following: (a) the prevalent influence of Rayleigh's work, particularly the Rayleigh integral, in acoutics; (b) the applicability of a rigid baffle condition to some common situations, such as a speaker mounted on a wall; and c) the small angles usually encountered in propagation calculations that make the use of the correct boundary conditions relatively unimportant. The current paucity of data suggests the need for further detailed studies, by theoretical, computational, and experimental means, of the fields produced by ultrasonic arrays in settings similar to those encountered in medical diagnosis. Such studies are, for example, important for the development of quantitative ultrasonic imaging.

The remainder of this paper is comprised of four sections: Theory, Computations and Results, Discussion, and Conclusion. In the Theory, the angular spectrum method, the diffraction integral method, and the shift-and-add method are summarized in a unified framework for calculation of wave propagation and backpropagation in a uniform medium in three-dimensional or two-dimensional spaces. An approximation is introduced to facilitate wave propagation calculations with a curved aperture. Computations based on the analytic results are presented in the next section that includes, as an example, a demonstration of the use of wave backpropagation to obtain the excitation signals for a ring transducer to produce a spatially limited plane wave. In the Discussion, the calculation of wave propagation for other boundary conditions is considered and the relationship between wave backpropagation, phase conjugation, and the time-reversal mirror is explored. The main results are summarized in the Conclusion.

II. Theory

Conventions for notation in this analysis are the following. Time dependence is assumed to be $e^{-j\omega t}$ for harmonic vibrations. Propagation or backpropagation is assumed to be along the z axis and the variable z is assumed to always denote a positive number.

A. Angular Spectrum Method

Let $p(x, y, z)$ denote the complex temporal harmonic amplitude of pressure at a single frequency in a uniform medium. Given values of $p(x, y, z)$ in the xy plane at a certain z, the angular spectrum is defined [2] as the Fourier transform of $p(x, y, z)$ with respect to x and y. The angular spectrum may thus be written

$$P(f_x, f_y, z) = \int_{-\infty}^{\infty} \int_{-\infty}^{\infty} p(x, y, z) e^{-j2\pi(xf_x + yf_y)} dx dy \ . \quad (1)$$

The relationship between $P(f_x, f_y, z)$ and $P(f_x, f_y, 0)$, the angular spectrum at $z = 0$, is obtained from the fact that $p(x, y, z)$ obeys the Helmholtz equation $(\nabla^2 + k^2)p = 0$, where $k = 2\pi/\lambda$ is the wavenumber. The result is [2]

$$P(f_x, f_y, z) = P(f_x, f_y, 0)H(f_x, f_y, z) \ , \quad (2)$$

where $H(f_x, f_y, z)$ is the so-called propagation function, which can be written explicitly as

$$
H(f_x, f_y, z) = e^{jkz\sqrt{1-\lambda^2(f_x^2+f_y^2)}}
$$
$$
= \begin{cases} e^{jkz\sqrt{1-\lambda^2(f_x^2+f_y^2)}}, & f_x^2 + f_y^2 \le 1/\lambda^2 \\ e^{-kz\sqrt{\lambda^2(f_x^2+f_y^2)-1}}, & f_x^2 + f_y^2 > 1/\lambda^2 \ . \end{cases} \quad (3)
$$

In the region $f_x^2 + f_y^2 \le 1/\lambda^2$, the propagation function has a uniform amplitude of 1, and is associated with what are known as homogeneous waves. In the region $f_x^2 + f_y^2 > 1/\lambda^2$, the propagation function decays exponentially with increasing propagation distance z, and is associated with what are known as evanescent waves.

In arriving at (3), a choice was made for the sign of the exponent. The choice was based on the physical requirement that homogeneous waves with a time dependence of $e^{-j\omega t}$ are advanced in phase to represent a time-delay, and on the fact that evanescent waves decay.

Equation (2) provides a way of calculating the field in an xy plane at an arbitrary z using $P(f_x, f_y, 0)$ or $p(x, y, 0)$. Since the calculation in (2) is a multiplication in the spatial-frequency domain, an inverse Fourier transformation to the space domain results in a convolution, which may be expressed

$$p(x, y, z) = \int_{-\infty}^{\infty} \int_{-\infty}^{\infty} p(x_0, y_0, 0) h(x - x_0, y - y_0, z) dx_0 dy_0 \ , \quad (4)$$

where

$$h(x, y, z) = \int_{-\infty}^{\infty} \int_{-\infty}^{\infty} H(f_x, f_y, z) e^{j2\pi(xf_x + yf_y)} df_x df_y \quad (5)$$

is called the impulse response function of the propagation process. An explicit form for $h(x, y, z)$ can be obtained by examining the angular spectrum of the free-space Green's function $g(r) = e^{jkr}/4\pi r$ where $r = \sqrt{x^2 + y^2 + z^2}$, which is [8],[11]

$$G(f_x, f_y, z) = \frac{j\lambda}{4\pi\sqrt{1 - \lambda^2(f_x^2 + f_y^2)}} \times e^{jk|z|\sqrt{1-\lambda^2(f_x^2+f_y^2)}} \ . \quad (6)$$

Since apparently $\partial G(f_x, f_y, z)/\partial z = -\frac{1}{2}H(f_x, f_y, z)$, an inverse Fourier transform of this relation with respect to f_x and f_y yields

$$h(x, y, z) = -2\frac{\partial}{\partial z}\left(\frac{e^{jkr}}{4\pi r}\right) = \frac{e^{jkr}}{2\pi r}\left(\frac{1}{r} - jk\right)\frac{z}{r} \ . \quad (7)$$

This result is the same as that derived in [3].

The backpropagation process is defined as the calculation of $P(f_x, f_y, 0)$ from $P(f_x, f_y, z)$. From (2), the backpropagation function may be defined as

$$H(f_x, f_y, -z) = e^{-jkz\sqrt{1 - \lambda^2(f_x^2 + f_y^2)}}$$
$$= \begin{cases} e^{-jkz\sqrt{1 - \lambda^2(f_x^2 + f_y^2)}}, & f_x^2 + f_y^2 \leq 1/\lambda^2 \\ e^{kz\sqrt{\lambda^2(f_x^2 + f_y^2) - 1}}, & f_x^2 + f_y^2 > 1/\lambda^2 \end{cases} \quad (8)$$

In the region $f_x^2 + f_y^2 > 1/\lambda^2$, $H(f_x, f_y, -z)$ grows exponentially with z, signifying that evanescent waves get an exponential amplification to compensate for the exponential decay they undergo in forward propagation. Because $H(f_x, f_y, -z)$ is unbounded in the region $f_x^2 + f_y^2 > 1/\lambda^2$, however, its inverse Fourier transform does not exist so that the impulse response function of backpropagation cannot be defined.

To circumvent this problem, consider two scenarios in which backpropagation might be used. One is to find excitation signals for the production of a specified field. The other is to calculate the field at some distance from a measurement aperture. At the position of specification or measurement, because the spatial sampling rate is always finite, the maximum spatial frequency $f_{\max}$ that the data can represent is also finite, and the magnitude of angular spectrum is assumed to be zero beyond $f_{\max}$. In these cases, therefore, the definition of $H(f_x, f_y, -z)$ can be modified by letting $H(f_x, f_y, -z) = 0$ for $f_x^2 + f_y^2 > f_{\max}^2$. Then, the inverse Fourier transform $H(f_x, f_y, -z)$ can be evaluated at least numerically. If $f_{\max} > 1/\lambda$, using such a backpropagation function still implies the exponential amplification of the evanescent waves whose magnitude of spatial frequency is between $1/\lambda$ and $f_{\max}$.

Evanescent waves have negligible amplitudes if the distance of propagation is more than a few wavelengths. For example, for an evanescent wave component with spatial frequency at $2/\lambda$ (double the highest spatial frequency of nonevanescent waves), the amplitude after propagating 2λ will be, according to (3), reduced by $e^{-2\pi \times 2 \times \sqrt{3}} = 3.5 \times 10^{-10}$, which is about -200 dB. This huge attenuation implies that to produce evanescent waves beyond a few wavelengths from the aperture is almost impossible, and to determine the existence of evanescent waves at a few wavelengths away is also almost impossible. In this case, the handling of evanescent waves becomes unimportant, and an arbitrary function may be used to replace the growing exponential in (8) to make the inverse Fourier transform well defined. One particular approximation that leads to an analytic form of the inverse Fourier transform is

$$\tilde{H}(f_x, f_y, -z) = H^*(f_x, f_y, z)$$
$$= \begin{cases} e^{-jkz\sqrt{1 - \lambda^2(f_x^2 + f_y^2)}}, & f_x^2 + f_y^2 \leq 1/\lambda^2 \\ e^{-kz\sqrt{\lambda^2(f_x^2 + f_y^2) - 1}}, & f_x^2 + f_y^2 > 1/\lambda^2 \end{cases} \quad (9)$$

which is obtained by replacing the growing exponential in (8) for the evanescent waves by a decaying exponential. The corresponding approximate backpropagation impulse

response function is the complex conjugate of $h(x, y, z)$,

$$\tilde{h}(x, y, -z) = -2\frac{\partial}{\partial z}\left(\frac{e^{-jkr}}{4\pi r}\right) = \frac{e^{-jkr}}{2\pi r}\left(\frac{1}{r} + jk\right)\frac{z}{r} .$$
$$(10)$$

The results in (9) and (10) developed here for acoustic applications have also been derived [12],[13] independently using similar reasoning and approximation for optical applications.

Since a forward propagation followed by a backpropagation of equal distance should ideally restore the wavefront, a good way of examining $\tilde{h}(x, y, -z)$ as an approximation of the ideal backpropagation impulse response function is to calculate the convolution of $h(x, y, z)$ and $\tilde{h}(x, y, -z)$ with respect to x and y, and to compare the result with the delta function, i.e., to check the accuracy of

$$4\frac{\partial}{\partial z}\left(\frac{e^{jkr}}{4\pi r}\right) * \frac{\partial}{\partial z}\left(\frac{e^{-jkr}}{4\pi r}\right) \approx \delta(x)\delta(y) . \quad (11)$$

B. Diffraction Integral Method

Since p satisfies the Helmholtz equation $(\nabla^2 + k^2)p = 0$, the value of p at an arbitrary point $\vec{r} = (x, y, z)$ can be expressed as the surface integral [11]

$$p(\vec{r}) = \iint\limits_{S_0} \left[G(\vec{r}|\vec{r}_0)\frac{\partial p(\vec{r}_0)}{\partial \vec{n}_0} - p(\vec{r}_0)\frac{\partial G(\vec{r}|\vec{r}_0)}{\partial \vec{n}_0} \right] d\vec{r}_0 ,$$
$$(12)$$

where S_0 is an arbitrary surface enclosing the point $\vec{r}$, $\vec{r}_0$ is a point on S_0, and $\vec{n}_0$ is the outward pointing normal vector of S_0 at $\vec{r}_0$. This formula enables the calculation of $p(\vec{r})$ from simultaneous knowledge of both $p(\vec{r}_0)$ and $\partial p(\vec{r}_0)/\partial \vec{n}_0$ on the surface S_0. The Green's function $G(\vec{r}|\vec{r}_0)$ to be used in the above formula is a general solution of the equation $(\nabla^2 + k^2)G(\vec{r}|\vec{r}_0) = -\delta(\vec{r} - \vec{r}_0)$, and consists of two terms

$$G(\vec{r}|\vec{r}_0) = g(R) + \chi(\vec{r}) = \frac{e^{jkR}}{4\pi R} + \chi(\vec{r}) , \quad (13)$$

where $R = |\vec{r} - \vec{r}_0|$ is the distance between $\vec{r}$ and $\vec{r}_0$, $g(R)$ is the free-space outgoing Green's function as already defined, and $\chi(\vec{r})$ is an arbitrary function satisfying the Helmholtz equation $(\nabla^2 + k^2)\chi(\vec{r}) = 0$ in the volume surrounded by the surface S_0. An arbitrary choice of $\chi(\vec{r})$ will not change the result computed by (12), but an appropriate choice of this function eliminates the need of simultaneous knowledge of both $p(\vec{r}_0)$ and $\partial p(\vec{r}_0)/\partial \vec{n}_0$ on the surface S_0, thereby preventing the boundary conditions from being overspecified.

Consider the case of S_0 being comprised of the plane $z = 0$ and the hemisphere at infinity enclosing the upper half space. The behavior of the pressure field at infinity is specified to satisfy the Sommerfeld radiation condition [2]. Under these conditions, the formulae for computing $p(\vec{r})$ using either $p(\vec{r}_0)$ alone or $\partial p(\vec{r}_0)/\partial \vec{n}_0$ alone are

well-known [11],

$$p(x, y, z) = \frac{z}{2\pi} \int\limits_{-\infty}^{\infty} \int\limits_{-\infty}^{\infty} p(x_0, y_0, 0) \left(\frac{1}{R} - jk\right) \frac{e^{jkR}}{R^2} \, dx_0 dy_0 \ , \tag{14}$$

or

$$p(x, y, z) = -\frac{1}{2\pi} \int\limits_{-\infty}^{\infty} \int\limits_{-\infty}^{\infty} \frac{\partial p(x_0, y_0, z_0)}{\partial z_0} \bigg|_{z_0=0} \frac{e^{jkR}}{R} \, dx_0 dy_0 \ . \tag{15}$$

In these expressions, $R = \sqrt{(x - x_0)^2 + (y - y_0)^2 + z^2}$. When pressure is specified in the $z = 0$ plane (known as the Dirichlet boundary condition), (14) applies. A special case of the Dirichlet boundary condition is the pressure release surface, in which the pressure is specified on the transducer surface and is assumed to be zero elsewhere in the transducer plane. When the normal derivative of pressure is specified in the $z = 0$ plane (known as the Neuman boundary condition), (15) applies. A special case of the Neuman boundary condition is the rigid baffle surface, in which the normal velocity (which is proportional to the normal derivative of the pressure) is specified on the transducer surface and is assumed to be zero elsewhere in the transducer plane. A comparison of (14) with (4) and (7) immediately reveals that the angular spectrum computation corresponds to the Dirichlet boundary condition. This conclusion is not surprising, since the angular spectrum method assumes that values of $p(x, y, z)$ are specified in the plane $z = 0$.

An equation that describes backpropagation and forms a pair with (14) is obtained using the approximate impulse response function of backpropagation in (10). The result is

$$p(x_0, y_0, 0) \approx \frac{z}{2\pi} \int\limits_{-\infty}^{\infty} \int\limits_{-\infty}^{\infty} p(x, y, z) \left(\frac{1}{R} + jk\right) \frac{e^{-jkR}}{R^2} \, dxdy \ . \tag{16}$$

The approximation in (16) is due, as already noted, to the exponential decay of evanescent waves during backpropagation instead of exponential amplification.

C. Propagation and Backpropagation by Shift-And-Add

The shift-and-add method can be derived from the diffraction integrals by an inverse Fourier transform of (14) and (16) with respect to time followed by a discretization of the integrals in space. An approximation is customarily made under the assumption that the distance R is much larger than the wavelength λ (as is usually the case). By omitting the term $1/R$ in the parentheses and denoting $p(x, y, z)$ by $p_\omega(x, y, z)$ to signify that the equation applies to a single frequency component, (14) becomes

$$p_\omega(x, y, z) = \frac{-jkz}{2\pi} \int\limits_{-\infty}^{\infty} \int\limits_{-\infty}^{\infty} p_\omega(x_0, y_0, 0) \frac{e^{jkR}}{R^2} dx_0 dy_0 \ . \tag{17}$$

The inverse Fourier transform of (17) with respect to temporal frequency then yields

$$p(x, y, z, t) = \frac{z}{2\pi c} \int\limits_{-\infty}^{\infty} \int\limits_{-\infty}^{\infty} \dot{p}(x_0, y_0, 0, t - R/c) \frac{1}{R^2} \, dx_0 dy_0 \ , \tag{18}$$

where $p(x, y, z, t)$ denotes the temporal pressure variation at point (x, y, z) and $\dot{p}$ denotes the differentiation of p with respect to time. The validity of the approximation leading to (18) requires the relation $R \gg \lambda$ to hold for all the significant frequency components contained in $p(x_0, y_0, 0, t)$. Subsequent discretization of (18) with respect to (x_0, y_0) leads to

$$p(x, y, z, t) = \frac{z}{2\pi c} \Delta x_0 \Delta y_0$$
$$\times \sum_m \sum_n \dot{p}(x_{0m}, y_{0n}, 0, t - R_{mn}/c) \frac{1}{R_{mn}^2} \ , \tag{19}$$

where $R_{mn} = \sqrt{(x - x_{0m})^2 + (y - y_{0n})^2 + z^2}$. Since (19) corresponds to time-shifting and adding signals at $z = 0$ to obtain signals in the plane at z, the name shift-and-add is given to the method. Similarly, the spatially discretized, time-domain version of (16) with the assumption $R \gg \lambda$ can be written as

$$p(x_0, y_0, 0, t) = -\frac{z}{2\pi c} \Delta x \Delta y$$
$$\times \sum_p \sum_q \dot{p}(x_p, y_q, z, t + R_{pq}/c) \frac{1}{R_{pq}^2} \ , \tag{20}$$

where $R_{pq} = \sqrt{(x_0 - x_p)^2 + (y_0 - y_q)^2 + z^2}$.

Both (19) and (20) come from results that were obtained for a planar geometry. Thus, these equations also only apply directly to a planar geometry, although the requirement is limited to the source aperture in the case of (19) and to the field measurement aperture in the case of (20). An approximate extension of these results to more general aperture shapes is possible, as described in the next section.

D. Propagation and Backpropagation in Two-dimensional Space

Assume now that the field varies only in the x and z directions and is constant in the y direction so the wave propagation is in two dimensions. The angular spectrum method can be applied to two-dimensional wave propagation with essentially no change in form. The corresponding propagation function is

$$H(f_x, z) = e^{jkz\sqrt{1 - \lambda^2 f_x^2}}$$
$$= \begin{cases} e^{jkz\sqrt{1 - \lambda^2 f_x^2}}, & f_x^2 \leq 1/\lambda^2 \\ e^{-kz\sqrt{\lambda^2 f_x^2 - 1}}, & f_x^2 > 1/\lambda^2 \ , \end{cases} \tag{21}$$

and the corresponding approximate backpropagation function is

$$\tilde{H}(f_x, -z) = \begin{cases} e^{-jkz\sqrt{1-\lambda^2 f_x^2}}, & f_x^2 \leq 1/\lambda^2 \\ e^{-kz\sqrt{\lambda^2 f_x^2 - 1}}, & f_x^2 > 1/\lambda^2 \end{cases}. \quad (22)$$

Using an approach similar to the one leading to (7), the inverse Fourier transform of $H(f_x, z)$ is found to be

$$h(x, z) = \int_{-\infty}^{\infty} H(f_x, z) e^{j2\pi x f_x} df_x = \frac{1}{2j} \frac{\partial}{\partial z} \left[H_0^{(1)}(kr) \right], \quad (23)$$

where $r = \sqrt{x^2 + z^2}$ and

$$H_0^{(1)}(\xi) = J_0(\xi) + jN_0(\xi) \rightarrow \sqrt{\frac{2}{\pi\xi}} e^{j(\xi - \pi/4)} \quad \text{as } \xi \rightarrow \infty \quad (24)$$

is the zeroth-order Hankel function of the first kind. A check on the accuracy of the asymptotic form using the IMSL library [14] indicates that the relative rms error for the real and the imaginary parts is less than 0.1% for $\xi = kr > 100$. Using the asymptotic form, the impulse response function of forward propagation is found to be

$$h(x, z) \approx \frac{1}{\sqrt{\lambda r}} e^{j(kr - \pi/4)} \frac{z}{r}. \quad (25)$$

The asymptotic form of the inverse Fourier transform of $\tilde{H}(f_x, -z)$ is similarly found to be

$$\tilde{h}(x, -z) \approx \frac{1}{\sqrt{\lambda r}} e^{-j(kr - \pi/4)} \frac{z}{r}. \quad (26)$$

The above impulse response functions $h(x, z)$ and $\tilde{h}(x, -z)$, as well as those presented in (7) and (10) for wave propagation in three-dimensional space, were obtained assuming a planar geometry. In practice, however, curved apertures may be encountered. To propagate from such an aperture or to backpropagate fields measured by such an aperture, an extension of these results to a curved geometry is needed.

A rigorous approach to treat a curved aperture is to find the Green's function in the form of (13) for the particular geometry and then to use that Green's function in (12). However, an analytic solution for $\chi(\vec{r})$ is known only for a few simple geometries. Therefore, this approach does not usually lead to uncomplicated analytic results.

Instead, a closer examination of the planar geometry result using the impulse response function proves worthwhile. In the following, $h(x, z)$ in (25) for wave propagation in two-dimensional space will be used as an example for this examination. The field $p(x, z)$ caused by a vibration $p(x, 0)$ at $z = 0$ can be expressed using $h(x, z)$,

$$p(x, z) = \int_{-\infty}^{\infty} p(x_0, 0) h(x - x_0, z) dx_0$$

$$\approx \int_{-\infty}^{\infty} p(x_0, 0) \frac{1}{\sqrt{\lambda r}} e^{j(kr - \pi/4)} \cos\theta dx_0, \quad (27)$$

where $r = \sqrt{(x - x_0)^2 + z^2}$ and $\cos\theta = z/r$ with θ being the angle between the normal of the aperture and the line that connects the aperture point and the field point, as shown in Fig. 1. The factor $\cos\theta$ is known as the obliquity factor. In order to generalize this result to an arbitrary aperture shape, the contribution of a line segment $p(x_0, 0) dx_0$ in the planar aperture to the field at (x, z) is examined. Apart from terms related to time delay, phase shifting, and amplitude scaling, the term $\cos\theta$ relates to the directivity of the radiation pattern of the line segment. Now, assume that the radiation pattern of a line segment in a curved aperture is little influenced by the overall shape of the aperture and is the same as the radiation pattern of a line segment in a planar aperture. (See Fig. 1.) This is probably a good approximation as long as the radius of curvature of the aperture is much larger than the wavelength (so that in the vicinity of each line segment the aperture is almost flat). Using this approximation, the contribution from individual line segments $p(x_0, z_0) ds_0$ can be found using the same formula as in (27) and the total field is obtained by a summation. The result is

$$p(x, z) \approx \int_{-\infty}^{\infty} p(x_0, z_0) \frac{1}{\sqrt{\lambda r}} e^{j(kr - \pi/4)} \cos\theta ds_0, \quad (28)$$

where $z > z_0$, $r = \sqrt{(x - x_0)^2 + (z - z_0)^2}$, ds_0 is a line segment along the curved aperture, and θ is the angle between the normal vector and the vector $\vec{r}$. A similar approach was used [15] to extend the impulse response method (which assumes the rigid baffle boundary condition) from a planar aperture to a curved aperture. Consider a circular aperture of radius R that spans an angle A. This geometry is shown in Fig. 2. The field produced by this aperture can be approximately computed using (28),

$$p(x, z) \approx \int_{-A/2}^{A/2} p(R\sin\alpha, -R\cos\alpha) \frac{1}{\sqrt{\lambda r}}$$
$$\times e^{j(kr - \pi/4)} \frac{R^2 + r^2 - (x^2 + z^2)}{2Rr} R d\alpha. \quad (29)$$

Backpropagation of a field measured along a curve can be computed using the same approximation with the obliquity factor $\cos\theta$ modified according to the geometry. The formula is

$$p(x, z) \approx \int_{-\infty}^{\infty} p(x_0, z_0) \frac{1}{\sqrt{\lambda r}} e^{-j(kr - \pi/4)} \cos\theta ds_0, \quad (30)$$

where $z < z_0$.

The time-domain counterparts of (28) and (30) cannot be written explicitly because the amplitude scaling contains a frequency-dependent factor $1/\sqrt{\lambda} = \sqrt{f/c}$, where f is temporal frequency and c is sound speed. Thus, the computation of a pulse wavefront propagating in two-dimensional space needs to be carried out for each harmonic frequency component of the pulse individually. The
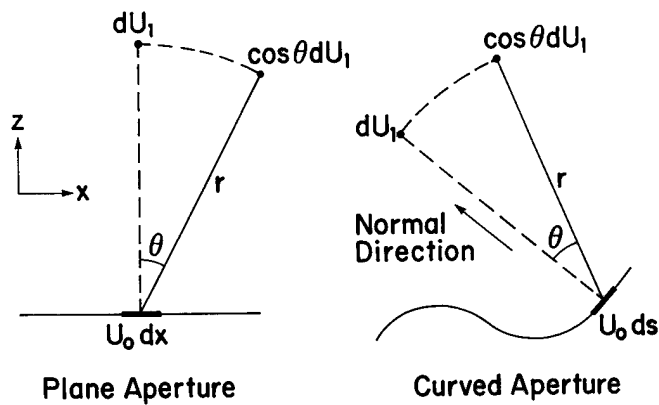
Fig. 1. Transition from a planar aperture to a curved aperture. In a planar aperture (left), the contribution of an aperture segment $U_0 dx$ to a field point in the normal direction is denoted by dU_1. The contribution to a field point at the same distance but at an angle θ from normal is given by $\cos\theta dU_1$ according to (27). In a gradually curved aperture (right), the radiation directivity of $\cos\theta$ is assumed to be little influenced by the overall aperture shape and is used to compute the field contribution by a segment of the aperture.
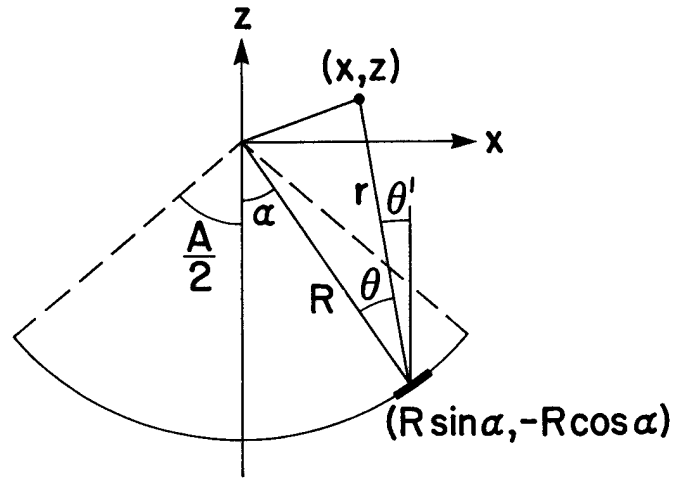

Fig. 2. Geometry for the calculation of obliquity factor for a circular aperture. The angle θ is between the normal direction and the vector $\vec{r}$ that goes from the aperture point to the field point. The angle θ' is between the z axis and the vector $\vec{r}$.

final result in the time domain can be obtained by adding the results for each harmonic frequency together.

III. COMPUTATIONS AND RESULTS

Computations were made to examine the validity of (11) in a particular configuration, to investigate the effects of the obliquity factor in three-dimensional as well as in two-dimensional wave propagation, and to demonstrate the use of backpropagation to determine element excitation of a ring transducer for the creation of a spatially limited plane wave.

A. Examination of the Validity of (11)

The computations were performed in the following way. First, complex functions $h(x, y, z)$ and $\tilde{h}(x, y, -z)$ were evaluated on an (x, y) grid in the space domain. These discrete functions were then Fourier transformed using two-dimensional FFT, and the product of the transforms was then inverse Fourier transformed. The use of Fourier transform in these computations provides an efficient evaluation of the two-dimensional convolution in (11).

The following parameters in the computation were chosen for their applicability in medical ultrasonic imaging. The center frequency was 3.75 MHz. The sound speed was 1.5 mm/μs. The distance of propagation (z) was 10 mm. This distance was intentionally kept relatively short so that the impulse response function $h(x, y, z)$ has significant values over a relatively small area and can, thus, be represented with fewer samples. This distance was large enough, however, so that evanescent waves can be safely ignored. An (x, y) grid spacing of 0.1 mm $\times$ 0.1 mm was used. This sampling interval is less than half the wavelength, which is 0.4 mm at 3.75 MHz, and satisfies the sampling theorem requirement.

Test computations were performed to determine the necessary coverage of the xy plane, or the grid size. The expected angular spectrum of $h(x, y, z)$ has unit amplitude in the region $\sqrt{f_x^2 + f_y^2} < 1/\lambda$ and decays exponentially beyond that. The graphical appearance of the magnitude of the angular spectrum is a disk. A grid size of 512×512 points with the grid spacing of 0.1 mm $\times$ 0.1 mm resulted in four corners in the calculated angular spectrum. These were caused by the truncation of $h(x, y, z)$ in space because only an area of 51.2×51.2 mm^2 was covered in this case while $h(x, y, z)$ extends throughout the entire xy plane. When the grid size was increased to 1024×1024 points, the four corners disappeared, showing that the spatial coverage in this case was sufficient to make the spatial truncation insignificant. Zero-padding to 2048×2048 points in space was then used to avoid wraparound errors that may occur in the evaluation of the convolution in (11) using a two-dimensional FFT. (Wraparound error occurs when the dimensions of the expected convolution result exceed the dimensions of the FFT.)

The results are illustrated in Fig. 3. These results have been normalized with respect to the grid spacing by multiplying the FFT result and the convolution result by spatial sampling intervals $\Delta x \Delta y$. The maximum magnitude of $h(x, y, z)$ in panel (a) is at $x = y = 0$ and equals about $1/\lambda z$, which has the numerical value of 0.25 for $\lambda = 0.4$ mm and $z = 10$ mm. In panel (b) that shows the magnitude of the angular spectrum of the impulse response, the diameter of the disk is about 1000 FFT points, whereas 2048 FFT points corresponds to the spatial sampling frequency, which is 10 points per millimeter. Thus, the radius is at a spatial frequency of approximately 2.5 cy/mm, which is the expected $1/\lambda$. The magnitude in panel c) at $f_x = f_y = 0$ is seen to be close to 1.0, as predicted by (3). Some ringing around the transition to the evanescent wave region is seen in the magnitude. This is a representation of
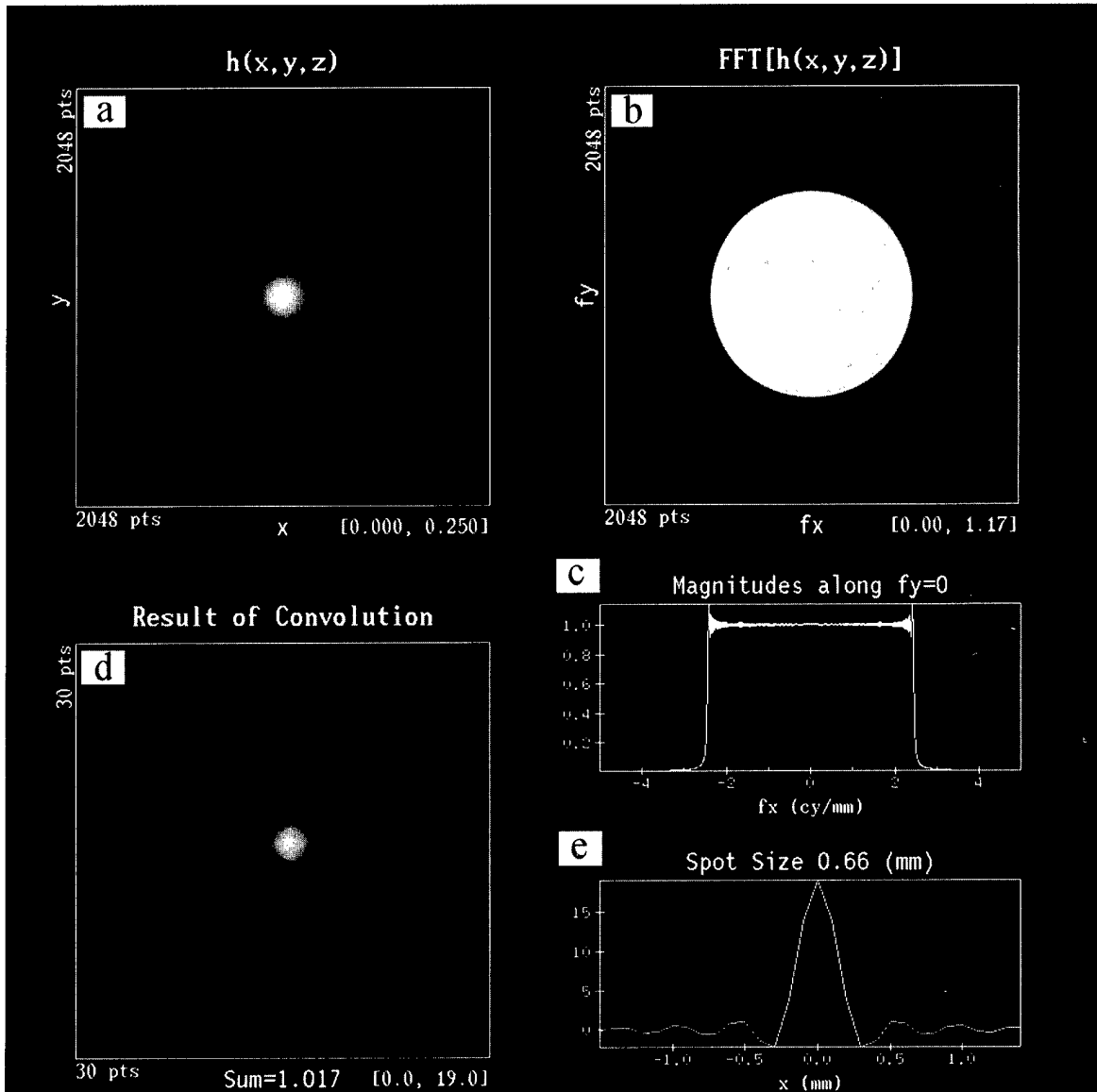
Fig. 3. Computations associated with the impulse response functions $h(x, y, z)$ in (7) and $\tilde{h}(x, y, -z)$ in (10). (a) Magnitude of $h(x, y, z)$ at $z = 10$ mm. The function is sampled by 1024×1024 points with a spatial sampling interval of 0.1 mm and zero-padded to 2048×2048 points. (b) Magnitude of the angular spectrum of $h(x, y, z)$. (c) Magnitude along the central horizontal line ($f_y = 0$) of panel (b). (d) Magnitude of the central 30×30 points that result from convolving $h(x, y, z)$ with $\tilde{h}(x, y, -z)$. (e) The real part of the convolution result along the central horizontal line ($y = 0$).

the Gibbs phenomenon. By applying an appropriate, non-rectangular, window to $h(x, y, z)$ in space domain, the ringing in its angular spectrum could be minimized [3], but as this was not a concern in the current investigation, a uniform or rectangular window was used. The result of convolution of $h(x, y, z)$ and $\tilde{h}(x, y, -z)$ is presented in panel d) using the central 30×30 samples to show details of the result, since the whole image of 2048×2048 samples produces important nonzero values only in the neighborhood of the center. The integration of the real part of the convolution over the 2048×2048 points was found to be 1.017, very close to the expected value of 1.0. (The imaginary part is essentially zero other than numerical errors, due to finite precision arithmetic.) The distance between the two minima surrounding the peak along the central horizontal

line, shown in panel e), was found via spline interpolation to be about 0.66 mm. This result can be compared to an analytical result, obtained by taking the inverse Fourier transform of the disk-shaped angular spectrum (ignoring evanescent waves). The result is the well-known Airy function of the form $J_1(k\rho)/k\rho$ with $\rho = \sqrt{x^2 + y^2}$, and the two minima surrounding the peak would be 1.635λ apart, which is 0.654 mm at the wavelength of 0.4 mm. The oscillatory tail in the plot is due to the sharp edges in the spectra of $h(x, y, z)$ and $h(x, y, -z)$.

A similar calculation was performed for $-2jkg(x, y, z)$ and $2jkg^*(x, y, z)$. These functions are good approximations to $h(x, y, z)$ and $\tilde{h}(x, y, -z)$ with the obliquity factor z/r removed, and would correspond to propagation and backpropagation by shift-and-add using a unit obliq-
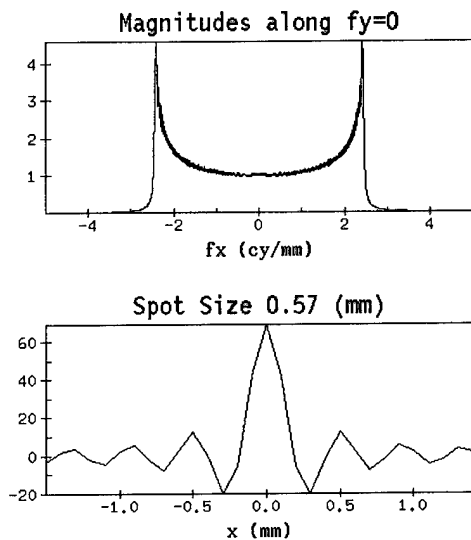
Fig. 4. Computations associated with the free-space Green's function. The two panels correspond to panels c) and e) in Fig. 3.
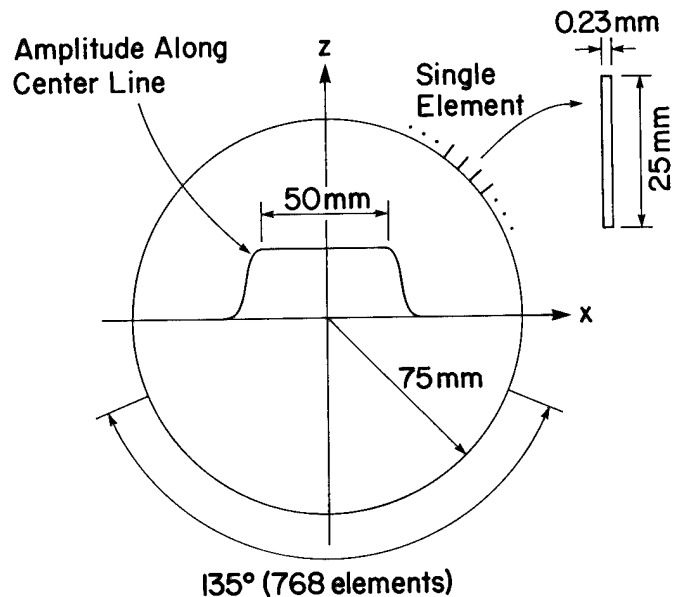

Fig. 5. Ring transducer and spatially limited plane wave. The ring is composed of 2048 elements, with the longer dimension of each element being parallel to the ring axis or perpendicular to the paper plane. A wavefront whose amplitude $a(x)$ along the diameter is uniform at the central region of 50 mm is to be produced. A cosine roll-off extending 1 mm on each side of the central region is used to provide a smooth transition in amplitude.

uity factor. The angular spectrum of $-2jkg(x, y, z)$ along $f_y = 0$ and the result of convolution along $y = 0$, calculated using the same parameters as used for the calculations in Fig. 3, are presented in Fig. 4. As can be seen in Fig. 4, the magnitude of the angular spectrum, which equals $[1 - \lambda^2(f_x^2 + f_y^2)]^{-1/2}$, increases from unity to infinity as the spatial frequency increases from zero to $1/\lambda$. The singularity in the angular spectrum of $g(x, y, z)$ is due to the uniform angular distribution of energy radiated from a point source [16]. The result of convolution is more oscillatory in Fig. 4 than in Fig. 3, because the discontinuity in the angular spectrum at $f_x^2 + f_y^2 = 1/\lambda^2$ is greater. The integration of the real part of the convolution over the 2048×2048 points was found to be 1.091, farther away from the expected 1.0 value than the 1.017 in Fig. 3. The distance between the two minima surrounding the peak is found to be about 0.57 mm, which is 14% smaller than the spot size of Fig. 3.

B. Use of Backpropagation to Determine Element Excitation for the Creation of a Specified Field

The problem that initially stimulated the investigation presented here is to prescribe a set of waveforms that may be applied to a segment of the elements of a ring transducer to create a spatially limited plane wave at the center of the ring. This ring transducer was developed by a team at University of Rochester for ultrasonic scattering and imaging studies. The ring transducer has a diameter of 150 mm and consists of 2048 elements, each able to transmit and receive independently with a center frequency of 2.43 MHz and a −6 dB bandwidth of 1.71 MHz. The transmit waveform (pulse shape) is independently specifiable for each element, a unique capability not found in commercial ultrasonic imaging systems. A diagram of the geometry is shown in Fig. 5.

The field along the 150 mm diameter was discretized into 1000 points. This discretization meets the sampling requirement for waves with a frequency up to 5 MHz. The field was specified to have a uniform amplitude for the central 50 mm with an additional 1 mm cosine roll-off at each end, and to have zero amplitude along the remainder of the diameter. The pulse waveform was specified to have a Gaussian envelope, a center frequency of 2.43 MHz, and a −6 dB bandwidth of 1.71 MHz. The field was thus represented as

$$p(x, t) = a(x)e^{-t^2/2\sigma_T^2}\sin(2\pi f_0 t) , \qquad (31)$$

where $a(x)$ is as shown in Fig. 5, $f_0 = 2.43$ MHz, and σ_T was adjusted to meet the −6 dB bandwidth requirement. The pulse wavefront was temporally sampled at 20 MHz.

The basic approach was to backpropagate the specified field to the position of each element and prescribe the calculated vibration as the excitation signal for that element. The field produced by the prescribed excitation was then calculated (using forward propagation) and compared to the specified field. Experimental verification is beyond the scope of this paper (but is planned for inclusion in another manuscript).

In the computations, two-dimensional wave propagation was used as opposed to three-dimensional wave propagation for three reasons. First, putting the physical ring transducer aside, a check of the approximations used to obtain (28) and (30), i.e., to see how well a backpropagation to a curved aperture followed by a forward propagation from that curved aperture restores the original wavefront, is of interest. Second, the far-field point of each element in

the elevation (height) direction, estimated using $h^2/4\lambda$, in which $h = 25$ mm is element height and $\lambda = 0.6$ mm is the center frequency wavelength, is 260 mm away from the element. This is significantly larger than the ring radius (75 mm) and indicates that each element is closer to a line source than a point source and that wave spread in the elevation direction is small within the range of consideration. Third, the ring transducer is essentially a one-dimensional array so that each element of the transducer can only act as a line transmitter or a line receiver (of finite length) and cannot be divided into smaller units along the elevation direction. Thus, three-dimensional wave propagation results cannot be applied directly to the ring transducer system.

The results of the two-dimensional wave propagation and backpropagation calculations described above are shown in Fig. 6. The number of elements used for the production of the spatially-limited plane wave was 768 (out of the total of 2048). This number was chosen based on tests that showed that the calculated excitation falls off to a negligible amplitude beyond that aperture size. To reduce computation, the forward propagation of the excitation signals was made with a coarser spatial sampling, in which 100 positions were employed to cover the ring diameter (150 mm). A small error (about 0.9% in magnitude) was observed at the border of the spatially limited plane wavefront. The error is attributed to the existence of a nonnegligible amount of evanescent wave energy in the specified field. In fact, when the width of cosine rolloffs was increased from 1 mm to 5 mm, the error reduced dramatically to 0.03%.

In the above computation, (29) was used to calculate the forward propagation from the circular aperture. For comparison, computations were also made to investigate the error that can be caused by using incorrect obliquity factors. Two incorrect obliquity factors were considered: unity and $\cos\theta'$ with θ' being the angle between the z axis and the vector $\vec{r}$ (Fig. 2). In Fig. 7, the amplitudes across the diameter are plotted for the originally specified field and for three other fields, all obtained with backpropagation of the specified field to the ring followed by forward propagation, but using the three different obliquity factors during forward propagation. The error caused by the use of incorrect obliquity factors is clearly shown.

IV. DISCUSSION

A. Nonplanar Geometry and Efficiency of Computation

The extension of wave propagation formulae from a planar aperture to curved apertures was only presented for two-dimensional space. However, the same kind of extension applies as well to calculations of three-dimensional wave propagation, using either the diffraction integral method or the shift-and-add method, but not the angular spectrum method (because the last method is inherently based on a planar geometry). The extension is, however,

approximate and applies only to curved apertures whose radius of curvature is much greater than the wavelength.

A different approach is possible for wave propagation calculations associated with a nonplanar geometry. The approach initially propagates the field from a curved surface to a close-by planar surface. As long as the distance of propagation is small, a simple time delay or a phase shift (for a single frequency component) can be used to perform the propagation approximately. Then, the propagation or backpropagation starting from the planar surface can be performed exactly as described here. This approach is similar to the thin lens approximation used in optics.

The numerical efficiency of the angular spectrum method for planar geometry deserves emphasis. For each single frequency, the propagation from one plane to another plane requires only a Fourier transform, a complex multiplication, and an inverse Fourier transform. The Fourier transforms can be implemented using a Fast Fourier Transform algorithm. As a result, for the calculation of propagation or backpropagation between two planes, the angular spectrum method is computationally the most efficient. However, this method is not applicable if the propagation or backpropagation starts from a curved boundary, in which case the other two methods may be employed with the above-mentioned extension.

B. Angular Spectrum Method with Other Boundary Conditions

The angular spectrum calculation in the theory section for three-dimensional wave propagation proceeds under the assumption that values of pressure $p(x, y, z)$ are given in the aperture. The calculation requires modification when other kinds of boundary conditions are specified. Consider a planar surface of local reaction [11] with a uniform impedance Z. The boundary condition imposed by the surface is

$$\frac{1}{Z}p(x, y, 0) + v_z(x, y, 0) = b(x, y) \ , \qquad (32)$$

where v_z is the normal velocity which is related to the normal derivative of pressure through

$$v_z(x, y, 0) = \frac{1}{j\omega\rho} \left. \frac{\partial p(x, y, z)}{\partial z} \right|_{z=0} \ , \qquad (33)$$

and $b(x, y)$ is the boundary value that is usually nonzero on the surface of the transducer and zero elsewhere. Substituting (33) into (32), taking Fourier transform with respect to x and y, and using the fact that the Fourier transform of $\partial p/\partial z$ at $z = 0$ equals $P(f_x, f_y, 0)$ times $jk\sqrt{1 - \lambda^2(f_x^2 + f_y^2)}$, as is evident from (2), yields

$$P(f_x, f_y, 0) = \frac{B(f_x, f_y)}{\frac{1}{Z} + \frac{1}{\rho c}\sqrt{1 - \lambda^2(f_x^2 + f_y^2)}} \ , \qquad (34)$$

where $B(f_x, f_y)$ is the Fourier transform of $b(x, y)$. Once $P(f_x, f_y, 0)$ is available, $P(f_x, f_y, z)$ at an arbitrary z can
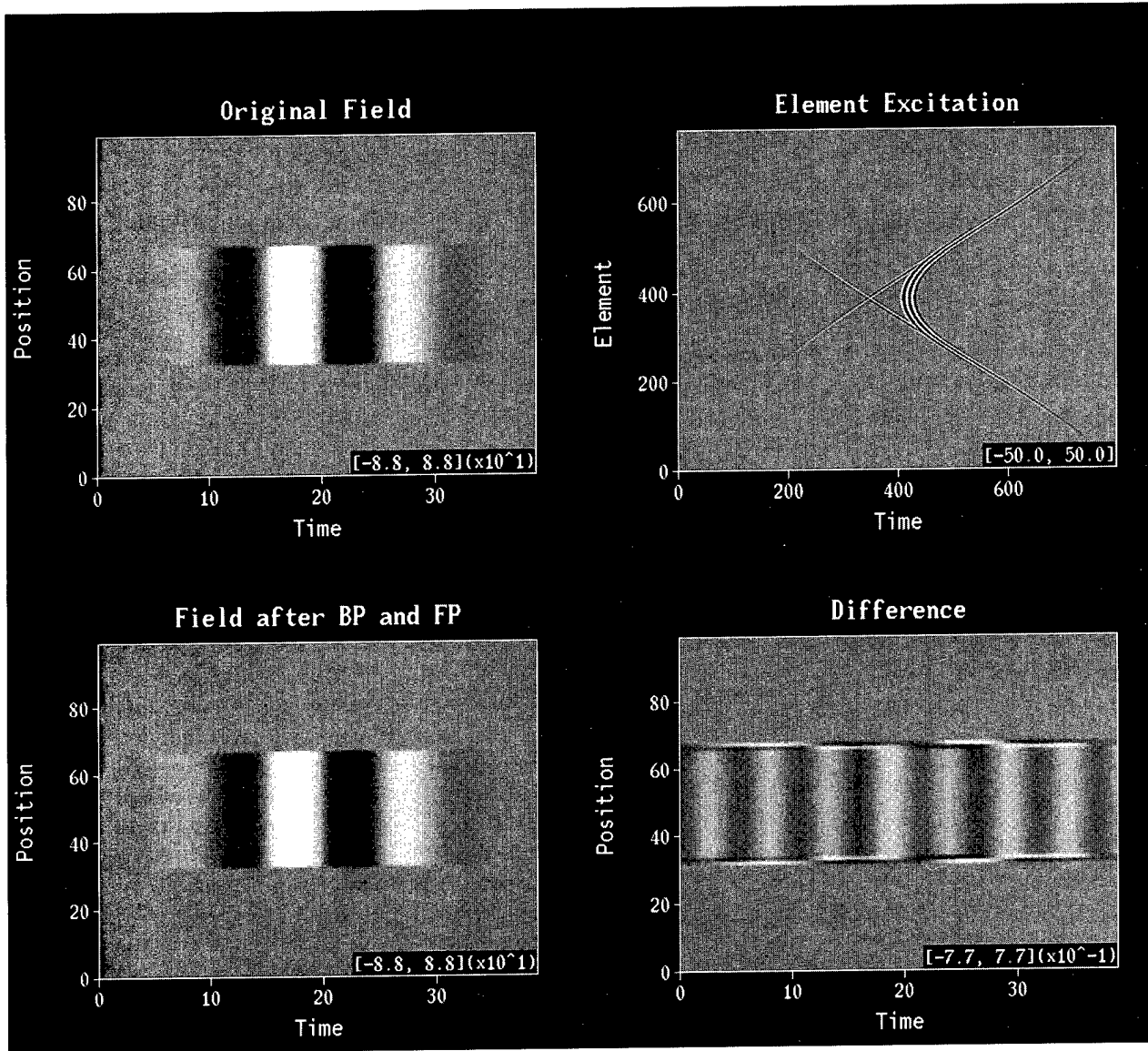
Fig. 6. Wavefront backpropagation applied to calculate ring transducer excitations for the production of a spatially limited plane wave. From left to right and top to bottom, respectively, are: the specified field, the calculated excitation signals, the field obtained by forward propagating the excitation wavefront, and the difference between the calculated and the specified field. In all the panels, horizontal axis is time sampled at 20 MHz. In the top-right panel, the vertical axis corresponds to element number and the display is in log scale with a 50 dB range for each polarity. In the other panels, the vertical axis corresponds to 100 spatial positions equally spaced along the ring diameter and the display is on a linear scale with gray being zero, white and black being positive and negative maximum amplitudes, respectively. The amplitude range is indicated in the lower right corner of each panel.

be obtained using (2). When $Z \to 0$, the above result approaches that for a pressure release surface, while when $Z \to \infty$, the above result approaches that for a rigid baffle surface.

In the particular case of $Z \to \infty$, $B(f_x, f_y)$ becomes $v_z(f_x, f_y)$, and (34) becomes

$$P(f_x, f_y, 0) = \frac{\rho c v_z(f_x, f_y)}{\sqrt{1 - \lambda^2(f_x^2 + f_y^2)}} \quad . \qquad (35)$$

This equation shows that a normal velocity boundary condition $v_z(x, y, 0)$ can be effectively transformed into a pressure boundary condition $p(x, y, 0)$. Multiplying (35) with $H(f_x, f_y, z)$ in (3), performing inverse Fourier transform

with respect to f_x and f_y, and using the angular spectrum of free-space Green's function in (6), yields

$$p(x, y, z) = -\frac{j\rho c}{\lambda} \int \int \frac{v_z(x_0, y_0, 0)e^{jkR}}{R} dx_0 dy_0 \quad , \qquad (36)$$

which is the well-known Rayleigh integral in the frequency domain.

C. Backpropagation, Phase Conjugation, and the Time-Reversal Mirror

The relationship between wave backpropagation, phase conjugation, and the so-called time-reversal mirror merits
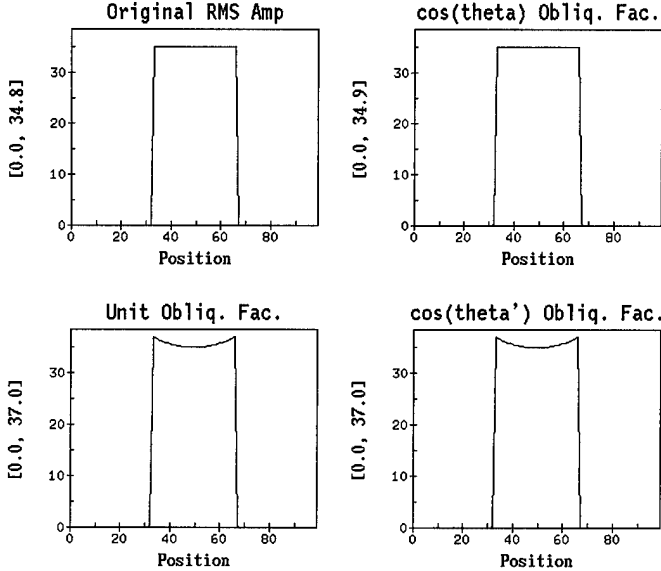
Fig. 7. Comparison of using correct and incorrect obliquity factors during forward propagation of excitation wavefront from the ring. From left to right and top to bottom, respectively, are: the specified field amplitude and the calculated field amplitudes using the correct obliquity factor $\cos\theta$ as defined in Fig. 2, using a unity obliquity factor, and using the obliquity factor $\cos\theta'$ also as defined in Fig. 2. The horizontal axis in these plots corresponds to 100 positions along the ring diameter.

comment, since these techniques are becoming more widely used and the analysis of wave propagation and backpropagation in this paper provides an opportunity to elucidate the similarity and dissimilarity of these techniques. For the purpose of discussion, assume a real pressure field $p(x, y, z, t)$ is given in an xy plane, and its temporal Fourier transform is denoted by $p_\omega(x, y, z)$. Because $p(x, y, z, t)$ is a real quantity, the result of phase conjugation $p_\omega^*(x, y, z)$ equals the Fourier transform of $p(x, y, z, -t)$. Therefore, aside from differences in implementation [17], phase conjugation and time-reversal differ only in that the former operates on a single frequency component whereas the latter is the time-domain representation of the same operation on all the frequency components. However, the time-domain approach has extra flexibility: the signal can be temporally windowed so that only a selected part of the signal is time-reversed. The application of phase conjugation or the time-reversal mirror usually consists of two stages. First a field is measured. Then the measurement is either phase conjugated or time-reversed and retransmitted. The retransmission involves a physical propagation in the medium so the medium must be present. In contrast, wave backpropagation is a computational process in which no physical propagation takes place, so the medium need not be present.

To examine further the relationship between backpropagation and phase conjugation (or the time-reversal mirror), consider a harmonic wavefront with complex amplitude $p(x, y, z)$ at a given z. The result of approximate backpropagation (in which evanescent waves decay instead of amplify with backpropagation) of $p(x, y, z)$ to the plane $z =$

0 can be computed using H^* given in (9). The result is

$$\tilde{P}_{\mathrm{BP}}(f_x, f_y, 0) = P(f_x, f_y, z)H^*(f_x, f_y, z) \ , \qquad (37)$$

where the subscript BP denotes backpropagation. On the other hand, the same wavefront may be phase conjugated and then retransmitted to produce a wave that propagates back to the plane at $z = 0$. In this case, although the physical propagation is in the $-z$ direction, the propagated homogeneous waves $(f_x^2 + f_y^2 \leq 1/\lambda^2)$ with a time dependence of $e^{-j\omega t}$ are advanced in phase to represent a time delay, and the amplitude of the propagated evanescent waves decay [18]. Therefore, the propagation function is exactly the same as $H(f_x, f_y, z)$ given by (3). Since the angular spectrum of the phase-conjugated wavefront $p^*(x, y, z)$ is

$$P_{\mathrm{PC}}(f_x, f_y, z) = \int \int p^*(x, y, z)e^{-j2\pi(xf_x + yf_y)}dxdy$$
$$= P^*(-f_x, -f_y, z) \ , \qquad (38)$$

where the subscript PC denotes phase conjugation, the result of propagating a phase-conjugated wavefront in the $-z$ direction is

$$P_{\mathrm{PC}}(f_x, f_y, 0) = P^*(-f_x, -f_y, z)H(f_x, f_y, z)$$
$$= [P(-f_x, -f_y, z)H^*(-f_x, -f_y, z)]^*$$
$$= \tilde{P}_{\mathrm{BP}}^*(-f_x, -f_y, 0) \ . \qquad (39)$$

Interpreted in the space domain, this result shows that

$$p_{\mathrm{PC}}(x, y, 0) = \tilde{p}_{\mathrm{BP}}^*(x, y, 0) \ , \qquad (40)$$

which, in turn, shows that the time-domain result of propagating a phase-conjugated wavefront is the time-reversal of the approximately backpropagated wavefront.

A wavefront $p(x, y, 0)$ that starts at plane $z = 0$, propagates to the plane at z and is measured there can, therefore, be fully recovered by backpropagation to $z = 0$ if exponential amplification of evanescent waves is performed during backpropagation. The backpropagated wavefront can have a resolution higher than that limited by $f_x^2 + f_y^2 < 1/\lambda^2$, as demonstrated in nearfield acoustic holography where measurements were used to reconstruct the field [19]. On the other hand, the $p(x, y, z)$ wavefront can be phase conjugated and retransmitted to propagate back to the plane $z = 0$. In the latter case, the wavefront resulting at $z = 0$ is approximately the time-reversal of the initial wavefront. The approximation results because the evanescent waves have decayed twice during this process: once from 0 to z and once from z to 0. Because of the decay, the field obtained by retransmission has a wavelength-limited resolution.

A matched filter model was employed in [17] to explain that a time-reversal mirror can be used to achieve a point focus by stating that the contribution from each element is maximized at the same instant of time at a certain field point. However, this statement applies to any field point within a distribution of random scatterers and does not explicitly identify the need for an isolated point target. The

need for a point target also limits the focus produced by time-reversal to be at the position of the point target, and no way apparently exists to steer the transmit beam effectively to other locations (which is essential for imaging purpose) unless the inhomogeneous medium is modelled such as by a phase screen placed some distance away from the aperture [20]. Another impression obtained from the matched-filter explanation is that the result of retransmission contains a temporal convolution of the form of $h_i(\vec{r}_0, T - t) * h_i(\vec{r}_0, t)$, where $h_i(\vec{r}_0, t)$ is the acoustic impulse response from field point $\vec{r}_0$ to transducer element i. See (9) of [17]. Therefore, pulses may become longer even if the acousto-electric impulse response of the elements $h_i^{ae}(t)$ is an ideal $\delta(t)$. The analysis presented above shows that this does not happen in a uniform medium if evanescent waves are ignored.

To summarize, backpropagation differs conceptually from phase conjugation/time-reversal mirror. Backpropagation is a computational process and can reconstruct a field with a resolution higher than that limited by wavelength, whereas phase conjugation/time-reversal mirror is a physical process and the retransmitted field always has a resolution that is wavelength limited. When applied for imaging through an inhomogeneous medium, backpropagation assumes knowledge or requires a model of the medium, and can be applied for beam steering and imaging, whereas phase conjugation or time reversal requires that the medium be present and that an isolated point target exist to form a focus only at that point.

V. CONCLUSION

The computation of wave propagation and backpropagation in a three-dimensional or a two-dimensional uniform medium has been considered. Three methods, *i.e.*, the angular spectrum method, the diffraction integral method, and the shift-and-add method, have been examined and their relationships explored. The straightforward application of the angular spectrum method was shown to correspond to Dirichlet boundary condition. The shift-and-add method was shown to require a temporal differentiation of the signal as well as amplitude scaling and multiplication with an obliquity factor in order for the results to be the same as obtained with the other two methods. By replacing the exponential amplification of evanescent waves during backpropagation with an exponential decay, results were obtained for backpropagation using the diffraction integral method and the shift-and-add method in addition to the angular spectrum method. Wave propagation in two-dimensional space was shown to differ in several aspects from three-dimensional wave propagation. In particular, no corresponding formula for shift-and-add method exists in the two-dimensional case. The diffraction integral method for two-dimensional propagation has been extended to apertures of arbitrary shape by changing the obliquity factor according to the geometry. This extension is based on the assumption that the aperture is smooth

and that the contribution of each element on the aperture surface to a field point is little influenced by the overall shape of the aperture. Computations have been used to illustrate the above results.
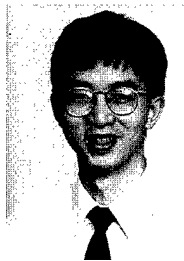
REFERENCES

[1] A. D. Pierce, *Acoustics: An Introduction to Its Physical Principles and Applications.* New York: McGraw-Hill, 1981, Ch. 4, Ch. 5.
[2] J. W. Goodman, *Introduction to Fourier Optics.* New York: McGraw-Hill, 1968, Ch. 3.
[3] R. C. Waag, J. A. Campbell, J. Ridder, and P. R. Mesdag, "Cross-Sectional Measurements and extrapolations of ultrasonic fields," *IEEE Trans. Sonics and Ultras.*, vol. SU-32, no. 1, pp. 26–35, 1985.
[4] Ultrasonic beamforming is usually based on shift-and-add (also known as delay-and-sum). See, for example, O. T. von Ramm and S. W. Smith, "Beam steering with linear arrays," *IEEE Trans. Biomed. Engnr.*, vol. BME-30, no. 8, pp. 438–452, 1983. Direct discretization of the Rayleigh integral also leads to shift-and-add. See, for example, J. Zemanek, "Beam behaviour within the nearfield of a vibrating piston," *J. Acoust. Soc. Am.*, vol. 49, pp. 181–191, 1971.
[5] D. H. Turnbull and F. S. Foster, "Beam steering with pulsed two-dimensional transducer array," *IEEE Trans. Ultrason., Ferroelect., Freq. Contr.*, vol. 38, no. 4, pp. 320–333, 1991.
[6] D. P. Orofino and P. C. Pedersen, "Efficient angular spectrum decomposition of acoustic sources — Part I: Theory," *IEEE Trans. Ultrason., Ferroelect., Freq. Contr.*, vol. 40, no. 3, pp. 238–249, 1993.
[7] P. R. Stepanishen, "The time-dependent force and radiation impedance on a piston in a rigid infinite planar baffle," *J. Acoust. Soc. Am.*, vol. 49, no. 3, pp. 841–849, 1971.
[8] P. R. Stepanishen, "The relationship between the impulse response and angular spectrum methods to evaluate acoustic transient fields," *J. Acoust. Soc. Am.*, vol. 90, no. 5, pp. 2794–2798, 1991.
[9] B. Delannoy, H. Lasota, C. Bruneel, R. Torguet, and E. Bridoux, "The infinite planar baffles problem in acoustic radiation and its experimental verification," *J. Appl. Phys.*, vol. 50, no. 8, pp. 5189–5195, 1979.
[10] A. R. Selfridge, G. S. Kino, and B. T. Khuri-Yakub, "A theory for the radiation pattern of a narrow-strip acoustic transducer," *Appl. Phys. Lett.*, vol. 37, no. 1, pp. 35–36, 1980.
[11] P. M. Morse and K. U. Ingard, *Theoretical Acoustics.* New York: McGraw-Hill, 1968, Ch. 7.
[12] J. R. Shewell and E. Wolf, "Inverse diffraction and a new reciprocity theorem," *J. Opt. Soc. Am.*, vol. 58, no. 12, pp. 1596–1603, 1968.
[13] E. Lalor, "Inverse wave propagator," *J. Math. Phy.*, vol. 9, no. 12, pp. 2001–2006, 1968.
[14] User's Manual, *Math/Library Special Functions, ver. 2*, Houston: IMSL, 1991, Ch. 6.
[15] A. Penttinen and M. Luukkala, "The impulse response and pressure nearfield of a curved ultrasonic radiator," *J. Phys. D. Appl. Phys.*, vol. 9, pp. 1547–1557, 1976.
[16] J. F. Clarebout, *Fundamentals of Geophysical Data Processing.* New York: McGraw-Hill, 1976, Ch. 10.

[17] M. Fink, "Time reversal of ultrasonic fields — Part I: Basic principles," *IEEE Trans. Ultrason., Ferroelect., Freq. Contr.*, vol. 39, no. 5, pp. 555–566, 1992.

[18] M. Nieto-Vesperinas and E. Wolf, "Phase conjugation and symmetries with wave fields in free space containing evanescent components," *J. Opt. Soc. Am.*, vol. 2, no. 9, pp. 1429–1434, 1985.

[19] J. D. Maynard, E. G. Williams, and Y. Lee, "Nearfield acoustic holography: I. Theory of generalized holography and the development of NAH," *J. Acoust. Soc. Am.*, vol. 78, no. 4, pp. 1395–1413, 1985.

[20] D.-L. Liu and R. C. Waag, "Correction of ultrasonic wavefront distortion using backpropagation and a reference waveform method for time-shift compensation," *J. Acoust. Soc. Am.*, vol. 96, no. 2, pp. 649–659, 1994.

Robert C. Waag (S'59–M'66–SM'83–F'90) received his B.E.E., M.S., and Ph.D. degrees from Cornell University in 1961, 1963, and 1965, respectively. After completing his Ph.D. studies, he became a member of the technical staff at the Sandia Laboratories, Albuquerque, NM and then served as an officer in the United States Air Force from 1966 to 1969 at the Rome Air Development Center, Griffiss Air Force Base, NY. In 1969, he joined the faculty at the University of Rochester where he is now Arthur Gould Yates Professor in the Department of Electrical Engineering, School of Engineering and Applied Science and holds an appointment in the Department of Radiology, School of Medicine and Dentistry. Professor Waag's recent research has treated ultrasonic scattering and propagation problems in medical imaging and other applications. Professor Waag is a fellow of the Institute of Electrical and Electronics Engineers, the Acoustical Society of America, and the American Institute of Ultrasound in Medicine.

Dong-Lai Liu (M'93) obtained his Bachelor of Engineering degree in 1984 from the Department of Automatic Control, Qinghua University, Beijing, China and Master of Engineering degree (1988) and Doctor of Engineering (1991) from the Department of Electronic Engineering, University of Tokyo. He was Assistant Professor in the Department of Electrical and Electronic Engineering at Sophia University, Tokyo, Japan, during April 1991 to March 1992. Since April 1992 he has been with the Department of Electrical Engineering at University of Rochester, Rochester, New York, where his current appointment is Scientist and Assistant Professor. Dr. Liu's research interests include analysis and modeling of ultrasonic wavefront distortion, adaptive beamforming with aberration correction, quantitative ultrasonic imaging, spectral analysis, and digital signal processing. He is a member of the Institute of Electrical and Electronics Engineers and the Acoustical Society of America.

Focusing and imaging using eigenfunctions of the scattering operator

T. Douglas Mast[a)]
Department of Electrical Engineering, University of Rochester, Rochester, New York 14642

Adrian I. Nachman
Department of Mathematics, University of Rochester, Rochester, New York 14627

Robert C. Waag
Departments of Electrical Engineering and Radiology, University of Rochester, Rochester, New York 14627

An inverse scattering method that uses eigenfunctions of the scattering operator is presented. This approach provides a unified framework that encompasses eigenfunction methods of focusing and quantitative image reconstruction in arbitrary media. Scattered acoustic fields are described using a compact, normal operator. The eigenfunctions of this operator are shown to correspond to the far-field patterns of source distributions that are directly proportional to the position-dependent contrast of a scattering object. Conversely, the eigenfunctions of the scattering operator specify incident-wave patterns that focus on these effective source distributions. These focusing properties are employed in a new inverse scattering method that represents unknown scattering media using products of numerically calculated fields of eigenfunctions. A regularized solution to the nonlinear inverse scattering problem is shown to result from combinations of these products, so that the products comprise a natural basis for efficient and accurate reconstructions of unknown inhomogeneities. The corresponding linearized problem is solved analytically, resulting in a simple formula for the low-pass-filtered scattering potential. The linear formula is analytically equivalent to known filtered-backpropagation formulas for Born inversion, and, at least in the case of small scattering objects, has advantages of computational simplicity and efficiency. A similarly efficient and simple formula is derived for the nonlinear problem in which the total acoustic pressure can be determined based on an estimate of the medium. Computational results illustrate focusing of eigenfunctions on discrete and distributed scattering media, quantitative imaging of inhomogeneous media using products of retransmitted eigenfunctions, inverse scattering in an inhomogeneous background medium, and reconstructions for data corrupted by noise. © *1997 Acoustical Society of America.* [S0001-4966(97)02308-4]

INTRODUCTION

This paper presents a new inverse scattering method that employs the focusing properties of certain acoustic fields obtained by retransmitting eigenfunctions of the scattering operator.

Eigensystem decomposition of the scattering operator, regardless of the inversion method employed, has potential advantages in methods of collecting and analyzing scattering data. Previous work in electrical impedance tomography has employed eigenfunction decomposition of an operator associated with the measurement process to determine optimal input current patterns and quantify the achievable resolution of imaging systems.[1,2] These optimal inputs can also be determined by iteratively retransmitting input patterns that are proportional to the measured scattered field. This approach is essentially an analog implementation of the "power method" for determining the eigenvectors of matrices.[2,3]

Likewise, the techniques of optical and acoustic phase conjugation[4–7] and the analogous process of time reversal[8,9]

can be understood as analog methods of computing the eigenfunctions of an operator associated with the phase conjugation or time-reversal process. Simple focusing by phase conjugation, in which received echoes are conjugated or time reversed and retransmitted, is equivalent to a single iteration of the power method. Further iterations of this procedure correspond to additional steps in the power method, and thus converge to the most significant eigenfunction of the associated operator at a rate specified by the ratio of the two largest eigenvalues.[3] The eigenfunctions of the "time-reversal operator," whether obtained by iterative time reversal or by numerical diagonalization, have been previously shown to correspond to source distributions that can focus incident energy on strong, pointlike scatterers.[10,11]

Eigensystem analysis has historically played a role in the theory of inverse scattering for radially symmetric objects.[12] For these objects, separation of variables naturally leads to a representation of the scattering operator in terms of trigonometric functions. Since these eigenfunctions are the same for any radial scatterer, the inverse scattering problem could be reduced to the problem of determining the unknown object from the eigenvalues of the scattering operator.

[a)]Current affiliation: Applied Research Laboratory, The Pennsylvania State University, P.O.B. 30, State College, PA 16802.

However, before the method presented here, the focusing properties of eigenfunctions have not been exploited for quantitative reconstruction of inhomogeneous media. It is stated in Ref. 9 that the concept of time reversal "cannot be directly compared to computed tomography" or to "techniques that generate the image of the medium through signal analysis." Although the basic principles of focusing on point targets using the eigenfunctions of scattering operators have been put forth in Ref. 10, these principles have not previously been shown to apply to general distributed inhomogeneities. Furthermore, no general imaging method has hitherto been based on these principles.

The current method presents a solution to the imaging problem by bringing together recent results in the theory of focusing, diffraction tomography, and inverse problems to synthesize a unified framework for quantitative imaging of inhomogeneous media. Application of the method shows that focusing on distributed inhomogeneities can be achieved using eigenfunctions and also provides a technique for quantitative imaging of discrete and distributed inhomogeneities using focusing properties.

This method has several advantages over current inverse scattering methods. First, the eigenfunction formulation provides optimal bases for reconstruction of unknown media, so that inversions are performed with the minimum possible complexity. Second, the method is applicable to any scattering medium for which the total acoustic pressure associated with an incident plane wave can be estimated. Inverse scattering in inhomogeneous background media as well as iterative nonlinear inverse scattering can therefore be directly implemented. Third, part of the computation necessary for the inverse scattering algorithm can be performed by analog means using ideas from the power method.

The present approach also provides new understanding about existing methods of focusing and imaging. For simple scattering objects, the new method presented here reduces to a quantitative specification of focusing similar to that obtained by iterative phase conjugation or time reversal. The eigenfunctions of scattering operators are shown not only to focus on pointlike scatterers, as has been previously shown,[10,11] but also to concentrate incident energy in the vicinity of general, distributed inhomogeneities. The method also improves on previous approaches to focusing using eigenfunctions in that quantitative images of medium parameters are obtained simultaneously with optimal incident-wave distributions. For the case of weakly scattering objects, the method reduces to a simple inversion algorithm that is mathematically equivalent to the filtered backpropagation algorithm,[13–15] but is optimally tailored to the unknown scattering medium. The method reduces to a comparably simple and efficient formula for the case of weakly nonlinear inverse scattering.

Analysis given in Sec. I shows that eigenfunctions of scattering operators are equal to the acoustic fields of effective source distributions that are proportional to the compressibility contrast of the scattering object. An inverse scattering method that incorporates products of retransmitted fields of eigenfunctions is presented. The general method is then employed to derive an analytic inversion formula valid
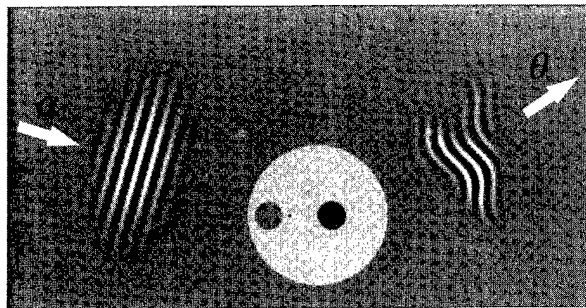

FIG. 1. Scattering configuration. An incident plane wave traveling in the direction α is scattered by an inhomogeneity and the scattered field is measured in the direction θ.

under the Born approximation as well as a simple nonlinear formula valid for small multiple-scattering effects. Numerical implementation of these methods is presented in Sec. II. Numerical results shown in Sec. III illustrate focusing on discrete and distributed inhomogeneities using a few eigenfunctions. Also, quantitative inverse scattering results are shown both within the context of a homogeneous background medium and an inhomogeneous background medium.

I. THEORY

A. Background

An inverse scattering method for a medium of variable sound speed is derived. For simplicity of exposition, the derivation is given for the canonical two-dimensional scattering configuration sketched in Fig. 1. However, with minor modifications, the method is applicable to arbitrary geometries and dimensions.

When the incident pressure is a plane wave of unit amplitude propagating in the direction α, so that $p_i(\mathbf{x}) = e^{ik\alpha \cdot \mathbf{x}}$, the corresponding total acoustic pressure $p(\mathbf{x}, \alpha)$ at the position $\mathbf{x}$ is given by the Lippman–Schwinger equation[16,17]

$$p(\mathbf{x}, \alpha) = e^{ik\alpha \cdot \mathbf{x}} - \int G_0(\mathbf{x} - \mathbf{y}, k) q(\mathbf{y}) p(\mathbf{y}, \alpha) dy, \quad (1)$$

where $G_0(\mathbf{x} - \mathbf{y})$ is the Green's function for the Helmholtz equation in a homogeneous medium. In an unbounded two-dimensional medium, $G_0(\mathbf{x} - \mathbf{y})$ is given by the Hankel function $(i/4)H_0^{(1)}(k|\mathbf{x} - \mathbf{y}|)$.[18] The angle α is defined as the angle corresponding to the direction unit vector α, the wave number k is equal to $2\pi f/c_0$ where c_0 is the wave speed of the background medium, and f is the temporal frequency of the incident wave. The integral appearing in Eq. (1), as well as subsequent integrals in x and y, are understood to be taken over the entire plane in $\mathbb{R}^2$. The scattering potential q is given for a medium of variable sound speed by

$$q(\mathbf{x}) = -k^2 \left(\frac{c_0^2}{c^2(\mathbf{x})} - 1 \right). \quad (2)$$

The quantity within parentheses is equal, for a medium of constant density, to the compressibility contrast γ_κ, as defined in Ref. 17. The scattering potential is assumed to be

real-valued and to be short-range, that is, the potential q decreases at large distances such that

$$|q(\mathbf{x})| \leq C(1+|\mathbf{x}|)^{-1-\delta}, \tag{3}$$

where $|\mathbf{x}|$ is the magnitude of the position vector $\mathbf{x}$, for some $\delta > 0$.

At a measurement radius r in the far field and a measurement angle θ, the scattered pressure, $p_s = p - p_i$, is of the form

$$p_s(r,\theta,\alpha) = -\sqrt{\frac{i}{8\pi}} \frac{e^{ikr}}{\sqrt{kr}} A(\theta,\alpha) + o\left(\frac{1}{\sqrt{kr}}\right), \tag{4}$$

where A is the far-field pattern of the scattered pressure

$$A(\theta,\alpha) = \int e^{-ik\theta \cdot \mathbf{x}} q(\mathbf{x}) p(\mathbf{x},\alpha) dx. \tag{5}$$

The incident pressure may be more generally taken as a superposition of plane waves propagating in all directions,

$$p_i(\mathbf{x}) = \int f(\alpha) e^{ik\alpha \cdot \mathbf{x}} d\alpha. \tag{6}$$

The far-field pattern of the corresponding scattered acoustic pressure is then

$$Af(\theta) = \int A(\theta,\alpha) f(\alpha) d\alpha. \tag{7}$$

Equation (7) defines an operator A that maps an incident-wave distribution $f(\theta)$ into the corresponding far-field scattered pressure $Af(\theta)$. The operator A is related to the usual scattering operator S (Ref. 19) by

$$S = I - \frac{i}{4\pi} A, \tag{8}$$

where I is the identity operator.

The operator A is compact[19] and therefore has a countable number of discrete eigenvalues with zero as the only possible cluster point. In practice, only a finite number of eigenvalues are distinguishable from zero. Since the potential q is real-valued, the scattering operator is unitary, so that the eigenvalues of A lie in the complex plane on the circle centered at $-4\pi i$ and passing through the origin. It also follows that A is normal ($A^*A = AA^*$, where A^* is the Hermitian transpose of A), so that an orthonormal basis $\{f_i\}$ for $L^2[0,2\pi]$ exists consisting of eigenfunctions of A.

Since A is a normal operator, the Hermitian transpose A^* satisfies the relation $A^* f_i = \lambda^* f_i$, where f_i is an eigenfunction of A and λ_i^* is the complex conjugate of λ_i. The eigenfunctions of A therefore also satisfy the equation

$$A^*A f_i = |\lambda_i|^2 f_i. \tag{9}$$

Thus the functions f_i also constitute a basis of eigenfunctions for A^*A and the corresponding eigenvalues are the squared magnitudes of the eigenvalues of A. The operator A^*A is essentially a far-field analog of the "time-reversal operator" as defined in Ref. 10.

B. Focusing properties

The focusing properties of A are seen by considering the ratio of the scattered amplitude to the incident amplitude. Since A is normal, the magnitude of its largest eigenvalue is equal to the largest possible value of this ratio for any non-zero f:

$$|\lambda_1| = \sup\left[\frac{\|Af(\theta)\|_{L^2}}{\|f(\theta)\|_{L^2}}\right], \tag{10}$$

where $\sup(\cdot)$ denotes the least upper bound and $\|f(\cdot)\|_{L^2}$ denotes the root-mean-square magnitude of a square-integrable function. Thus the eigenfunction associated with the largest eigenvalue of A specifies an incident-wave distribution that maximizes the energy scattered to the far field. Other eigenfunctions also focus energy on inhomogeneities with an efficiency that is quantified by the associated eigenvalues.

The focusing property of eigenfunctions of A is further illustrated by introducing the acoustic fields of incident-wave distributions specified by the eigenfunctions. One may define retransmitted fields of an incident-wave distribution $f(\alpha)$ as

$$E(\mathbf{x}) = \int f(\alpha) e^{ik\alpha \cdot \mathbf{x}} d\alpha,$$

$$F(\mathbf{x}) = \int f(\alpha) p(\mathbf{x},\alpha) d\alpha, \tag{11}$$

where $E(\mathbf{x})$ is the retransmitted field associated with the incident-wave distribution in a homogeneous medium and $F(\mathbf{x})$ is the retransmitted field in a medium containing the inhomogeneity $q(\mathbf{x})$.

For incident-wave patterns corresponding to eigenfunctions that have nonzero eigenvalues, the retransmitted fields of Eqs. (11) can be written using Eqs. (5) and (7) in the form

$$E_i(\mathbf{x}) = \frac{2\pi}{\lambda_i} \int J_0(k|\mathbf{x}-\mathbf{y}|) F_i(\mathbf{y}) q(\mathbf{y}) dy,$$

$$F_i(\mathbf{x}) = \frac{1}{\lambda_i} \int \langle p(\mathbf{x},\theta), e^{ik\theta \cdot \mathbf{y}} \rangle F_i(\mathbf{y}) q(\mathbf{y}) dy. \tag{12}$$

The brackets in Eq. (12) denote the inner product

$$\langle u,v \rangle = \int_0^{2\pi} u(\theta) v^*(\theta) d\theta, \tag{13}$$

while the inner product appearing in the expression for E_i was evaluated using the identity

$$J_0(z) = \frac{1}{2\pi} \int e^{iz \cos\theta} d\theta \tag{14}$$

known as Parseval's integral.[20] The retransmitted fields of Eq. (11) are thus seen to be equivalent to a weighted convolution of the unknown scattering potential with inner products of acoustic fields.

When the scattering potential $q(\mathbf{x})$ is concentrated in a finite number of pointlike scatterers, each very small compared to a wavelength, Eq. (12) reduces to an expression of diffraction-limited focusing on each point scatterer. That is, for a scattering medium defined by

$$q(\mathbf{x}) = \sum_1^M \mu_j \delta(\mathbf{x} - \mathbf{x_j}), \tag{15}$$

the retransmitted field $E_i(\mathbf{x})$ is

$$E_i(\mathbf{x}) = \frac{2\pi}{\lambda_i} \sum_j F_i(\mathbf{x}_j) J_0(k|\mathbf{x} - \mathbf{x_j}|) \mu_j, \tag{16}$$

so that in this case, the retransmitted field $E_i(\mathbf{x})$ is equal to a weighted sum of Bessel functions, each centered at the location of one of the point scatterers. These Bessel functions correspond to a group of diffraction-limited main lobes, centered at each scatterer position $\mathbf{x_j}$, with corresponding Bessel sidelobes that combine coherently. Thus each retransmitted field E_i focuses to some extent on all of the individual point scatterers.

The close relationship between the retransmitted fields of eigenfunctions and the unknown scattering potential, as seen in Eq. (12), is an expression of the focusing property of eigenfunctions. That is, since eigenfunctions of A correspond to incident-wave patterns that concentrate energy within the support of the scattering potential, they can be said to focus on general distributed inhomogeneities as well as pointlike scatterers. This idea is illustrated numerically later in this paper.

C. Inverse scattering method

Because of the focusing properties outlined above, retransmitted fields of eigenfunctions are a useful starting point for inverse scattering reconstructions. A general inverse scattering method incorporating these ideas is outlined below.

The starting point for this method is an expression of the inverse scattering problem in terms of the operator A of Eq. (7) and the corresponding retransmitted fields defined in Eq. (11):

$$\langle Af_i, f_j \rangle = \delta_{ij}\lambda_i = \int F_i(\mathbf{x}) E_j^*(\mathbf{x}) q(\mathbf{x}) dx,$$

$$i, j = 1, 2, \ldots . \tag{17}$$

The problem can be regularized by seeking the solution that minimizes the weighted L^2 norm

$$\|q\|_W^2 = \int |q(\mathbf{x})|^2 W(\mathbf{x}) dx \tag{18}$$

with $W(\mathbf{x})$ an appropriate weight. For the analysis given below, this weight is defined as $W(\mathbf{x}) = (1 + |\mathbf{x}|)^\delta, \delta > 0$. For the explicit computations given later, other choices of $W(\mathbf{x})$ are more natural.

A solution to the minimization problem is obtained using the method of Lagrange multipliers, analogous to the approach used in Ref. 21 for a linearized electric impedance tomography problem. At a minimum, the (infinite-dimensional) gradient of $\|q\|_W^2$ is a linear combination of the gradients of the constraints in Eq. (17). The latter can be calculated using the two-potential formula[16]

$$A_{q_1}(\theta, \alpha) - A_{q_2}(\theta, \alpha) = \int p_1(\mathbf{x}, \alpha)$$

$$\times (q_1(\mathbf{x}) - q_2(\mathbf{x})) p_2(\mathbf{x}, \theta + \pi) dx, \tag{19}$$

where A_{q_1}, p_1, A_{q_2}, and p_2 are the scattering operators and the total acoustic pressures for the inhomogeneous media defined by $q_1(\mathbf{x})$ and $q_2(\mathbf{x})$, respectively. Equation (19) yields the derivative

$$\lim_{\epsilon \to 0} \frac{A_{q + \epsilon \tilde{q}}(\theta, \alpha) - A_q(\theta, \alpha)}{\epsilon} = \int p(\mathbf{x}, \alpha) \tilde{q}(\mathbf{x}) p(\mathbf{x}, \theta + \pi) dx, \tag{20}$$

while the infinite-dimensional gradient of $\|q\|_W^2$ is found from

$$\lim_{\epsilon \to 0} \frac{\|q + \epsilon \tilde{q}\|_W^2 - \|q\|_W^2}{\epsilon} = 2 \int q(\mathbf{x}) \tilde{q}(\mathbf{x}) W(\mathbf{x}) dx. \tag{21}$$

The result follows that if the potential $q_M(\mathbf{x})$ solves the regularized inverse scattering problem [minimization of the weighted norm from Eq. (18) under the constraint of Eq. (17)], q_M must be of the form

$$q_M(\mathbf{x}) = \frac{1}{W(\mathbf{x})} \sum_l \sum_m Q_{lm} F_l(\mathbf{x}) \bar{F}_m^*(\mathbf{x}), \tag{22}$$

where $\bar{F}_m^*(\mathbf{x})$, the complex conjugate of the retransmitted field corresponding to an incoming condition at infinity, is defined as

$$\bar{F}^*(\mathbf{x}) = \int f^*(\alpha) p(\mathbf{x}, \alpha + \pi) d\alpha, \tag{23}$$

and the coefficients Q_{lm} are the Lagrange multipliers. If the above gradients are taken with respect to the real and imaginary parts of a complex potential, Eq. (22) as stated is also found to be valid when the potential q_M is complex. In some of the simplifying approximations made below, Eq. (22) will yield a complex potential q_M even when the data are assumed to come from a unitary scattering operator associated with the real potential q.

By substituting Eq. (22) into Eq. (17), the inverse problem is reduced to the problem of finding the coefficients Q_{lm} from the nonlinear system

$$\delta_{ij}\lambda_i = \sum_l \sum_m \left[\int \frac{F_i(\mathbf{x}) E_j^*(\mathbf{x}) F_l(\mathbf{x}) \bar{F}_m^*(\mathbf{x})}{W(\mathbf{x})} dx \right] Q_{lm},$$

$$i, j = 1, 2, \ldots , \tag{24}$$

where the dependence of the fields F and $\bar{F}^*$ on the scattering potential q is implicit.

In general, the scattering potential $q(\mathbf{x})$, and therefore the total pressure field $p(\mathbf{x}, \alpha)$, are unknown in inverse scattering problems. The function $p(\mathbf{x}, \alpha)$ that implicitly appears in Eq. (24) may therefore be replaced by the best available estimate for the total pressure. Equation (24) can then be solved for the coefficients Q_{lm} by standard numerical techniques for solution of linear systems.

The number of terms N can be chosen arbitrarily; however, increasing N beyond the number of nonzero eigenval-

ues of A is of limited benefit in reconstructions. For simple scattering objects, q can be represented by expansions employing small values of N. For instance, for an inhomogeneity consisting of finitely many point scatterers, N comparable to the number of scatterers is sufficient.

The above method simplifies further in the case of a weakly scattering medium, for which the total pressure p can be approximated by the incident pressure. In this case, taking the weight $W(\mathbf{x}) \equiv 1$, the coefficients Q_{lm} can be evaluated analytically. From Eq. (22), under the Born approximation, the scattering potential takes the form

$$q_B(\mathbf{x}) = \sum_l \sum_m Q_{lm} E_l(\mathbf{x}) E_m^*(\mathbf{x}). \tag{25}$$

Substituting Eq. (25) into Eq. (5) gives the equation

$$A(\theta, \alpha) = \sum_l \sum_m Q_{lm} \int e^{-ik\theta \cdot \mathbf{x}} E_l(\mathbf{x}) E_m^*(\mathbf{x}) p(x, \alpha) dx. \tag{26}$$

Replacement of $p(\mathbf{x}, \alpha)$ in Eq. (26) by the incident plane wave $e^{ik\alpha \cdot \mathbf{x}}$, use of Eq. (11), and integration in $\mathbf{x}$ over $\mathbb{R}^2$ yields

$$A(\theta, \alpha) = \frac{(2\pi)^2}{k^2} \sum_l \sum_m Q_{lm} \int_{-\pi}^{\pi} \int_{-\pi}^{\pi} \delta(\theta - \alpha - \theta' + \alpha')$$
$$\times f_l(\theta') f_m^*(\alpha') d\theta' d\alpha' \tag{27}$$

for $\theta - \alpha$ not equal to 0 or π. The double integral in Eq. (27) can be evaluated using the change of variables

$$x_1' = \cos \theta' - \cos \alpha', \quad x_2' = \sin \theta' - \sin \alpha', \tag{28}$$

which is one-to-one when restricted to the regions $\alpha' < \theta'$ and $\alpha' > \theta'$. Evaluation of the integral yields

$$|\sin(\theta - \alpha)| A(\theta, \alpha) = \frac{(2\pi)^2}{k^2} \sum_l \sum_m Q_{lm} (f_l(\theta) f_m^*(\alpha)$$
$$+ f_l(\alpha + \pi) f_m^*(\theta + \pi)). \tag{29}$$

Equation (29) can be solved for the coefficients Q_{lm} using the fact that the eigenfunctions $f_l(\theta)$ are orthonormal as well as the reciprocity identity[16]

$$A(\theta + \pi, \alpha + \pi) = A(\alpha, \theta). \tag{30}$$

The solution is

$$Q_{lm} = \frac{k^2}{8\pi^2} \int \int |\sin(\theta - \alpha)| A(\theta, \alpha) f_l^*(\theta) f_m(\alpha) d\alpha \, d\theta. \tag{31}$$

Equations (25) and (31) specify a solution q_B to the linearized inverse problem. This solution is, in general, complex, even when the true potential q is purely real. A physical way to understand why the Born approximation yields a complex scattering potential for a lossless medium is to recognize that this approximation neglects multiple scattering and thus, the resulting output energy differs from the input energy. The corresponding scattering operator is then no longer unitary, and is only physically realizable by a potential with a nonzero imaginary part. For weak scattering, the

energy discrepancy is small and so is the imaginary part of the potential.

The analytic solution of Eqs. (25) and (31) is equivalent to the well-known filtered backpropagation formula[13-15] and has the advantage of computational simplicity, as discussed later in this paper. Equivalence between the two formulas is shown by formulating an expansion of $e^{-ik\alpha \cdot \mathbf{x}}$, viewed as a function of α, in terms of the orthonormal basis $\{f_m(\alpha)\}$. In view of Eqs. (11), this expansion yields the identity

$$e^{-ik\alpha \cdot \mathbf{x}} = \sum_m E_m^*(\mathbf{x}) f_m(\alpha). \tag{32}$$

Substituting Eq. (31) in Eq. (25) and using Eq. (32) as well as its conjugate gives

$$q_B(\mathbf{x}) = \frac{k^2}{8\pi^2} \int \int |\sin(\alpha - \theta)| A(\theta, \alpha) e^{ik\mathbf{x} \cdot (\theta - \alpha)} d\alpha \, d\theta, \tag{33}$$

which is the standard filtered backpropagation formula. Equation (33) yields the low-pass-filtered version of the true potential q if multiple scattering effects are negligible. The correct nonlinear generalization of the linearized low-pass filtered solution q_B is the minimal L^2 (or weighted L^2) solution q_M, which is of a form specified by Eq. (22).

The inverse scattering method developed above can also be used with any orthonormal set of basis functions for $L^2[0, 2\pi]$. For instance, reconstructions can be performed using eigenfunctions of A for axisymmetric objects rather than using the eigenfunctions associated with the measured A. In this case, the eigenfunctions take the form

$$f_m(\theta) = \frac{1}{\sqrt{2\pi}} e^{im\theta}, \quad m = 0, \pm 1, \pm 2, \ldots . \tag{34}$$

The retransmitted fields E_m can be analytically evaluated to be

$$E_m(r, \phi) = \sqrt{2\pi} i^m e^{im\phi} J_m(kr), \tag{35}$$

and the coefficients Q_{lm} for the low-pass-filtered reconstruction of q are given by

$$Q_{lm} = \frac{k^2}{16\pi^3} \int \int |\sin(\theta - \alpha)| A(\theta, \alpha) e^{-il\theta} e^{im\alpha} d\alpha \, d\theta. \tag{36}$$

While the retransmitted fields specified by Eq. (35) are not ideally matched to nonaxisymmetric scattering media, they can be analytically evaluated and stored for use in fast reconstructions. Since these retransmitted fields are also unaffected by uncertainties in scattering measurements, they are suitable for reconstructions from data corrupted by noise.

Finally, use of the eigenfunction method beyond linear inversion is demonstrated by considering the case where the inhomogeneous-medium retransmitted fields F can be estimated from a first approximation to the scattering potential q. One approach in this case is to solve the full system of equations defined by Eq. (24); however, a more numerically efficient correction to the Born approximation can be obtained by invoking the localized nonlinear approximation introduced in Ref. 22 for electromagnetic scattering. This approximation follows from writing the Lippman–Schwinger equation [Eq. (1)] in the form

$$p(\mathbf{x},\alpha)=\Gamma(\mathbf{x})\left(e^{ik\alpha\cdot\mathbf{x}}-\int (p(\mathbf{y},\alpha)-p(\mathbf{x},\alpha))\right.$$

$$\left.\times q(\mathbf{y})G_0(\mathbf{x}-\mathbf{y})dy\right),\tag{37}$$

where the quantity $\Gamma(\mathbf{x})$, called the depolarization tensor in electromagnetic scattering,[22] is defined by

$$\Gamma(\mathbf{x})=\left(1+\int q(\mathbf{y})G_0(\mathbf{x}-\mathbf{y})dy\right)^{-1}.\tag{38}$$

The second term in Eq. (37) is presumed to be small because the singularity of the Green's function is cancelled by the difference term appearing in the integrand. Thus the total pressure may be approximated by the formula

$$p(\mathbf{x},\alpha)\approx\Gamma(\mathbf{x})e^{ik\alpha\cdot\mathbf{x}}.\tag{39}$$

The form for the scattering potential given by Eq. (22) then becomes

$$q_M(\mathbf{x})\approx\frac{\Gamma(\mathbf{x})^2}{W(\mathbf{x})}\sum_l\sum_m Q_{lm}E_l(\mathbf{x})E_m^*(\mathbf{x}).\tag{40}$$

Substituting this form into Eq. (5) and using Eq. (39) gives

$$A(\theta,\alpha)\approx\sum_l\sum_m Q_{lm}\int e^{-ik\theta\cdot\mathbf{x}}W(\mathbf{x})^{-1}E_l(\mathbf{x})E_m^*(\mathbf{x})$$

$$\times\Gamma(\mathbf{x})^3 e^{ik\alpha\cdot\mathbf{x}}\,dx.\tag{41}$$

An approximate nonlinear formula for the scattering potential q can be obtained by taking $W(\mathbf{x})\equiv\Gamma(\mathbf{x})^3$. Equation (41) then yields the coefficients Q_{lm} from Eq. (31) and the resulting solution for the scattering potential is

$$q_M(\mathbf{x})\approx\sum_l\sum_m Q_{lm}\frac{E_l(\mathbf{x})E_m^*(\mathbf{x})}{\Gamma(\mathbf{x})}.\tag{42}$$

The solution of Eq. (42) is simplified by making the further approximation

$$\frac{1}{\Gamma(\mathbf{x})}\approx 2-\Gamma(\mathbf{x}),\tag{43}$$

which is valid for small scattering potentials. This substitution results in

$$q_M(\mathbf{x})\approx\sum_l\sum_m Q_{lm}(2E_l(\mathbf{x})-F_l(\mathbf{x}))E_m^*(\mathbf{x}).\tag{44}$$

This nonlinear equation for the potential q_M can be approximately solved by using a form of the retransmitted field $F_l(\mathbf{x})$ corresponding to the low-pass-filtered potential q_B or to another estimate of the scattering potential.

II. COMPUTATIONAL METHODS

The focusing and imaging methods outlined in Sec. I were implemented using numerically computed scattered fields of inhomogeneous objects. Scattering operators were calculated using a method due to Kirsch and Monk,[23] in which an inner solution of the Helmholtz equation for a medium of variable sound speed is matched to an outer solution of integral equations that implicitly satisfy the Sommerfeld radiation condition. The inner solution is obtained using a finite-element method, while the outer integral equations are solved using Nyström's method.[23]

Scattering data were calculated numerically for a number of incident plane waves evenly distributed over M angles between 0 and 2π. For each incident-wave angle, the scattered field was computed at M far-field receiver angles between 0 and 2π, so that the angular sampling rate was $M/(2\pi)$ samples per radian. The number of receiver angles M should be chosen such that the scattered field has no significant frequency components above the Nyquist frequency of $M/(4\pi)$ samples per radian. This computation yields a discrete representation of the scattering operator A as an $M\times M$ matrix, A_M.

The eigenfunctions of A and their associated eigenvalues were estimated numerically by direct computation of the eigenvectors and eigenvalues of A_M. Retransmitted fields of eigenfunctions were evaluated numerically by numerical integration of Eq. (11). Images of inhomogeneous objects were then obtained using a straightforward numerical implementation of Eqs. (25) and (31). The integrals appearing in these equations were evaluated using corresponding discrete summations of the components of A_M and its eigenvectors. For comparison, standard diffraction tomography inversions were also performed by numerical integration of Eq. (33).

Stability of the eigenfunction imaging method was tested by inversion of noisy data obtained by adding numerically generated Gaussian white noise to the scattering matrix A_M. The rms amplitude of the noise was specified as a fraction of the rms value of A_M. Thus, for instance, a signal-to-noise ratio of 6 dB was obtained by adding noise with an rms amplitude one-half the rms value of A_M.

Inversions were also performed using the basis of eigenfunctions corresponding to axisymmetric inhomogeneities. In this case, the formula of Eq. (25) was implemented numerically using the trigonometric basis functions defined in Eq. (34), the retransmitted fields given in closed form in Eq. (35), and the coefficients defined in Eq. (36).

Nonlinear eigenfunction images were obtained using the analytic formula of Eq. (44) with the total pressure $p(\mathbf{x},\alpha)$ approximated by the total pressure for a medium including a cylinder of specified radius and compressibility contrast. This computation employed an exact solution for the scattering of a plane wave by a cylinder.[17]

III. NUMERICAL RESULTS

Focusing of eigenfunctions on a distributed scattering object is illustrated in Fig. 2. Here, the magnitudes of the retransmitted fields $E_1(\mathbf{x})$ and $E_2(\mathbf{x})$ are shown for an inhomogeneity consisting of a weakly scattering triangle ($\gamma_\kappa=0.01$) approximately two wavelengths in height. The triangle is shown in outline together with the retransmitted fields. The corresponding scattering operator, calculated using the finite-element/Nyström method described above, was represented by a matrix of size 128×128. The retransmitted fields show that the significant eigenfunctions of A specify incident-wave patterns that concentrate energy within the support of the inhomogeneity. Notable is that this focused energy is distributed throughout the support of the triangle.

Implementation of the eigenfunction method in focusing on pointlike scatterers is illustrated in Figs. 3 and 4. These figures, obtained using the linearized eigenfunction method, show not only diffraction-limited focusing but also quantitative reconstructions of the associated scattering potentials. Figure 3 shows images made from the scattered field of two pointlike scatterers at locations $(-0.5,0)$ and $(0,-0.2)$, each of radius 0.01 and compressibility variation -0.9. The numerically computed scattered field was sampled at 128 equally spaced angles for each of 128 incident-wave angles, so that the operator A was represented by a 128×128 matrix. The wave number used was 10, so that the scatterers were separated by approximately one wavelength. Since, in this case, two eigenvalues of A were much larger than the remaining eigenvalues, the basic reconstruction required only the use of two retransmitted fields. This result illustrates that, for an inhomogeneity consisting of finitely many pointlike scatterers, the present inverse scattering method provides an accurate reconstruction with diffraction-limited point resolution using a corresponding number of eigenfunctions.

A stability test of the eigenfunction method is illustrated in Fig. 4. This image shows a reconstruction of the two pointlike scatterers of Fig. 3 using the same scattering data with added Gaussian white noise for a signal-to-noise ratio of 3 dB. The method of reconstruction was identical to that used for Fig. 3. The reconstruction shown is almost indistinguishable from the noiseless reconstruction, indicating the stability of the eigenfunction imaging method.

Linear eigenfunction images of the triangular inhomogeneity of Fig. 2 are presented in Fig. 5. These images were constructed using the same scattering data as that used for Fig. 2. The first image, obtained using five retransmitted fields, shows that strong focusing is achieved using only a few eigenfunctions of A. The entire inhomogeneity is well-insonified and little incident energy is transmitted outside the support of the inhomogeneity. The second image, obtained using 15 eigenfunctions, shows that the eigenfunction method rapidly converges to the ideal low-pass-filtered solution for the scattering potential. Notable is that the eigenfunction method using 15 eigenfunctions required 69.1 s of CPU time on a Sun SPARCstation 10, while an analogous image obtained using the diffraction tomography formula of Eq. (33), with the integrals evaluated in an analogous manner, required 3014.3 s.

Eigenfunction reconstructions of a test phantom, shown in Figs. 6–8, illustrate application of the eigenfunction imaging method to a larger-scale imaging problem. The phantom, also represented in Fig. 1, is a cylinder of compressibility contrast 0.01 and diameter of 5 mm. Internal objects include a water-filled (cystic) region of diameter 1 mm, a wire of diameter 0.1 mm and compressibility contrast -0.5, and an internal cylinder of diameter 1 mm and compressibility contrast -0.01. Scattered fields were calculated using the methods described above, with the operator A discretized as a matrix of 256×256 points. The first image shown in Fig. 6, obtained using the single wave number $k = 10$ has high resolution but contains ringing (Gibbs phenomenon) artifacts and loss of contrast in the cystic region. These artifacts are removed by compounding of images ob-

tained using five linearly spaced wave numbers, $8 \leqslant k \leqslant 12$, so that the dimensionless parameter ka varied between 20 and 30. The five-frequency image, shown in the second panel of Fig. 6, also shows increased point and contrast resolution compared to the single-frequency image. Both images shown in Fig. 6 were obtained using the linearized eigenfunction method described above, with 64 eigenfunctions of A for $k = 8$, 9, and 10, 68 eigenfunctions for $k = 11$, and 72 eigenfunctions for $k = 12$.

Reconstructions of the test phantom obtained from noisy data are shown in Fig. 7. Gaussian white noise was added to the scattering data employed in Fig. 6, so that the signal-to-noise ratio was 6 dB at each of the frequencies employed. The reconstructions employed the formula of Eq. (25) and coefficients obtained from Eqs. (34)–(36). The numbers of basis functions employed were equal to the number of eigenfunctions employed in Fig. 6. These results indicate the stability of the method for large objects with scattering data severely degraded by noise.

Nonlinear reconstructions of the same test phantom, obtained using Eq. (44), are presented in Fig. 8 together with linear reconstructions. In the nonlinear reconstructions, the retransmitted fields $F_l(\mathbf{x})$ were estimated using pressure fields associated with a cylinder of diameter 5 mm and compressibility contrast 0.01.[17] The scattering data employed was identical to that used in Fig. 6(b), with five linearly spaced wave numbers such that $20 \leqslant ka \leqslant 30$. The number of eigenfunctions employed in each image were also the same as those used for the images in Fig. 6. The first panel shows the real part of the nonlinear reconstruction, taken along the line $y = 0$, together with the real part of the analogous linear reconstruction from Fig. 6(b). The nonlinear reconstruction shows improved resolution over the linear reconstruction by increased height of the peak associated with the internal wire. The second panel shows the imaginary part of the nonlinear reconstruction with the corresponding linear reconstruction from Fig. 6(b). Here, the inaccuracy of the Born approximation results in a significant imaginary part for the linear reconstruction, while the true potential is purely real. The nonlinear inversion shows improved quantitative accuracy over the linear inversion by reduction of the reconstructed imaginary part.

IV. DISCUSSION

Our method has shown that eigenfunctions of the scattering operator can be employed to focus on distributed inhomogeneities as well as pointlike scatterers. However, the focusing on distributed inhomogeneities occurs in a different manner from focusing on pointlike scatterers. That is, the incident energy is not maximized at a single point within the medium. Instead, when combined according to the present reconstruction method, retransmitted eigenfunctions specify incident-wave distributions that distribute energy throughout the inhomogeneous region. This type of focusing, which results from the eigenfunction property of maximizing the scattered energy, is clearly connected to imaging of the medium by inverse scattering.

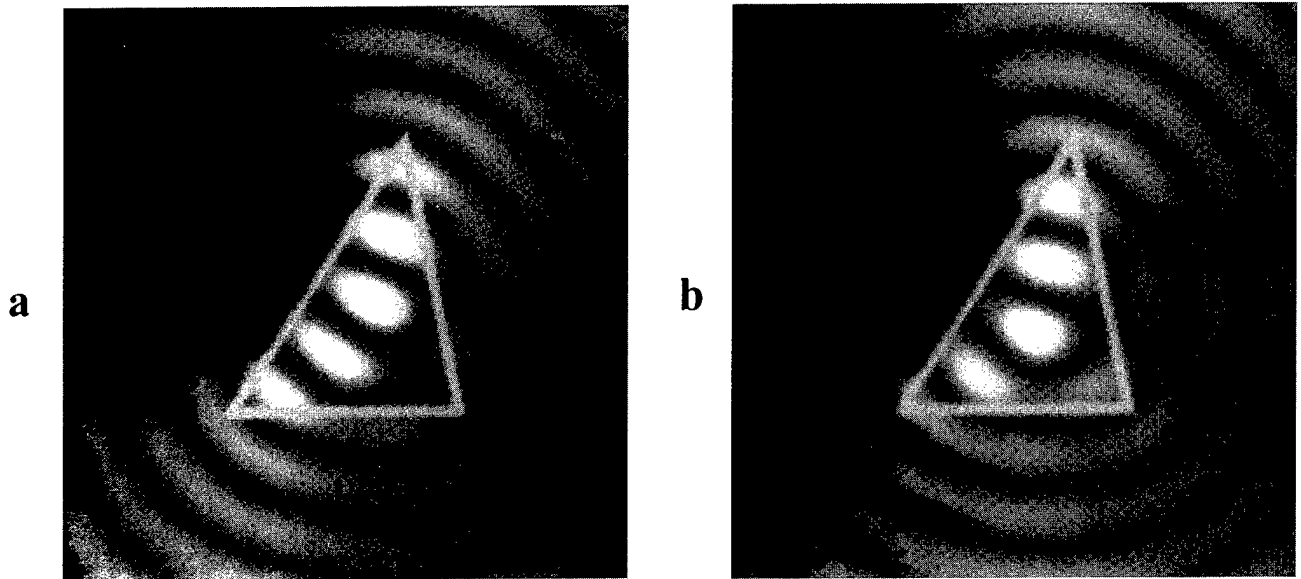The quantitative inverse scattering method presented in this paper can considerably simplify imaging computations.

FIG. 2. Focusing on a distributed inhomogeneity. Magnitudes of the retransmitted fields of the two most significant eigenfunctions are shown on a linear gray scale with black indicating zero and white indicating maximum amplitude. The scattering object is a uniform triangle, compressibility contrast 0.01, within the sketched boundaries. (a) $E_1(\mathbf{x})$, (b) $E_2(\mathbf{x})$.

The computational complexity of the current method depends mainly on the number of significant eigenfunctions, which in turn depends only on the complexity of the scattering medium. Furthermore, the basis for expansion of the unknown medium is determined directly from the scattering data. Since the basis functions are closely related to the unknown medium, reconstructions performed using this basis employ a minimal amount of unnecessary information. This property gives the present inverse scattering method advantages over other methods in which a fixed basis is used to expand the unknown medium.[24-27] These advantages are

most apparent for inhomogeneities a small number of wavelengths in size.

The present inverse scattering method also has the advantage of applicability to any medium for which the background pressure field can be estimated. Use of background pressure estimates can greatly improve accuracy over reconstructions based on simpler approximations. For instance, Born inversion can yield a spurious reconstructed imaginary part even when the true potential is real-valued; use of an estimated background pressure field can greatly reduce this error, as seen in Fig. 8. The inverse scattering method pre-
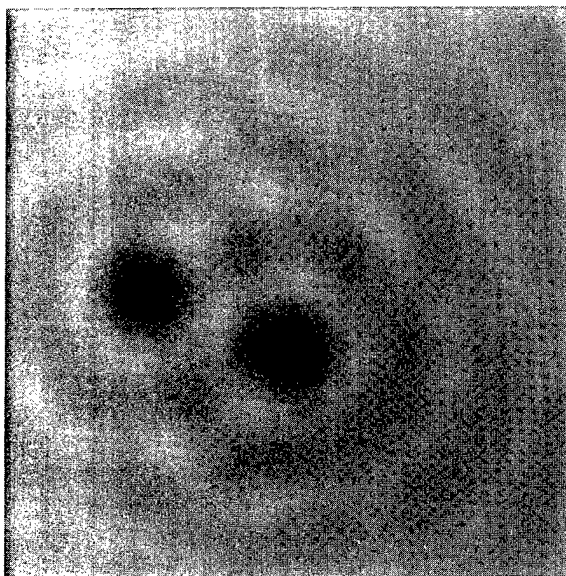
FIG. 3. Eigenfunction image of two pointlike scatterers, compressibility contrast −0.9, separated by approximately one wavelength. The image was obtained using retransmitted fields of the two most significant eigenfunctions.
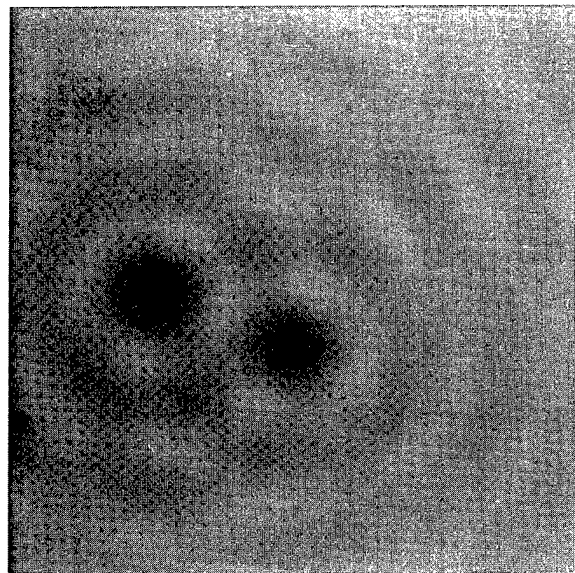

FIG. 4. Effect of noise on eigenfunction reconstruction. The object of Fig. 3 was reconstructed from two eigenfunctions of synthetically noised scattering data with a signal-to-noise ratio of 3 dB.
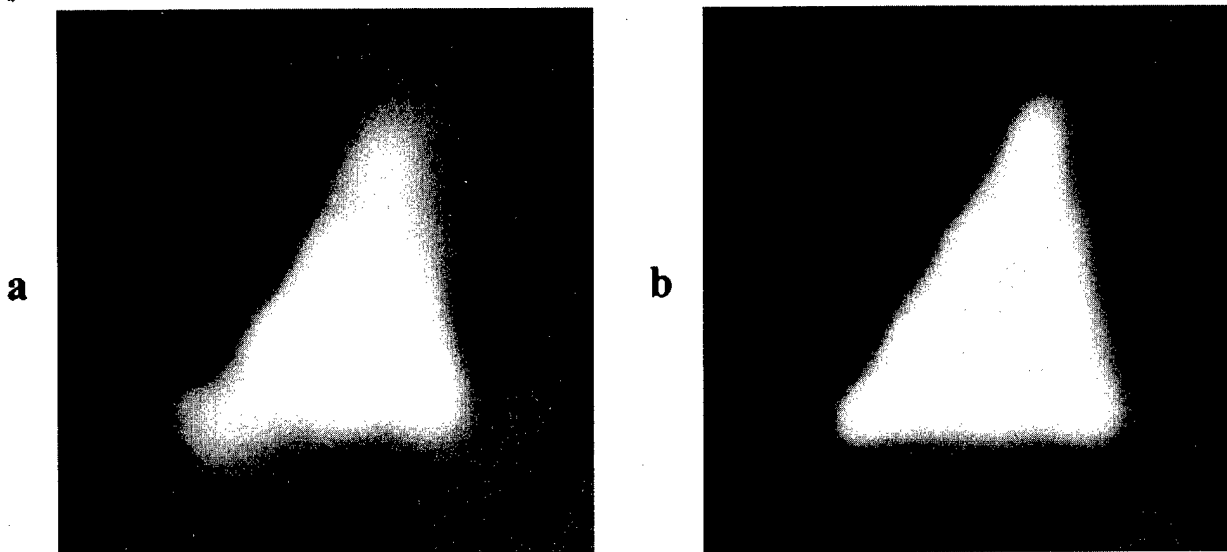
FIG. 5. Eigenfunction images of a triangle about three wavelengths in height having compressibility contrast 0.01. (a) Real part of an inversion obtained using retransmitted fields of five eigenfunctions. (b) Analogous image obtained using 15 eigenfunctions.

sented here is also extensible to any background medium for which a pressure field can be estimated, including moving fluids, layered or stratified media, and enclosed or otherwise bounded regions.

The imaging, focusing, and inverse scattering methods presented here also intrinsically take advantage of any potential increase in resolution that is associated with multiple scattering or other higher-order effects, as long as these effects are taken into account in the estimated pressure field. This increase in resolution is possible because the retransmitted fields of eigenfunctions may have desirable qualities, such as higher spatial-frequency components, that are associated with the presence of an inhomogeneous background. Such improvements in resolution have been shown experimentally for time-reversal focusing in a multiply scattering medium.[28]

The most significant eigenfunctions of A can be determined experimentally through iterative retransmission of received scattered fields in a manner similar to that performed in Refs. 1 and 10. This implementation of the power method[3] allows computation of the most significant eigenfunctions of A by analog means, which may be preferable to numerical computation for very large scattering objects. These eigenfunctions are useful as optimal incident-wave patterns for inverse scattering experiments.

The inverse scattering method presented here includes the assumption that the scattering potential is purely real, that is, the inhomogeneous medium is assumed to have zero absorption. Eigensystem analysis of the scattering operator A is more complicated in the presence of absorption.[29,30] However, the methods introduced here are expected to still
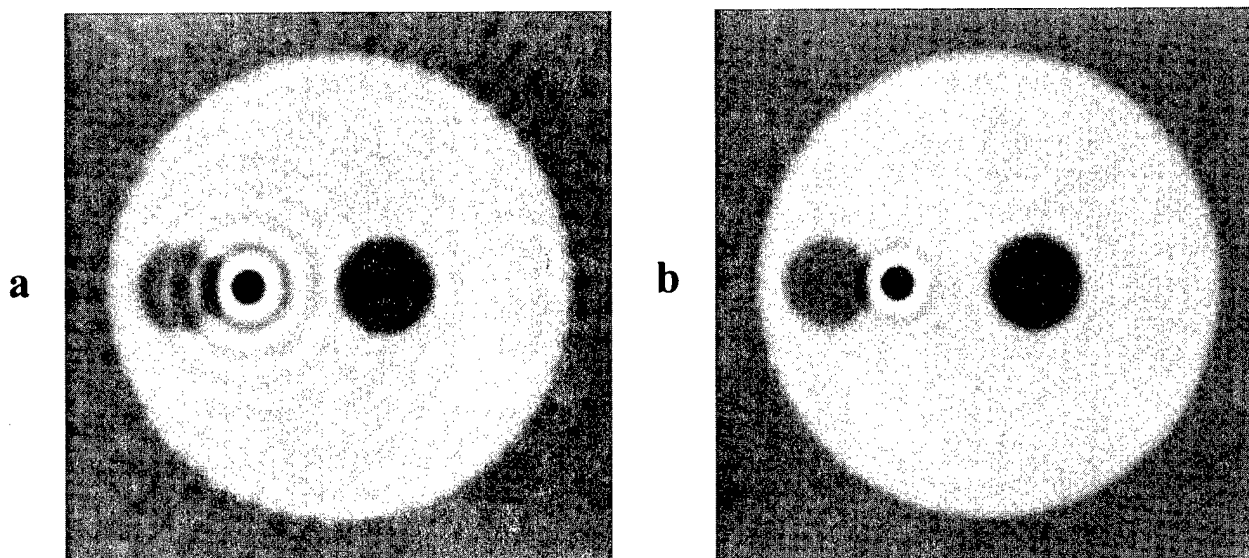

FIG. 6. Eigenfunction images of a test object having background compressibility contrast 0.01, a cystic (water-filled) region, a pointlike scatterer, and an internal cylinder. The images are shown on a logarithmic scale with a 40 dB dynamic range. (a) Real part of inversion obtained for a wave number such that $ka = 25$. (b) Analogous image obtained using five wavenumbers such that $20 < ka < 30$.
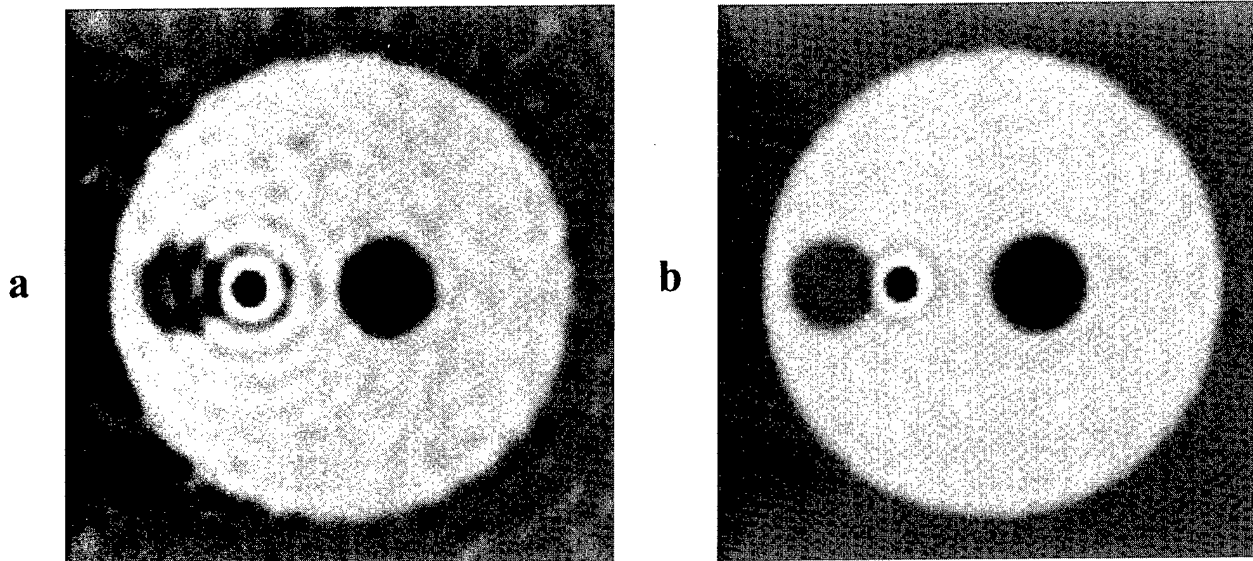
FIG. 7. Images of test object obtained using noised data with 6 dB signal-to-noise ratio. The images are shown on a logarithmic scale with a 40 dB dynamic range. (a) Real part of inversion obtained for a wave number such that $ka=25$. (b) Analogous image obtained using five wave numbers such that $20<ka<30$.

be useful for media such as biological tissue when absorption is finite but small.

A disadvantage of the inverse scattering method as currently implemented is that nonlinear inversion requires an accurate specification of the background acoustic field. This disadvantage is not unique to the eigenfunction method, but is a common feature of most current inversion methods. Recent theoretically exact methods, while not limited in this manner,[31,32] have not yet been implemented numerically.
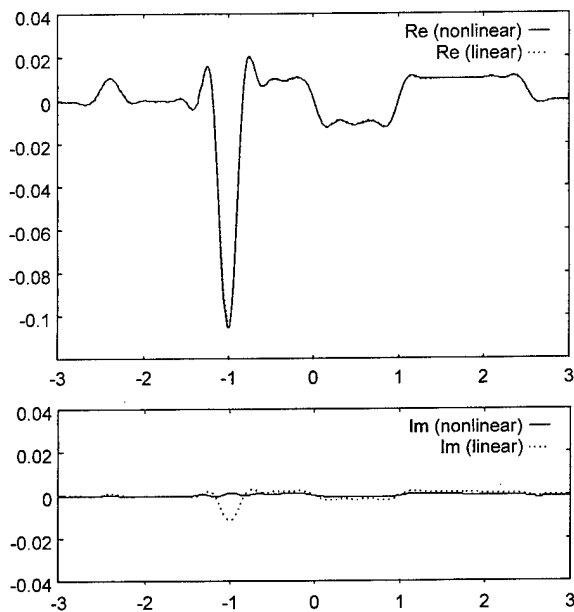

FIG. 8. Cross sections of real and imaginary parts of test object reconstructions using data from five wave numbers. Linear reconstructions were obtained using retransmitted fields in a homogeneous medium, while nonlinear reconstructions were obtained using retransmitted fields in a homogeneous medium and in a background cylinder of compressibility contrast 0.01. (a) Cross sections of real parts. (b) Cross sections of imaginary parts.

The general, nonlinear version of the eigenfunction imaging approach, as defined in Eqs. (24) and (44) and illustrated in Fig. 8, has obvious application to iterative reconstruction of unknown inhomogeneities. In such reconstructions, the total pressure field can be estimated at each iteration from a numerical solution of the direct scattering problem for the currently estimated inhomogeneity, and an eigenfunction inversion can be performed using this pressure field. This procedure can then be repeated to obtain improved estimates of the scattering potential until convergence is achieved.

V. CONCLUSION

A method for focusing and imaging using scattered fields has been presented. The method outlined here makes use of the physical properties of scattering operators by using their eigenfunctions as incident-wave patterns. The eigenfunctions have been shown to provide optimal focusing on pointlike and distributed scattering objects.

The inverse scattering scheme presented exploits the focusing properties of eigenfunctions as well as recent analytic results to obtain a robust and efficient means of quantitatively reconstructing unknown scattering media. This new method has a complexity dependent only on the size and complexity of the scattering medium. Particular cases of the method provide improved implementations of eigenfunction focusing and filtered backpropagation. The method can be implemented for any background medium for which the total acoustic pressure field can be estimated.

Another particular case of the presented method results in a nonlinear inverse scattering formula that yields a solution for the scattering potential q in terms of retransmitted fields of eigenfunctions in the scattering medium and in the background medium. This formula has been demonstrated to yield improvement in accuracy and resolution over Born inversion.

T. D. Mast *et al.*: Eigenfunctions of the scattering operator

The ideas reported here are expected to be useful in further studies of inverse scattering, adaptive focusing, and ultrasonic imaging. The eigenfunctions of the scattering operator A, whether determined by iterative retransmission or by numerical diagonalization, may be used to focus through inhomogeneous media and to determine optimal incident-wave patterns for inverse scattering experiments. Also, the products of fields of eigenfunctions are expected to form a useful basis for expansion of unknown scattering media in iterative reconstruction algorithms.

[1] D. Isaacson, "Distinguishability of conductivities by electric current computed tomography," IEEE Trans. Med. Imaging MI-5, 91–95 (1986).

[2] D. G. Gisser, D. Isaacson, and J. C. Newell, "Electric current computed tomography and eigenvalues," SIAM (Soc. Ind. Appl. Math.) J. Appl. Math. 50, 1623–1634 (1990).

[3] E. Isaacson and H. S. Keller, Analysis of Numerical Methods (Wiley, New York, 1966), pp. 147–159.

[4] G. S. Agarwal, A. T. Friberg, and E. Wolf, "Scattering theory of distortion correction by phase conjugation," J. Opt. Soc. Am. 73, 529–538 (1983).

[5] R. Mittra and T. M. Habashy, "Theory of wave-front distortion by phase conjugation," J. Opt. Soc. Am. A 1, 1103–1109 (1984).

[6] O. Ikeda, "An image reconstruction algorithm using phase conjugation for diffraction-limited imaging in an inhomogeneous medium," J. Acoust. Soc. Am. 85, 1602–1606 (1989).

[7] D. R. Jackson and D. R. Dowling, "Phase conjugation in underwater acoustics," J. Acoust. Soc. Am. 89, 171–181 (1991).

[8] M. Fink, "Time-reversal of ultrasonic fields—Part I: Basic principles," IEEE Trans. Ultrason. Ferroelectr. Freq. Control 39, 555–567 (1992).

[9] D. Cassereau and M. Fink, "Time-reversal of ultrasonic fields—Part III: Theory of the closed time-reversal cavity," IEEE Trans. Ultrason. Ferroelectr. Freq. Control 39, 579–592 (1992).

[10] C. Prada, J. -L. Thomas, and M. Fink, "The iterative time-reversal process: analysis of the convergence," J. Acoust. Soc. Am. 97, 62–71 (1995).

[11] C. Prada, S. Manneville, D. Spoliansky, and M. Fink, "Decomposition of the time reversal operator: Detection and selective focusing on two scatterers," J. Acoust. Soc. Am. 99, 2067–2076 (1996).

[12] K. Chadan and P. C. Sabatier, Inverse Problems in Quantum Scattering Theory (Springer-Verlag, New York, 1989).

[13] A. J. Devaney, "A filtered backpropagation algorithm for diffraction tomography," Ultrason. Imaging 4, 336–350 (1982).

[14] A. J. Devaney and G. Beylkin, "Diffraction tomography using arbitrary transmitter and receiver surfaces," Ultrason. Imaging 6, 181–193 (1984).

[15] A. Witten, J. Tuggle, and R. C. Waag, "A practical approach to ultrasonic imaging using diffraction tomography," J. Acoust. Soc. Am. 83, 1645–1652 (1988).

[16] J. R. Taylor, Scattering Theory (Wiley, New York, 1972).

[17] P. M. Morse and K. U. Ingard, Theoretical Acoustics (McGraw-Hill, New York, 1968), Chap. 8.

[18] P. M. Morse and H. Feshbach, Methods of Theoretical Physics (McGraw-Hill, New York, 1953), Vol. I.

[19] M. Reed and B. Simon, Methods of Mathematical Physics (Academic, San Diego, 1980), Vol. III.

[20] G. N. Watson, A Treatise on the Theory of Bessel Functions (Macmillan, New York, 1944), 2nd ed., p. 359.

[21] D. C. Dobson and F. Santosa, "Resolution and stability analysis of an inverse problem in electrical impedance tomography: dependence on the input current patterns," SIAM (Soc. Ind. Appl. Math.) J. Appl. Math. 54, 1542–1560 (1994).

[22] T. M. Habashy, R. W. Groom, and B. R. Spies, "Beyond the Born and Rytov approximations: a nonlinear approach to electromagnetic scattering," J. Geophys. Res. 98, 1759–1775 (1993).

[23] A. Kirsch and P. Monk, "An analysis of the coupling of finite element and Nyström methods in acoustic scattering," IMA J. Num. Anal. 14, 523–544 (1994).

[24] T. J. Cavicchi and W. D. O'Brien, "Numerical study of higher-order diffraction tomography via the sinc basis moment method," Ultrason. Imaging 11, 42–74 (1989).

[25] D. T. Borup, S. A. Johnson, W. W. Kim, and M. J. Berggren, "Nonperturbative diffraction tomography via Gauss-Newton iteration applied to the scattering integral equation," Ultrason. Imaging 14, 69–85 (1992).

[26] W. C. Chew and G. P. Otto, "Microwave imaging of multiple conducting cylinders using local shape functions," IEEE Microwave Guided Wave Lett. 2, 284–286 (1992).

[27] H. Gan, R. Ludwig, and P. L. Levin, "Nonlinear diffractive inverse scattering for multiple scattering in inhomogeneous acoustic background media," J. Acoust. Soc. Am. 97, 764–776 (1995).

[28] A. Derode, P. Roux, and M. Fink, "Acoustic time-reversal through high-order multiple scattering," 1995 IEEE Ultrasonics Symposium Proceedings (IEEE, Piscataway, NJ, 1995), Vol. 2, pp. 1091–1094.

[29] D. Colton and R. Kress, "Eigenvalues of the far field operator and inverse scattering theory," SIAM J. Math. Anal. 26, 601–615 (1995). One of the anonymous reviewers is thanked for drawing the authors' attention to Refs. 29 and 30.

[30] D. Colton and R. Kress, "Eigenvalues of the far field operator for the Helmholtz equation in an absorbing medium," SIAM (Soc. Ind. Appl. Math.) J. Appl. Math. 55, 1724–1735 (1995).

[31] A. I. Nachman, "Reconstructions from boundary measurements," Ann. Math. 128, 531–576 (1988).

[32] A. I. Nachman, "Global uniqueness for a two-dimensional inverse boundary problem," Ann. Math. 143, 71–96 (1996).